



# Politecnico di Bari

Repository Istituzionale dei Prodotti della Ricerca del Politecnico di Bari

Modelling, simulation and experimental validation of the behaviour of a piezoelectric cantilever beam in Energy Harvesting and non-destructive diagnostic fields

This is a PhD Thesis

*Original Citation:*

Modelling, simulation and experimental validation of the behaviour of a piezoelectric cantilever beam in Energy Harvesting and non-destructive diagnostic fields / DI MODUGNO, Filomena. - (2017). [10.60576/poliba/iris/di-modugno-filomena\_phd2017]

*Availability:*

This version is available at <http://hdl.handle.net/11589/102568> since: 2017-04-14

*Published version*

Politecnico di Bari  
DOI: 10.60576/poliba/iris/di-modugno-filomena\_phd2017

*Terms of use:*

Altro tipo di accesso

(Article begins on next page)



Politecnico  
di Bari

Department of Electrical and Information Engineering  
ELECTRICAL AND INFORMATION ENGINEERING

Ph.D. Program

SSD: ING-IND/31– ELECTRICAL ENGINEERING

**Final Dissertation**

---

Modelling, simulation and experimental  
validation of the behaviour of a  
piezoelectric cantilever beam  
in Energy Harvesting and  
non-destructive diagnostic fields

---

by

Filomena Di Modugno

Supervisor:

Prof. Giuseppe Acciani

*Coordinator of Ph.D Program:*

*Prof. Vittorio Passaro*

---

*XXIX cycle, 2014-2016*



Politecnico  
di Bari

Department of Electrical and Information Engineering  
ELECTRICAL AND INFORMATION ENGINEERING

Ph.D. Program

SSD: ING-IND/31– ELECTRICAL ENGINEERING

**Final Dissertation**

---

Modelling, simulation and experimental  
validation of the behaviour of a  
piezoelectric cantilever beam  
in Energy Harvesting and  
non-destructive diagnostic fields

---

by  
Filomena Di Modugno

---

Referees:

Prof. Sergejus Borodinas

Prof. Paula Lopez

Supervisor:

Prof. Giuseppe Acciani

---

*Coordinator of Ph.D Program:*  
*Prof. Vittorio Passaro*

---

*XXIX cycle, 2014-2016*

*"It is important to make a dream of life and of a dream reality"*

*Pierre Curie  
Nobel Prize for Physics in 1903*

*To Girolamo, the Man who made of my dreams reality.*

# Summary

<i>Acknowledgments</i> .....	5
<i>Introduction</i> .....	6
<b>1. Chapter 1</b> .....	13
<b>1.1. Introduction</b> .....	14
<b>1.2. Classification of piezoelectric materials</b> .....	15
<b>1.3. New piezoelectric materials</b> .....	18
<b>1.4. Piezoelectric effects. Sensors and actuators.</b> .....	20
<b>1.5. Piezoelectric Constitutive Equations.</b> .....	22
<b>1.6. Piezoelectric Coefficients.</b> .....	24
<b>1.7. Piezoelectric crystals and crystallography.</b> .....	25
<b>1.8. Electromechanical conversion of energy.</b> .....	28
<b>1.9. Conclusions.</b> .....	32
<b>References.</b> .....	32
<b>2. Chapter 2</b> .....	34
<b>2.1 Introduction</b> .....	35
<b>2.2 A mathematical model</b> .....	36
2.2.1. <i>Statistical Linearization approach</i> .....	38
2.2.2. <i>Predictor - corrector algorithm for Lyapunov equation integration</i> .....	44
2.2.3. <i>Application: Bouc-Wen systems subjected to non-stationary base random input</i> .....	45
2.2.4. <i>The Bouc-Wen model equivalent linearization</i> .....	47
2.2.5. <i>Modelling of Input Ground Motion</i> .....	48
2.2.6. <i>Stochastic Analysis</i> .....	49
2.2.7. <i>Numerical analysis</i> .....	50
2.2.8. <i>Future Research</i> .....	53
<b>2.3 Boundary conditions for vibrational and piezoelectric problems</b> .....	54
<b>2.4 Conclusions</b> .....	55
<b>References</b> .....	55

3. Chapter 3.....	58
3.1. Introduction .....	59
3.2. Case study 1: an ideal cantilever beam under pressure .....	60
3.2.1. Piezoelectric Materials.....	61
3.2.2. Boundary Conditions.....	63
3.2.3. The mesh .....	64
3.2.4. Simulation results .....	65
3.2.4.1. Lead Zirconate Titanate.....	65
3.2.4.2. Cadmium Sulfide.....	67
3.2.4.3. Bismuth Germanate .....	68
3.2.4.4. Polyvinylidene Fluoride .....	69
3.2.5. Simulations with different thickness.....	71
3.2.5.1. Increasing Thickness.....	71
3.2.5.2. Decreasing Thickness .....	72
3.3. Case study 2: a real cantilever beam under pressure .....	76
3.3.1. <i>Experimental apparatus</i> .....	76
3.3.2. <i>Mathematical model</i> .....	79
3.3.3. <i>Simulations</i> .....	80
3.3.4. <i>Numerical results</i> .....	81
3.3.5. <i>Simulations with different materials</i> .....	82
3.3.6. <i>Simulation with different shapes</i> .....	84
3.4. In-depth analysis of FEM mesh .....	87
3.4.1. <i>A multiplier factor.</i> .....	88
3.4.2. <i>A different mesh</i> .....	91
3.4.3. <i>Mesh Streamlining.</i> .....	92
3.5. Case study 3: interaction of a cantilever beam with a fluid.....	93
3.5.1. <i>Mathematical Modelling and Simulation Environment</i> .....	94
3.5.2. <i>Fluid Model</i> .....	96
3.5.3. <i>Fluid-structure interaction Model</i> .....	97
3.5.4. <i>Electromechanical coupling Model</i> .....	97

3.5.5.	<i>Simulations</i> .....	98
3.5.6.	<i>Boundary Conditions</i> .....	98
3.5.7.	<i>Material properties</i> .....	98
3.5.8.	<i>Mesh</i> .....	99
3.5.9.	<i>Results</i> .....	99
<b>3.6.</b>	<b>Case study 4: interaction of a fluid with a cantilever beam locked to a bluff body.</b>	
	102	
3.6.1.	<i>Parametric Shape Optimization of the Bluff element</i> .....	103
3.6.2.	<i>Multiphysics Numerical Setup</i> .....	104
3.6.3.	<i>Bluff body profile geometric parametrisation</i> .....	105
3.6.4.	<i>Numerical optimization of the parametric Bluff</i> .....	106
3.6.5.	<i>Simulation results</i> .....	108
<b>3.7.</b>	<b>Conclusions.</b> .....	111
	<b>References.</b> .....	112
<b>4.</b>	<b>Chapter 4</b> .....	115
4.1.	<b>Introduction</b> .....	116
4.2.	<b>Applications in NDE</b> .....	118
4.2.1.	<i>The axle box</i> .....	118
4.2.2.	<i>The sensor node</i> .....	120
4.2.3.	<i>The energy harvester</i> .....	120
4.2.4.	<i>Mathematical model</i> .....	122
4.2.5.	<i>Stationary analysis</i> .....	122
4.2.6.	<i>Eigenfrequency analysis</i> .....	123
4.2.7.	<i>Time dependent analysis</i> .....	126
4.2.8.	<i>Study in the presence of defects</i> .....	130
4.2.9.	<i>Study in the presence of a different defect</i> .....	135
4.3.	<b>Ongoing and future research</b> .....	139
4.4.	<b>Conclusions.</b> .....	141
	<b>References.</b> .....	142
<b>5.</b>	<b>Conclusions</b> .....	144

6. *List of publications co-authored by the PhD candidate*.....149

## *Acknowledgments*

I would like to express my deep gratitude to my doctoral advisor Professor Dr. Eng. Giuseppe Acciani. Three years ago he accepted the challenge of 'transforming' a Mathematics graduate into a PHD in Electrical Engineering. Today we are winning that challenge together. In these three years, I have discovered a person with a great humanity, always ready to encourage my studies and research. I wish to thank him for his help, support and teaching.

I would like to thank my doctoral co-advisor Professor Dr. Eng. Ernesto Mininno for his patience in reading and correcting my thesis.

I need to show my gratitude to my external referee Professors Dr. Eng. Paula Lopez Martinez and Sergejus Borodinas and my committee members for their role.

My appreciations also extend to Professor Dr. Eng. Cataldo Guaragnella who first saw the 'seeds' of a PHD in my person and to Professor Richard Lusardi for his advice on my PHD thesis as mother tongue expert in scientific and technical English.

A special thanks to Pasquale Montegiglio and Giancarlo Gelao, my 'travel friends' in the PHD course, for all the simulations, graphics, discussions and moments that we have spent together, to Antonio Giaquinto and Roberto Dinapoli, my 'brothers' in the PHD course, in my thesis and in my life, to my sister Raffaella who never left me alone, especially during my working trips abroad.

Especially I am fully indebted with my sons Alessandro and Enrico and my daughter Arianna since all the time dedicated to the PHD course and to its final thesis has been taken from them. I want to thank them for their patience and maturity, despite their young age, in understanding the importance of my absences.

Another special thanks to my parents and parents-in-law because they have always been present in the life of my family, helping my children when I was not with them and supporting me in my critical moments.

My last but not least acknowledgement is for my beloved husband Girolamo. I decided to attend the PHD course also to fulfil his dreams but he has never left me alone on this path, even if now he is looking down at me from another Dimension.

## Introduction

Environmental pollution is one of the biggest world problems nowadays and is closely connected to other important problems such as rapid climate change and the wide diffusion of fatal illnesses. Even though the damaging effects of fossil fuels on the environment are well known, coal, oil and natural gas are still exploited on a large scale to satisfy world energy demand.

Research into energy source consumption in 2015, carried out as part of the BP Statistical Review of World Energy, provided the results depicted in Figure 1 [1] in which oil consumption is measured in million tonnes and other fuels are measured in million tonnes of oil equivalent. Figure 1 shows that the use of fossil fuels still had a growing trend and oil was still the dominant fuel in the world, with an annual consumption of 4331.3 million tonnes, while coal had an annual consumption of 3839.9 million tonnes. On the other hand, renewable energies represented the least exploited source with an annual consumption of 364.9 million tonnes, compared with a total annual consumption of energy of 13147.3 million tonnes. This analysis highlights how the percentage of employment of polluting sources of energy is still high compared with that referred to clean ones.

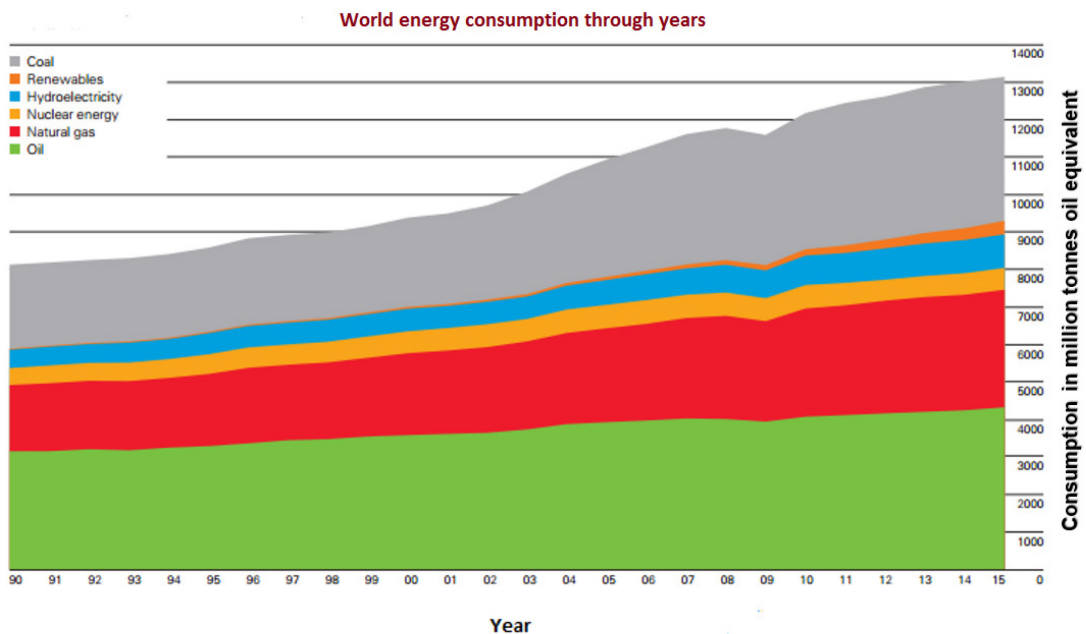


**Figure 1 – World energy consumption from 1990 until 2015 for different energy sources (Courtesy to BP Statistical Review of World Energy 2016 BP).**

Another important contribution to environmental degradation is due to a phenomenon that has seen a wide diffusion in the last decade. Low-power electronic devices, such as wearable devices and wireless autonomous elements for sensor networks, have seen an increasing production and a fast adoption rate for practical uses. The miniaturization of this class of devices in the sub-micrometre size range has not been paralleled by an analogous shrink in the chemical battery sources [2]. The recharging or replacement of chemical batteries in such devices is often expensive or very difficult and sometimes impossible because of their location in the device. The reduced life of batteries influences and reduces the life of electronic devices when they could still work, as their natural lives are longer than those of their batteries [3-4]. This implies a double environmental damage due to the premature disposal of electronic devices and an increasing amount of exhausted batteries.

The concern for reducing the production of energy from traditional and non-renewable forms, the requirement of producing non-polluting and not expensive energy on site, the ecological concept of abating the chemical waste produced by replacing batteries and the need to reduce maintenance costs for smaller devices have all sparked increasing interest in researchers seeking cheap and non-polluting alternative sources of energy. In recent years, several studies into alternative energies have been developed, also encouraged by authorities such as the European Parliament or the Council of the European Union [5]. At the end of 2015, the world electricity powered by renewable sources of energy reached 23.9% of the total world electricity production [6]. Figure 2 shows the partition of this percentage for each single source of renewable energy [6].

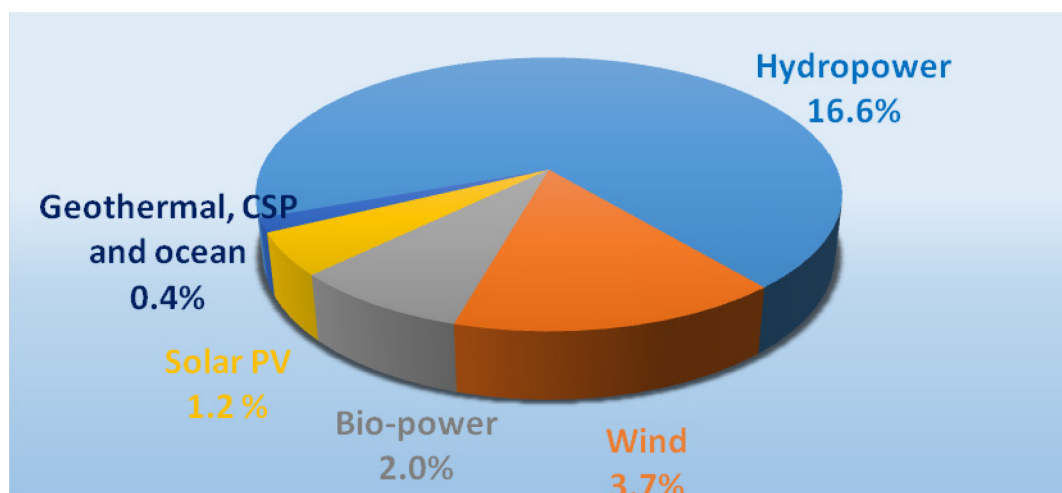


*Figure 2– Estimated Renewable Energy as a Share of total Global Electricity Production, End–2015.*

The aim of renewable energies fits well with the philosophy of a science that studies the conversion of energy wasted in the environment into different and more useful forms, in particular the electric one: this science is called *Energy Harvesting* (EH). Energy is everywhere around us, it is possible to harvest energy in different ways, capturing it from environmental sources such as solar, thermal, wind-kinetic energy and natural vibrations. These alternative sources of energy, free and inexhaustible in the environment, are converted into electrical energy through non-polluting processes. Some of them, such as wind and vibrational energy, are used directly by devices that work as generators under the effect of vibrations, due to a specific form of excitation: according to Erturk and Inman [2], these devices are defined as *energy harvesters*. They are raising increasing interest because they can power small and low-power electrical apparatus [7-8]. The use of a piezoelectric harvester, instead of traditional batteries, allows the achievement of an energetically autonomous system, which does not need periodic maintenance to replace batteries and does not produce chemical waste.

The conversion process of environmental energy into electrical power often involves smart materials such as piezoelectric materials, which develop electrical charge when subject to mechanical stress (direct piezoelectric effect): this charge can be stored by means of an electrical circuit. Moreover, piezoelectric materials for EH are cheap and easy to manage. Furthermore, the piezoelectric effect is one of the most studied areas by EH researchers.

One of the main purposes in designing a wind energy harvester made of a piezoelectric material is to improve its electrical performance and so reduce costs. Different types of piezoelectric transducers can be used to harvest energy, including monomorphs, bimorphs, stacks or membranes. According to Erturk and Inman [2], each configuration has advantages and disadvantages so each device needs to be opportunely designed for its intended application. Indeed, the electromechanical response of a piezoelectric energy harvester and the amount of power it generates are completely dependent on the nature of the ambient energy. Most piezoelectric energy harvesters are in the form of cantilever beams with one or two piezoceramic layers, because of the simplicity of this kind of structure. The harvester beam is located on a vibrating host structure and the dynamic strain induced in the piezoelectric layers is converted into an alternating voltage output across its electrodes [2]. A wide range of devices made of piezoelectric

materials has been developed in the EH field, for various large and small-scale applications. Great interest has been directed to piezoelectric transducers stressed by natural vibrations, such as those induced by rain [9] or wind.

Figure 2 shows that wind energy is currently the second most important renewable source of electric energy. It is available everywhere in the world and wind harvester devices can be used and applied universally. For this reason, wind energy has been exploited for many years. Good examples of wind harvester devices are traditional windmills or wind turbines located on land (onshore) or in the sea or freshwater (offshore), even if they have a non-negligible environmental impact. In order to prevent ecological damage, EH researchers are considering different solutions for exploiting wind energy. In 2013, a group of researchers at Cornell University [10] arranged a structure, the so-called *Vibro-Wind* technology, consisting of wind transducers and used it to convert wind-induced vibrations into electrical energy. More recently this kind of technology has been improved by Valtchev, Almeida, Teixeira and Klaassens through an in-depth study of the appropriate dimensions of the piezoelectric transducers [11]. Other differently assembled devices have been developed to convert wind into electrical power [12-13] and most of them are equipped with centimetre-sized transducers while the whole structure is about one square metre.

In the field of small-scale windmills, Yang et al. have presented a rotational piezoelectric energy harvester in which impact-induced resonance is used to enable effective excitation of the intrinsic mode of vibration of piezoelectric cantilevers: this implies an optimum deformation of the cantilevers themselves, which is beneficial for the transformation of kinetic into electric energy. The small windmill was realised with piezoelectric bimorph cantilevers locked at one end and arranged as a polygon, which has some elastic balls inside. When the wind causes the rotation of the device, the balls strike the piezoelectric layers, producing electric potential because of the piezoelectric effect [14].

Rezaei et al. proposed a topology for piezoelectric EH consisting of a lift-based wind turbine and a piezoelectric beam with a contactless vibration mechanism. This structure enables energy to be harvested at a wide range of wind speeds [15].

Starting from the above recalled context, this dissertation is aimed at contributing to the production of clean and inexpensive energy, using small piezoelectric devices

stressed by natural vibrations and useful to provide energy to low-power devices.

The objective is to understand how a piezoelectric cantilever beam reacts under the effect of vibrations that could be induced by a flowing fluid, such as air or water, or by mechanical movement, such as that of a train on the rails. The vibrational analysis was carried out both using experimental apparatus and in a simulation environment, in order to validate the simulations with experimental data. This validation lends reliability to the simulation process that can be extended to analyse situations not easily testable in the laboratory. Furthermore, the simulation environment offers the opportunity of looking for the optimization of several constitutive elements of cantilever beams, such as their shapes, thicknesses and materials they are made of, so allowing the design of an ‘optimal’ cantilever beam, specific for the situation considered. The electrical potential developed by such devices can be stored and reused following the principles of EH. Moreover, these so designed devices can be used as sensors in the field of Non-destructive testing. For example, studies about dynamics of trains have shown that, due to the irregularities of the railway line, the accelerations on some mechanical parts of the train, such as the axle box, are greater than elsewhere, so the axle box is one of the safety-critical subsystems in railway vehicles [16] and one of the most stressed components of the train wheelset. For this reason, it could be chosen as the optimal place to install a piezoelectric harvester that receives vibrations from the axle box and converts the acceleration into electric potential, useful to power a wireless sensor node. The self-powered sensor node can provide information about the state of health of the axle box itself in real time. Therefore, the described system achieves energy harvesting and diagnostic goals simultaneously.

All the simulations presented in the dissertation were realised using Comsol Multiphysics, software that uses the Finite Element Method (FEM) to solve mathematical models. The FEM is one of the most popular numerical methods used to calculate approximated solutions for problems described mathematically by Partial Differential Equations (PDEs). It is often used to ‘simplify’ real-world problems that involve complicated physics, geometry and boundary conditions [17]. The continuous given domain in FEM simulations is split up into many smaller and simpler subdomains, the boundaries of which ensure continuity for input and output variables. This division is obtained using imaginary lines and surfaces. Each subdomain, a ‘Finite

Element', performs as a 'simpler' way to find a solution to the problem, compared to that useful for the original domain. The collection of the subdomains created is called the *mesh*, the construction of which represents a crucial point in order to find a good convergent solution to the mathematical equations that describe the problem.

In more detail, Chapter 1 of this work focuses on the analysis of piezoelectric materials and their properties: classification of materials, studies about new piezoelectric materials, constitutive equations and matrices to describe their behaviour in converting mechanical energy into electrical energy and vice versa.

A mathematical model is proposed in Chapter 2 to study mechanical vibrations and focuses on all the boundary conditions useful to define a vibrational problem correctly.

Chapter 3 presents the modelling, simulation, optimization and experimental validation of the behaviour of a piezoelectric cantilever beam. The analysis is carried out with some different case studies, describing the cantilever beam in situations with an increasing degree of difficulty. Initially the device is analysed under the effect of a force with the same intensity as wind action, then its interaction with a fluid is studied and finally a situation with a device anchored to a bluff body is presented.

Finally, Chapter 4 illustrates the possible applications of piezoelectric harvester devices, in EH and Non-destructive testing fields.

Each chapter is introduced with a deep analysis on the corresponding issue and its peculiarities as well as a literature review aimed at identifying the state of the art on the topic and positioning its contribution.

## References.

- [1] BP Statistical Review of World Energy June 2016, <http://www.bp.com/content/dam/bp/pdf/energy-economics/statistical-review-2016/bp-statistical-review-of-world-energy-2016-full-report.pdf>.
- [2] Ertuk A., Inman D.J. "Piezoelectric Energy Harvesting". John Wiley and Sons, Ltd., Publication, Chichester, UK, 2011, pp.146.
- [3] Anton S.R., Sodano H.A. "A review of power harvesting using piezoelectric materials (2003-2006)". Smart Materials and Structures, 2007, Vol. 16, No. 3, pp. R1-R21.
- [4] Heung Soo K., Joo-Hyon, Jaehwan K. "A review of piezoelectric energy harvesting based on vibration". International Journal of Precision Engineering and Manufacturing, 2011, Vol. 12, No. 6, pp. 1129-1141.
- [5] EC. "Directive of The European Parliament and of The Council on the promotion of the use of energy from renewable". 23 April 2009.
- [6] [http://www.ren21.net/wp-content/uploads/2016/06/GSR\\_2016\\_Full\\_Report.pdf](http://www.ren21.net/wp-content/uploads/2016/06/GSR_2016_Full_Report.pdf)
- [7] Sodano H.A, Inman D.J., Park G. "Comparison of piezoelectric energy harvesting devices for recharging batteries". Journal of Intelligent Material Systems, 2005, Vol.16, pp.799-807.

- [8] Shu Y.C., Lien I.C. "Analysis of power output for piezoelectric energy harvesting systems". *Smart Materials and Structures*, 2006, Vol.15, pp.1499–1511.
- [9] Viola F., Romano P., Miceli R., Acciari G., "On the harvesting of rainfall Energy by means of piezoelectric transducer", *Proc International Conference on Renewable Energy Research and Applications, ICRERA 2013*, pp. 1133-1138.
- [10] Kluger J.M, Moon F.C., Rand R.H. "Shape optimization of blunt body Vibro-wind galloping oscillator". *Journal of Fluids and Structures*, 2013, Vol. 40, pp. 185-200.
- [11] Valtchev S., Almeida J., Teixeira J.P., Klaassen J.B. "Conversion of Wind-Induced Vibrations into Electricity". *Proc. of IEEE 36th International Telecommunications Energy Conference - INTELEC 2014*, pp 1-8.
- [12] He X.F., Gao J., "Wind energy harvesting based on flow-induced-vibration and impact". *Microelectronic Engineering*, 2013, Vol.111, pp. 82-86.
- [13] Mutsuda H., Miyagi J., Doi Y., Tanaka Y., Takao H., Sone Y. "Flexible piezoelectric sheet for wind energy harvesting". *International Journal of Energy Engineering*, 2014, Vol.4, No. 2, pp. 67-75.
- [14] Yang Y., Shen Q.L., Jin J.M., Wang Y.P., Qian W.J., Yuan D.W. "Rotational piezoelectric wind energy harvesting using impact-induced resonance". *Applied Physics Letters*, 2014, Vol. 105, No. 5.
- [15] Rezaei N., Tabesh A., Dehghani R., Aghili A. "An Efficient Piezoelectric Windmill Topology for Energy Harvesting from Low Speed Air Flows". *IEEE Transactions on Industrial Electronics*, 2015, Vol. 62, No. 6, pp. 3576-3583.
- [16] <http://evolution.skf.com/the-evolution-of-ilwayaxlebox-technology/>.
- [17] Reddy J.N. "An Introduction to the Finite Element Method (Third ed.)". McGraw-Hill, 2006.

## ***1. Chapter 1***

### ***Piezoelectric materials and electromechanical conversion of energy***

In this chapter an overview about piezoelectric materials and their properties is proposed.

The chapter begins with a brief historical introduction and goes on to a classification of piezoelectric materials with their advantages and disadvantages. New piezoelectric materials are described and the reasons for researching this field are explained. The constitutive equations of these materials with their matrices, coefficients and their physical meanings are described. Elements of crystal classes and their relationship with piezoelectric materials are discussed. The chapter closes with an analysis of electromechanical conversion of energy applied to a capacitive two-port device.

## 1.1. Introduction

The word *piezoelectricity* is composed of two Greek words ‘piezein’, which means ‘to press’, and ‘ēlektron’, which means ‘amber’, an ancient source of electric charge [1]. Therefore, the word ‘piezoelectricity’ means ‘electricity generated from a pressure’ [2].

The piezoelectric phenomenon was discovered by Jacques and Pierre Curie. They observed that some natural crystals such as quartz, tourmaline, Rochelle salt and cane sugar were able to generate electric charges on their surfaces when they were mechanically stressed. In 1880 the first scientific work on piezoelectricity was published [3]. One year later the Curie brothers gave experimental confirmation of the converse piezoelectric effect which had been mathematically predicted by Lippmann from the laws of thermodynamics [2,4].

Even though the properties of piezoelectric materials were discovered at the end of the nineteenth century, the first applications of these materials were made during World War I and became more widely used between the two World Wars, with their employment in objects such as microphones [2]. Quartz was still the most exploited piezoelectric material with a growing demand. In order to satisfy that demand, in 1935 researchers postulated the possibility of growing a synthetic crystal with the same properties as natural quartz. In 1958 synthetic quartz was produced and commercialized, with the quality of this crystal being better than the natural one [5]. Nowadays, these materials find wide applications in everyday objects, such as sensors, watches, the computer mouse, lighters and medical devices (Metered-Dose Inhaler "Puffers", scalpels). Figure 1.1 shows an overview of the piezoelectric device market trends in 2015<sup>1</sup>.

---

<sup>1</sup> The percentages depicted in Figure 1.1 were shown by Prof. Kenji Uchino during his presentation ‘Medical Applications of Piezoelectric Devices – Introduction to Practical Successful Piezoelectric Products In The Medical Area’ at the 12th International Workshop on Piezoelectric Materials and Applications in Actuators (IWPMVA Vilnius 2015). Data sources: iRAP and IdTechEx.

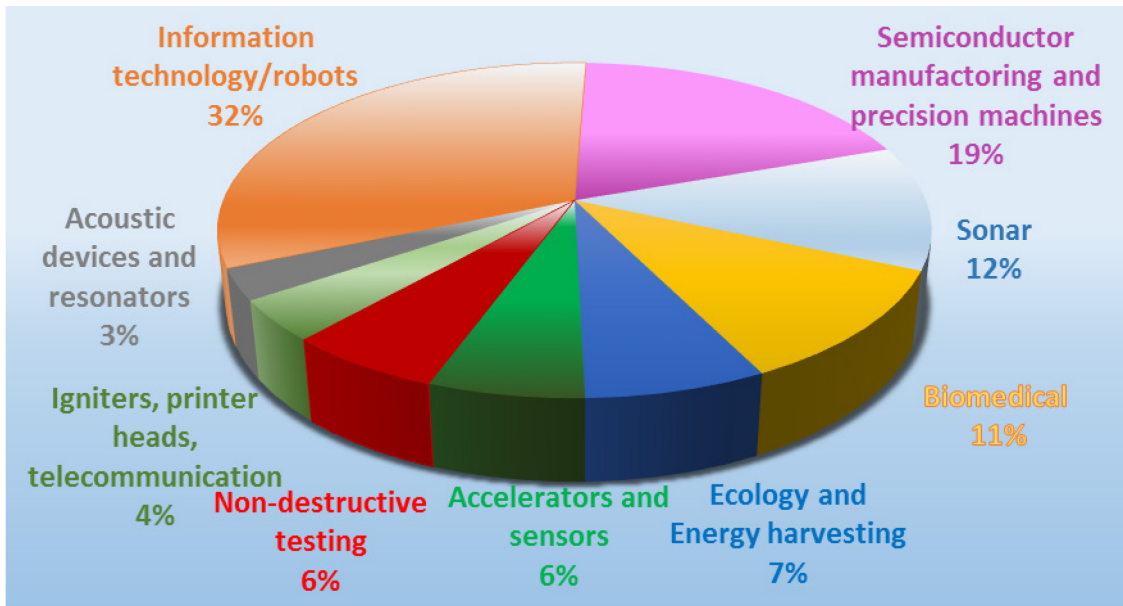


Figure 1.1 – Piezoelectric devices market trend in 2015.

## 1.2. Classification of piezoelectric materials

Piezoelectric materials are dielectric crystals with a symmetric atomic structure and with a total dipole moment not equal to zero. Their relationship to dielectric, pyroelectric<sup>2</sup> and ferroelectric<sup>3</sup> materials is shown in the diagram in Figure 1.2.

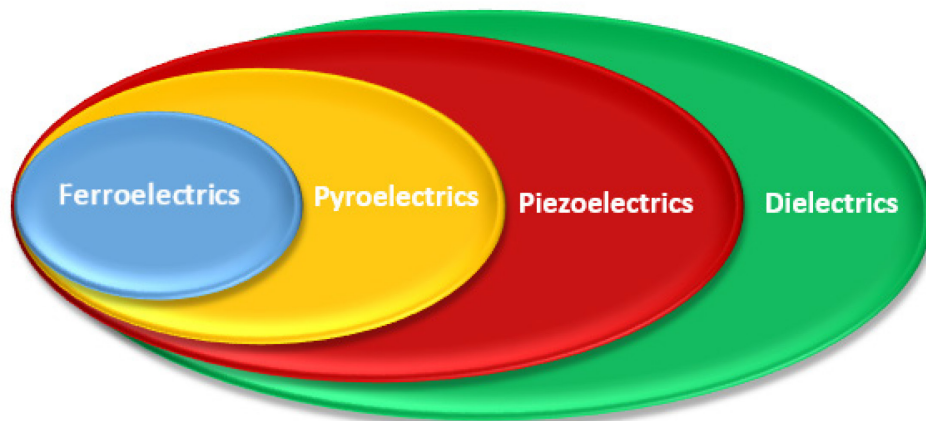


Figure 1.2 – Subcategories of dielectric materials.

<sup>2</sup> Materials able to generate electrification or electrical polarity produced in certain crystals by temperature changes [1].

<sup>3</sup>Materials which possess spontaneous electric polarization such that the polarization can be reversed by an electric field [1].

Piezoelectric materials can be natural, such as those analysed by the Curie brothers, or synthetic. They are classified into four main groups: natural crystals, *piezo ceramics*, *piezo polymers* and *piezo composites* [7].

Examples of materials belonging to the natural crystals are quartz, berlinite (structurally identical to quartz), tourmaline, Rochelle salt, cane sugar, topaz. Cane sugar is not commonly exploited for its piezoelectric properties because it breaks easily and has a lower melting point (185°C). Tourmaline cannot be synthesized because it is brittle and therefore difficult to process. Quartz is exploited much less than in the past because its natural crystals contain too many imperfections and defects for today's demanding applications [6].

The most used piezoelectric class is, nowadays, that of piezo ceramics. They are widely used to produce sensors. Lead Titanate ( $\text{PbTiO}_3$ ), Barium Titanate ( $\text{BaTiO}_3$ ) and Lead Zirconate Titanate (PZT) belong to this group. They are crystals with a perovskite structure and they must undergo a poling procedure to induce piezoelectricity. They can be grouped into two main categories: *hard materials* and *soft materials*. Materials in the former group can withstand a high level of electrical excitation and mechanical stress, while those in the latter group are characterized by high sensitivity and permittivity and are well suited to static applications.

The third class is that of piezo polymers. They are divided into three different categories: *bulk polymers*, *voided charged polymers* and *piezocomposite polymers*. The piezoelectric effect of piezoelectric bulk polymers is due to the molecular structure of the polymer and its orientation. One well-known bulk polymer is Polyvinylidene fluoride (PVDF): it is the most used in electromechanical devices, in underwater sonar and biomedical imaging applications. PVDF is also the most studied material in this dissertation. Voided charged polymers contain internal gas voids. These polymers behave as piezoelectric materials when the surfaces adjacent to the voids are charged up. The third subgroup of piezo polymers is that of piezo composites, obtained by mixing piezoelectric ceramics with polymers. They provide the advantages of both materials, namely the higher coupling factor and dielectric constant of ceramics and the mechanical flexibility of polymers. They are widely used for acoustic devices because they increase the performance of ultrasonic transducers [8]. Manufacturing is, however,

more expensive than for ceramics.

Figure 1.3 shows a classification of piezoelectric materials with examples of the most representative materials in each group.

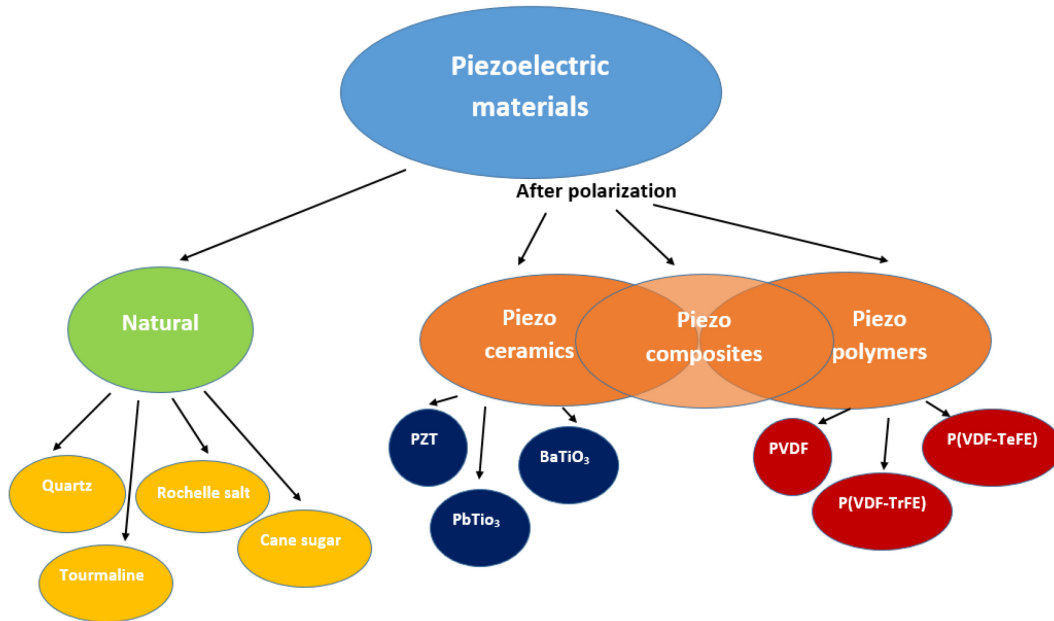


*Figure 1.3 - Classification of piezoelectric materials.*

One peculiar sub-class of piezoelectric materials is the ferroelectric materials. They have a spontaneous electric polarization that can be reversed by applying an electric field[1]. All these materials are characterized by the presence of hysteresis, a dependence of the output of the system on what happened in the past. Figure 1.4 shows a typical example of a hysteresis loop for a ferroelectric material, where P is the polarization and E the electric field.

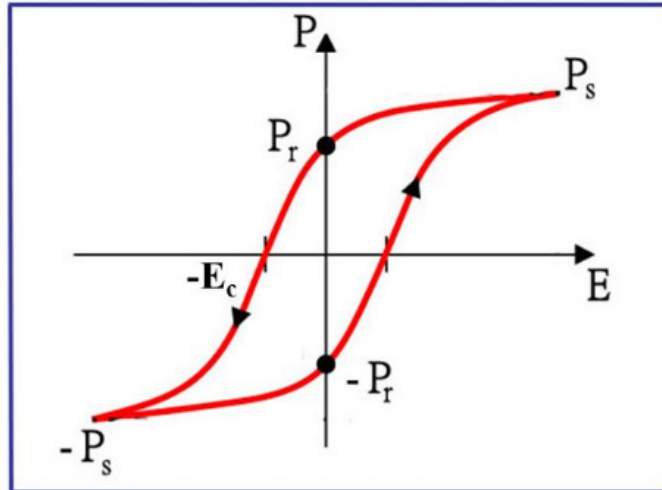


Figure 1.4 – Ferroelectric hysteresis loop.

Ferroelectric materials can be reversed from the saturation point  $-P_s$  to the saturation point  $P_s$  by applying a suitable electric field. When the field is removed, the polarisation does not disappear. The polarisation which remains after a material has been fully polarised and then had the field removed is called the *remanent polarisation* ( $P_r$ ). If the reversal field  $E_c$  is greater than the breakdown field<sup>4</sup> of the material, then the material is pyroelectric. Pyroelectric materials are able to generate electrification or electrical polarity produced in certain crystals by temperature changes [1].

### 1.3. New piezoelectric materials

Each piezoelectric material is characterized by a critical temperature, the so-called *Curie point* or *Curie temperature*. Once the Curie point has been reached, the material becomes inactive from the piezoelectric point of view. This parameter becomes crucial in specific applications, such as aerospace, automotive and aircraft, which require the materials to work at higher temperatures. Another important challenge in the development of piezoelectric materials comes from the quickly growing field of Micro Electro-Mechanical Systems (MEMS). MEMS dimensions are often in the micron range, thus requiring the miniaturization of the piezoelectric materials they are made of.

<sup>4</sup>The breakdown electric field is an important material parameter to evaluate the strength of the insulating layer. It is defined as the ratio between the breakdown electric voltage across the insulating layer and the physical thickness of the insulating layer [9]. The breakdown electric voltage is the minimum applied voltage that would cause a given insulator or electrode to break down [1].

For the above reasons, the market needs new types of piezoelectric crystals, capable of satisfying the demand for miniaturization with greater sensitivity as well as that of also working appropriately at high temperatures [6]. For this reason, some companies have carried out intensive research in cooperation with university and research centers in order to investigate new crystal compounds and to create a growing process in situ. A leader in this area is Kistler that produced its first crystal 'in house' in 1998. The crystal is called K185 and belongs to the PiezoStar group. Its piezoelectric sensitivity is 5 times higher than that of natural quartz, it has low temperature dependence, a Curie point over 600° C and a melting point above 1300° C. The process used by Kistler to produce PiezoStar is called the Czochralsky process. It takes one week to grow a crystal with a diameter of 55 [mm] and a weight of 1.8 [Kg]. PiezoStar crystals belong to the same family as langasite and have the same crystallographic class as quartz [10-11]. Figure 1.5 shows a PiezoStar crystal produced by Kistler.



*Figure 1.5 - Kistler's PiezoStar: Ø55 [mm], weight 1.8 [Kg] (Courtesy to Kistler Group).*

The most important disadvantage of PiezoStar is the high cost. Kistler also produces cheaper artificial quartz crystals for less demanding applications. Crystals are grown using a hydrothermal process in autoclaves at a pressure of 1 to 2 [Kbar], at temperatures between 350° and 400° C, for a period of 3-6 months. These crystals have high mechanical load capacity, extremely good thermal stability and are suitable up to 400° C [12]. Figure 1.6 shows ingots of artificial quartz produced by Kistler.



Figure 1.6 - Ingots of Kistler's artificial quartz (Courtesy to Kistler Group).

#### 1.4. Piezoelectric effects. Sensors and actuators.

Piezoelectric materials are characterized by the property of generating electricity when they are mechanically stressed so they can convert mechanical energy into electrical energy. This property is called the *direct effect of piezoelectricity* and is shown in Figure 1.7.

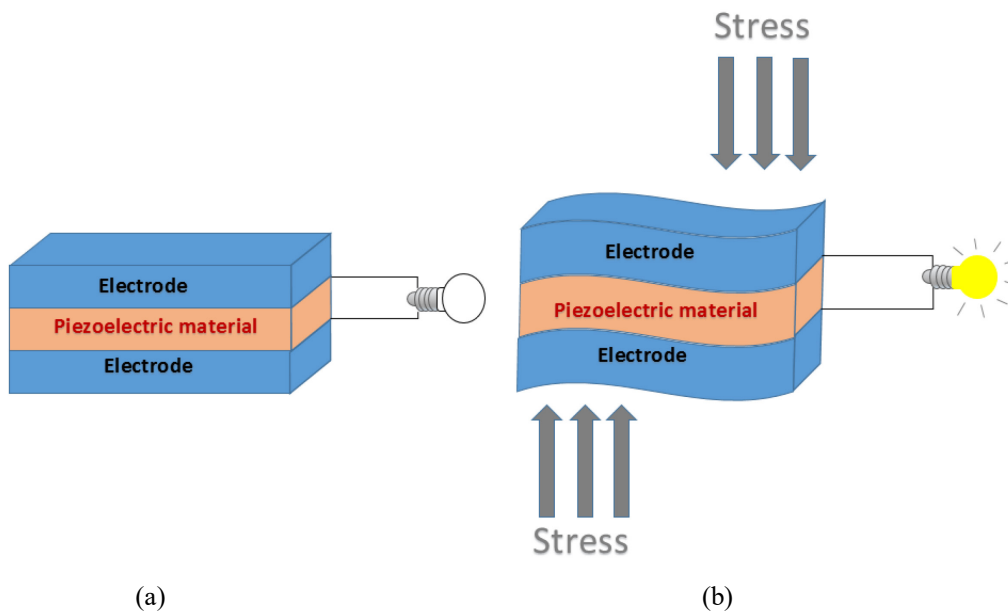
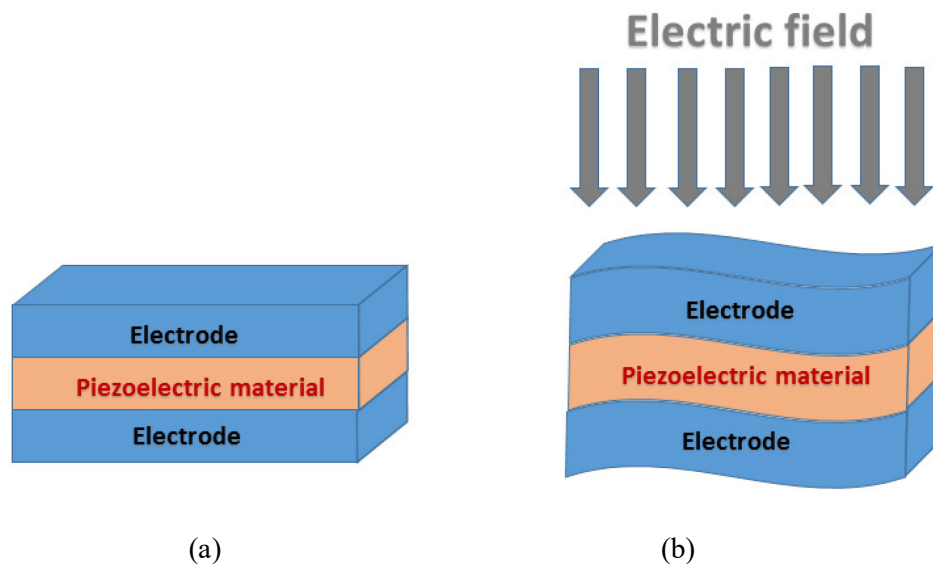


Figure 1.7 - Direct piezoelectric effect. a) Piezoelectric material at rest. b) Stressed piezoelectric material.

The voltage generated by a piezoelectric material under stress is linearly proportional to the stress applied, up to a specific value, which depends on the material properties. Mechanical compression or tension on the piezoelectric element changes its dipole moment, thus generating a voltage. Compression along the direction of polarization, or

tension perpendicular to the direction of polarization, generates a voltage of the same polarity as the poling voltage. Tension along the direction of polarization, or compression perpendicular to that direction, generates a voltage with polarity opposite to that of the poling voltage. When operating in this mode, the piezoelectric device is being used as a *sensor*. Piezoelectric sensors offer a high signal to noise ratio and high-frequency noise rejection. Therefore, they are suitable for applications that involve measuring low strain levels. Finally, they are compact, easy to embed and require moderate signal conditioning circuitry [2].

Furthermore, piezoelectric materials undergo deformation and produce strain if they are subjected to an electric field: this is the so-called *converse effect of piezoelectricity* which is shown in Figure 1.8.



**Figure 1.8 - Converse piezoelectric effect. a) Piezoelectric material at rest. b) An electric field applied deforms the piezoelectric material.**

When a voltage of the same polarity as the poling voltage is applied to a piezoelectric element, the element lengthens and its diameter becomes smaller. Whereas, when a voltage of polarity opposite to that of the poling voltage is applied, the element becomes shorter and broader. When an alternating voltage is applied to the device, the element expands and contracts cyclically, at the frequency of the applied voltage. When operated in this mode, the piezoelectric material is used as an *actuator* that converts electrical energy into mechanical energy [2].

### 1.5. Piezoelectric Constitutive Equations.

The electromechanical behaviour of piezoelectric materials is well described by the *Constitutive Equations of Piezoelectric Materials*. They explain how the stress ( $T$ ) applied to the piezoelectric material, the strain ( $S$ ), the charge-density displacement ( $D$ ) and the electric field ( $E$ ) all interact. Following the guidelines of the IEEE Standard on piezoelectricity [13], in this dissertation the piezoelectric materials are assumed to be linear, that is piezoelectric devices operated in a low electric field or under low mechanical stress.

The anisotropic behaviour of piezoelectric crystals requires the definition of a reference system. According to the IEEE Standard on Piezoelectricity [13], the plane of isotropy is called the “12-plane” or the “xy-plane” and the piezoelectric material exhibits symmetry about the 3-axis or z-axis, which is the poling axis of the material [14]. The axes orientation and their nomenclature are shown in Figure 1.9.

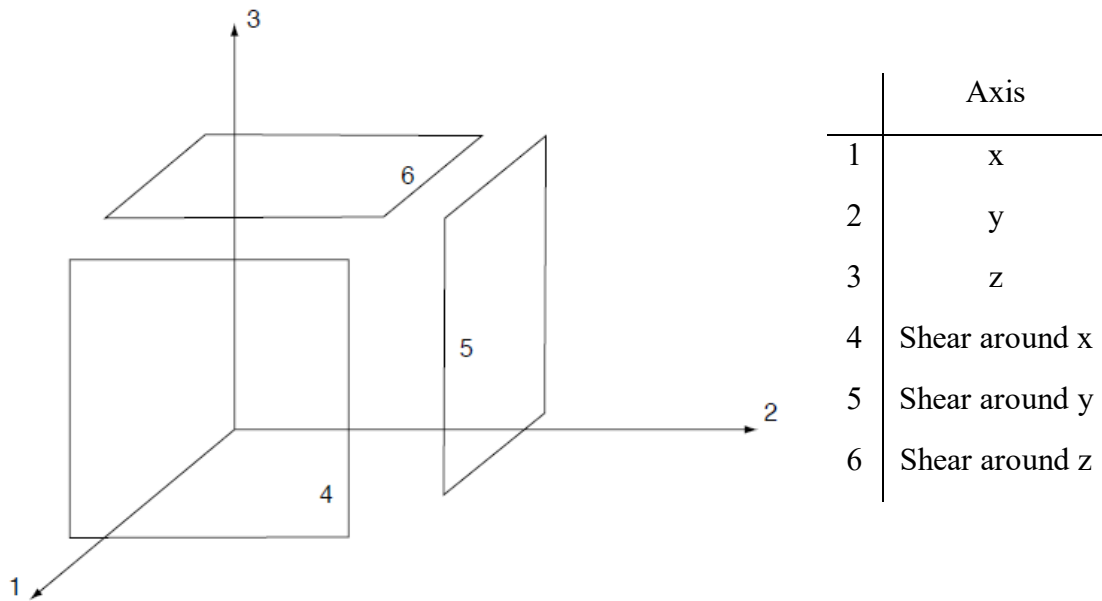


*Figure 1.9 - Axes orientation and nomenclature*

The IEEE Standard on piezoelectricity proposes four formulations for the constitutive equations that could be expressed in the tensorial form or in the matrix array form, using compressed matrix notation. In this dissertation, the matrix array form is preferred.

Each formulation has a key-name that highlights the dependent variables. The first and the most important formulation is the so-called *stress-charge form*. It is the only formulation useful for the three-dimensional continuum when there are no boundaries [13] and is expressed by equations (1.1) and (1.2).

$$T_p = c_{pq}^E S_q - e_{kp} E_k \quad (1.1)$$

$$D_i = e_{iq} S_q - \varepsilon_{ik}^S E_k, \quad (1.2)$$

where  $i, k = 1, 2, 3$ ,  $p, q = 1, 2, 3, 4, 5, 6$ ,  $c^E$  is the *elasticity matrix* (evaluated at constant electric field  $E$ );  $e$  is the *piezoelectric stress matrix* or the *coupling matrix*, and  $\varepsilon^S$  is the *dielectric matrix* (evaluated at constant mechanical strain  $S$ ) of the piezoelectric material. In the matrix form they become:

$$\begin{bmatrix} T \\ D \end{bmatrix} = \begin{bmatrix} c^E & -e^t \\ e & \varepsilon^S \end{bmatrix} \begin{bmatrix} S \\ E \end{bmatrix} \quad (1.3)$$

where the superscript  $t$  denotes the transpose matrix.

The other forms proposed by [13] for these equations are expressed in the so-called *strain-charge form* (1.4-1.5), *stress-voltage form* (1.6-1.7) and *strain-voltage form* (1.8-1.9).

$$S_p = s_{pq}^E T_q + d_{kp} E_k \quad (1.4)$$

$$D_i = d_{iq} T_q - \varepsilon_{ik}^T E_k \quad (1.5)$$

$$T_p = c_{pq}^D S_q - h_{kp} D_k \quad (1.6)$$

$$E_i = -h_{ip} S_p + \beta_{ik}^S D_k \quad (1.7)$$

$$S_p = s_{pq}^D T_q + g_{kp} D_k \quad (1.8)$$

$$E_i = -g_{iq} T_q + \beta_{ik}^T D_k. \quad (1.9)$$

It is important to underline that equations (1.1) and (1.2) are always valid while (1.4-1.9) can be used only under specified circumstances which allow some of the variables on the right hand side of the equations to be approximate to zero.

The relations among the coefficients of equations (1.4-1.9) can be written as follows.

$$c_{pr}^E s_{qr}^E = \delta_{pq} \quad (1.10)$$

$$c_{pr}^D s_{qr}^D = \delta_{pq} \quad (1.11)$$

$$\beta_{ik}^S \varepsilon_{jk}^S = \delta_{ij} \quad (1.12)$$

$$\beta_{ik}^T \varepsilon_{jk}^T = \delta_{ij} \quad (1.13)$$

$$c_{pq}^D = c_{pq}^E + e_{kp} h_{kp} \quad (1.14)$$

$$s_{pq}^D = s_{pq}^E - d_{kp} g_{kq} \quad (1.15)$$

$$\varepsilon_{ij}^T = \varepsilon_{ij}^S + D_{iq} e_{jq} \quad (1.16)$$

$$\beta_{ij}^T = \beta_{ij}^S - g_{iq} h_{jq} \quad (1.17)$$

$$e_{ip} = d_{iq} c_{qp}^E \quad (1.18)$$

$$d_{ip} = \varepsilon_{ik}^T g_{kp} \quad (1.19)$$

$$g_{ip} = \beta_{ik}^T d_{kp} \quad (1.20)$$

$$h_{ip} = g_{iq} c_{qp}^D \quad (1.21)$$

where  $i, j, k=1,2,3$ ,  $p, q, r=1,2,3,4,5,6$  and  $\delta_{pq}$  is the Kronecker delta that generates a 6x6 unit matrix,  $d$ ,  $g$  and  $h$  are an alternative form of the piezoelectric matrix,  $s^*$  is the *elastic compliance matrix*,  $\beta^*$  is the *impermittivity matrix* and the superscripts  $*$  can assume the values  $E$ ,  $D$  or  $T$  which denote that the constants are evaluated at constant electric field, or at constant electric displacement, or at constant stress, respectively.

### 1.6. Piezoelectric Coefficients.

The physical meaning of the coefficients of the matrices introduced in section 1.5 is described in this section, according to [2]. The  $lm$  index indicates that the stress, or strain is in the  $m$  direction, and the electrodes are perpendicular to the  $l$ -axis.

The piezoelectric coefficient  $d_{lm}$  is the ratio of the strain on the  $m$ -axis to the electric field applied along the  $l$ -axis, when all external stresses are constant. The  $d_{31}$  coefficient is sometimes negative because the application of a positive electric field generates a positive strain in direction 3.

The piezoelectric constant  $g_{lm}$  describes the electric field generated along the  $l$ -axis when the material is stressed along the  $m$ -axis.

The elastic compliance constant  $s_{lm}$  is the ratio of the strain in the  $l$ -direction to the stress in the  $m$ -direction, with the assumption that there is no change in stress in the other two directions.

The dielectric coefficient  $\epsilon_{lm}$  determines the charge per unit area on the  $l$ -axis due to an electric field applied on the  $m$ -axis. The relative dielectric constant is defined as the ratio of the absolute permittivity of the material to the permittivity of free space.

Another important coefficient is the *piezoelectric coupling coefficient*  $k_{lm}$ , which is not a coefficient of a piezoelectric matrix, unlike the coefficients  $d_{lm}$ ,  $g_{lm}$ ,  $s_{lm}$  and  $\epsilon_{lm}$ . It represents the ability of a piezoelectric material to transform electrical energy into mechanical energy and vice versa. This is one of the most important aspects to evaluate a transducer or an actuator and for this reason the value of this coefficient is always declared on the datasheet of piezoelectric devices.

The coupling coefficient can be written in terms of other piezoelectric constants:

$$k_{lm}^2 = \frac{d_{lm}^2}{s_{lm}^E \epsilon_{lm}^T} = g_{lm} d_{lm} E_p \quad (1.22)$$

where  $E_p$  is the Young's modulus of elasticity of the piezoelectric material considered.

### 1.7. Piezoelectric crystals and crystallography.

To solve the constitutive equations of piezoelectric materials, 21 independent elastic constants, 18 independent piezoelectric constants, and 6 independent dielectric constants are needed. Each piezoelectric material belongs to one of the 32 crystal classes which are grouped into 7 crystallographic systems: monoclinic, orthorhombic, tetragonal, trigonal, hexagonal, and cubic. Materials belonging to the same class have similar a crystallographic structure and present the same symmetry. The symmetry reduces the number of the independent elastic, piezoelectric, and dielectric constants needed to identify numerically the material considered, as explained in 1.5.

Figure 1.10 proposes a classification of materials into 32 crystal classes. Twenty of these classes correspond to piezoelectric materials. Of these, the 10 classes of materials with piezoelectric but not pyroelectric properties refer to materials that polarize under mechanical stress while the other 10 classes refer to materials that spontaneously polarize. The ferroelectric materials spontaneously polarize and have a reversible polarization.

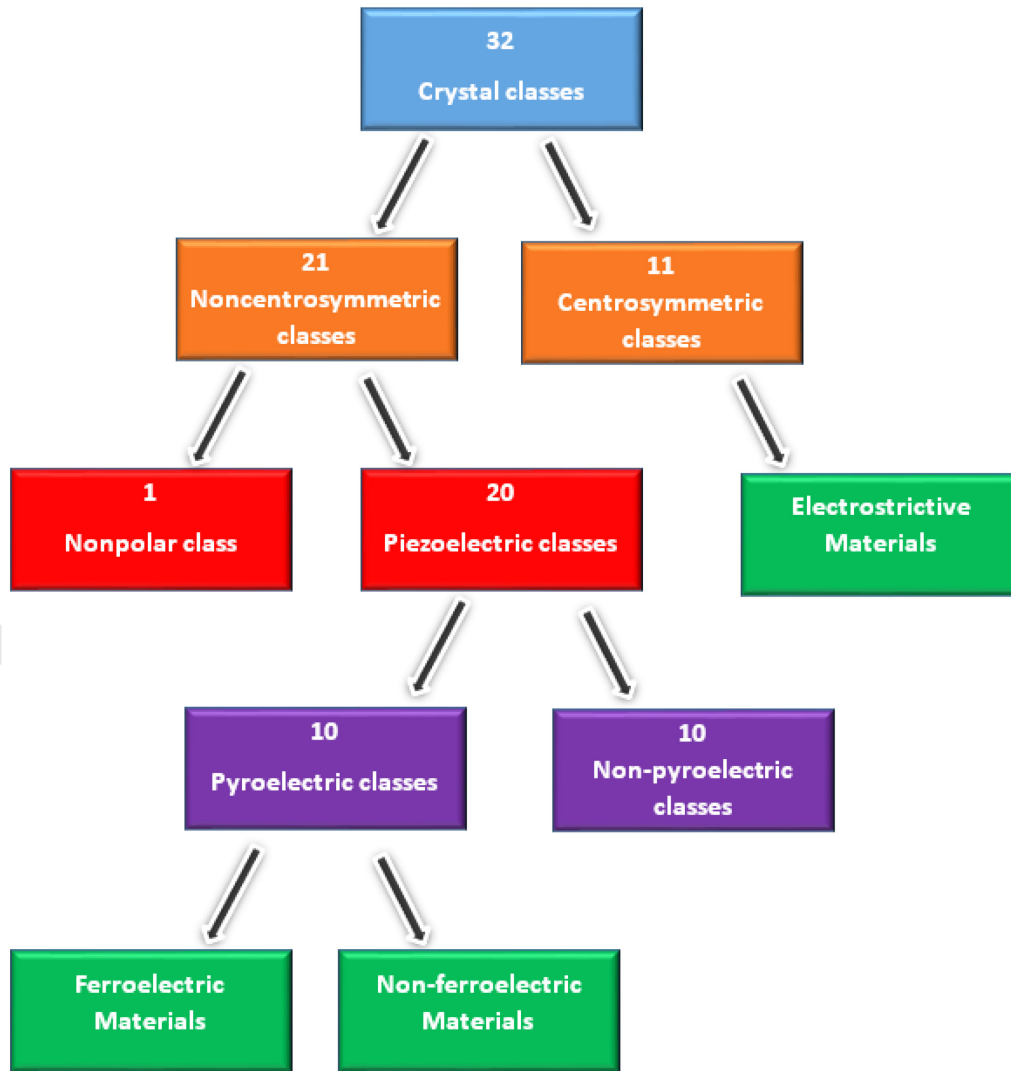


*Figure 1.10 - Classification of materials into crystal classes.*

With the Hermann-Mauguin notation, the 20 piezoelectric crystal classes are: 1, 2, m, 222, mm2, 3, 32, 3m, 4,  $\bar{4}$ , 422, 4mm,  $\bar{4}2m$ , 6,  $\bar{6}$ , 622, 6mm,  $\bar{6}2m$ , 23,  $\bar{4}3m$ .

In this dissertation, several piezoelectric materials have been analysed. They are Bismuth Germanate Oxides (BGO), Lead Zirconate Titanate (PZT) and Cadmium Sulphide (CdS), all belonging to piezoceramics, Polyvinylidene Fluoride (PVDF), belonging to piezo polymers, and quartz belonging to natural crystals. Useful information is provided about the crystal class and structure of the matrices of each material [15].

PZT and CdS belong to the 6mm crystal class of the hexagonal system [16], which has 10 independent coefficients: 5 elastic constants, 3 piezoelectric constants, and 2

dielectric constants. The structure of their constitutive matrices is depicted in Figure 1.11 [13] where the zone with red boundaries signifies the elasticity matrix, those with green boundaries signify the coupling matrix and its transpose, and that with blue boundaries signifies the dielectric matrix. The lines join numerical equalities except for complete reciprocity across the principal diagonal, which holds for all classes [2]. The open dot indicates the negative of the corresponding solid dot and X indicates:

$$2(s_{11} - s_{12}) \quad (1.23)$$

or

$$\frac{(c_{11} - c_{12})}{2}. \quad (1.24)$$

Other coefficients which are not explicitly drawn are equal to 0.

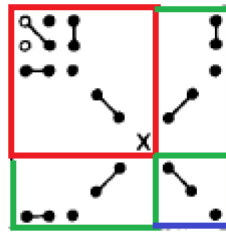


Figure 1.11 - Piezoelectric matrices for materials in the 6mm crystal class.

BGO has a cubic crystal structure, class 23 [16], which implies only 5 independent coefficients, shown in Figure 1.12 with the same notation used in Figure 1.11.

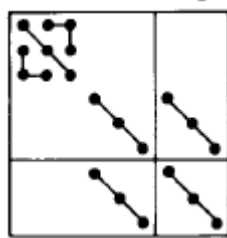


Figure 1.12 - Piezoelectric matrices for materials in the 23 crystal class.

PVDF has a very low crystallographic symmetry. Its poling is achieved by uniaxial or biaxial stretching rather than applying an electric field [6]. It belongs to the mm2 crystal class of the orthorhombic system [16] that has 17 independent coefficients, shown in Figure 1.13.

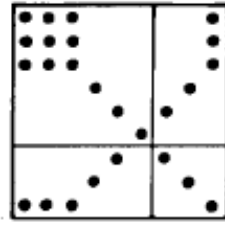


Figure 1.13 - Piezoelectric matrices for materials in the  $mm2$  crystal class.

Quartz belongs to the trigonal crystal system. There are several different kinds of quartz and each one has different matrices with a minimum of 8 to a maximum of 15 independent coefficients.

### 1.8. Electromechanical conversion of energy.

An unusual way of obtaining piezoelectric constitutive equations of piezoelectric materials is shown in this section. Such equations are usually deduced from the first law of thermodynamics, the Principle of Conservation of Energy and the concept of Electric Enthalpy Density [13], while in this case they are deduced from the constitutive equations of a two-port electromechanical capacitor device [17-19].

A two-port electromechanical device is an object able to convert mechanical energy into electrical energy and vice versa, whereas a piezoelectric actuator is an example of a two-port capacitor device, which has one electrical port and one mechanical port. The former is characterized by a scalar electric potential  $\varphi(\tau)$  and electrical current  $i(\tau)$ , where  $\tau$  represents the time, and the latter is characterized by velocity  $v(\tau)$  and force  $F(\tau)$ . Ideally these devices are reversible, so power flows from the electrical to the mechanical port and vice versa. In the first case, they behave as motors and transform electric power into mechanical power. Alternatively, they convert mechanical power into electrical power so they behave as generators [19].

A capacitive two-port device is able to convert power, using a capacitive element with a charge  $Q(\tau)$ . A scheme of this device is depicted in Figure 1.14.

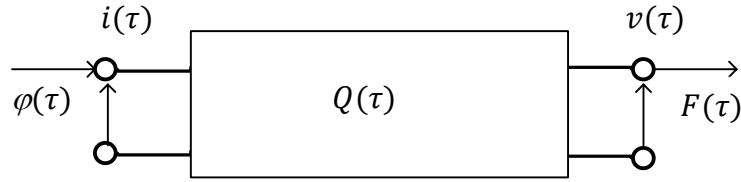


Figure 1.14 - Capacitive two-port device

The behaviour of this device is described by the following constitutive equations:

$$\varphi(\tau) = \varphi(Q(\tau), x(\tau)) \quad (1.25)$$

$$F(\tau) = F(Q(\tau), x(\tau)) \quad (1.26)$$

where  $x(\tau)$  is the generic displacement.

Equations (1.25) and (1.26) are generic and need to be specified for each different electrostatic interaction.

The absorbed power  $P(\tau)$  of a two-port capacitor device is the difference between input power and output power:

$$P(\tau) = \varphi(\tau) i(\tau) - F(\tau)v(\tau) \quad (1.27)$$

where:

$$i(\tau) = \frac{dQ(\tau)}{d\tau} \quad (1.28)$$

and

$$v(\tau) = \frac{dx(\tau)}{d\tau}, \quad (1.29)$$

so considering the energy  $W(Q, x)$ :

$$dW(Q, x) = P(\tau) d\tau = \varphi(\tau) dQ - F(\tau) dx \quad (1.30)$$

It is always possible to write:

$$dW(Q, x) = \frac{\partial W(Q, x)}{\partial Q} dQ + \frac{\partial W(Q, x)}{\partial x} dx \quad (1.31)$$

and comparing (1.30) and (1.31):

$$\varphi(Q, x) = \frac{\partial W(Q, x)}{\partial Q} \quad (1.32)$$

and:

$$F(Q, x) = - \frac{\partial W(Q, x)}{\partial x}. \quad (1.33)$$

Equation (1.33) underlines the dependence of force  $F$  on the charge and deformation [19].

Considering the co-energy  $dW^*(\varphi, x)$ :

$$W^*(\varphi, x) = \varphi Q - W(Q, x) \quad (1.34)$$

so:

$$dW^*(\varphi, x) = \varphi dQ + Q d\varphi - dW(Q, x) \quad (1.35)$$

but for (1.30):

$$\varphi(\tau) dQ - dW(Q, x) = F(\tau) dx \quad (1.36)$$

so:

$$dW^*(\varphi, x) = Q(\tau) d\varphi + F(\tau) dx. \quad (1.37)$$

It is always possible to write:

$$dW^*(\varphi, x) = \frac{\partial W^*(\varphi, x)}{\partial \varphi} d\varphi + \frac{\partial W^*(\varphi, x)}{\partial x} dx \quad (1.38)$$

and comparing (1.37) and (1.38):

$$Q(\varphi, x) = \frac{\partial W^*(\varphi, x)}{\partial \varphi} \quad (1.39)$$

and:

$$F(\varphi, x) = \frac{\partial W^*(\varphi, x)}{\partial x}. \quad (1.40)$$

Equation (1.40) underlines the dependence of force  $F$  on the electrical potential and deformation [19].

Assuming a linear dependence of the charge  $Q$  from the scalar potential  $\varphi(\tau)$ :

$$Q(\varphi, x) = C(x) \varphi(\tau) \quad (1.41)$$

where  $C(x)$  is the capacitance of the capacitor, expressed as a function of the mechanical displacement  $x(\tau)$ . According to (1.41) and (1.32):

$$W(Q, x) = \frac{1}{2} \frac{Q^2(\tau)}{C(x)} \quad (1.42)$$

subsequently, from (1.42) and (1.33):

$$F(Q, x) = -\frac{Q^2}{2} \frac{d}{dx} \frac{1}{C(x)} \quad (1.43)$$

or from (1.40):

$$F(\varphi, x) = \frac{\varphi^2}{2} \frac{d}{dx} C(x). \quad (1.44)$$

This model can be used to describe the electrostatic behaviour of a capacitive two-port system with a Single Degree of Freedom (SDoF).

A piezoelectric crystal is an example of a capacitive reversible electro-mechanical two-port system that works as actuator. Its physical characterization can be expressed by the usual electromechanical quantities, with the following constitutive equations [19]:

$$F(\varphi, x) = k_e x(\tau) - c_e \varphi(\tau) \quad (1.45)$$

$$Q(\varphi, x) = c_e x(\tau) + C(x) \varphi(\tau) \quad (1.46)$$

where  $c_e \left[ \frac{\text{N}}{\text{V}} \right]$  is the piezoelectric charge constant,  $k_e \left[ \frac{\text{N}}{\text{m}} \right]$  is the mechanical stiffness constant of the crystal. Equation (1.46) is the same as (1.41), which describes a purely electrostatic capacitor behaviour, except for the first term  $c_e x(\tau)$  on the right hand side of the equation. This charge term is due to the mechanical deformation of the system.

Assuming the system to act as a parallel plate capacitor:

$$C = \frac{\varepsilon^S A}{d} \quad (1.47)$$

$$E = \frac{\varphi(\tau)}{d} \quad (1.48)$$

where  $\varepsilon^S \left[ \frac{\text{F}}{\text{m}} \right]$  is the dielectric constant measured at constant strain  $S$ ,  $d$  is the distance between the two plates of the capacitor and  $A$  their surface,  $E$  is the electric field; substituting (1.47) and (1.48) in (1.46) and dividing all the members of equations (1.45) and (1.46) by an arbitrary surface equal to that of capacitor plates  $A$ :

$$\frac{F(\varphi, x)}{A} = \frac{k_e}{A} x(\tau) - \frac{c_e}{A} \varphi(\tau) \quad (1.49)$$

$$\frac{Q(\varphi, x)}{A} = \frac{c_e}{A} x(\tau) + \varepsilon^S E. \quad (1.50)$$

So equations (1.49) and (1.50) can be expressed as follows:

$$T = c^E S - e E \quad (1.51)$$

$$D = e S + \varepsilon^S E \quad (1.52)$$

where  $T = \frac{F}{A} \left[ \frac{\text{N}}{\text{m}^2} \right]$  is the stress,  $S = \frac{x}{d}$  is the strain,  $c^E = \frac{k_e d}{A}$  [Pa] is the elastic constant, measured at constant electric field,  $e = \frac{c_e d}{A} \left[ \frac{\text{C}}{\text{m}^2} \right]$  is the piezoelectric constant,

$D = \frac{q}{A} \left[ \frac{C}{\text{m}^2} \right]$  is the electric displacement.

Equations (1.51) and (1.52) are the piezoelectric constitutive equations expressed in the stress-charge form, as (1.1) and (1.2).

## 1.9. Conclusions.

Piezoelectric materials are the main topic of this chapter. They have been described with all properties that enable their classification. The main piezoelectric groups have been analysed with some examples of materials for each group. Moreover, the crystal classes concerning these materials have been considered. The mathematical model of constitutive equations, useful to describe the behaviour of piezoelectric materials has been presented. All the information provided is useful to understand the following chapters and the choices made by the authors in each situation.

The chapter closes with a novel contribution to the field: an in-depth study of the electromechanical conversion of energy applied to a capacitive two-port device and its relation to the constitutive equations of piezoelectric devices.

## References.

- [1] <http://www.dictionary.com>
- [2] Moheimani Reza S.O., Fleming A.J. "Piezoelectric Transducers for Vibration Control and Damping". Springer Science & Business Media, 2006.
- [3] Curie J., Curie P. "Développement par compression de l'électricité polaire dans les cristaux hémihédres à faces inclinées" [Development, via compression, of electric polarization in hemihedral crystals with inclined faces]. Bulletin de la Société minéralogique de France, 1880. 3: 90–93.
- [4] Lippmann M.G. "On the Principle of the conservation of electricity". 1881, Taylor & Francis, pp.151-154.
- [5] Tichý, J., Erhart, J., Kittinger, E., Prívratská, J. "Fundamentals of piezoelectric sensorics: mechanical, dielectric, and thermodynamical properties of piezoelectric materials". Springer Science & Business Media, 2010.
- [6] Nakamura K. "Ultrasonic transducers". Woodhead Publishing Limited, 2012.
- [7] <https://www.kistler.com/?type=669&fid=96&model=download>
- [8] Ramadan K.S., Sameoto D., Evoy S. "A review of piezoelectric polymers as functional materials for electromechanical transducers." Smart Materials and Structures, 2014, Vol. 23, No.3.
- [9] Lin H.C., Ye P.D., Wilk G..D. "Leakage current and breakdown electric-field studies on ultrathin atomic-layer-deposited Al<sub>2</sub>O<sub>3</sub> on GaAs.". Applied physics letters 2005, Vol. 87, No. 18.
- [10] Cavalloni C., Sommer R. "PiezoStar Crystals. A New Dimension in Sensor Technology ". Kistler Special Print 920-240e-07, 2003.
- [11] Mill B.V., Pisarevsky Y.V. "Langasite-type materials: from discovery to present state," Frequency Control Symposium and Exhibition, 2000. Proc. of the 2000 IEEE/EIA International, 2000, pp. 133-144.
- [12] [https://sem.org/wp-content/uploads/2016/03/kistler\\_PiezoStar.pdf](https://sem.org/wp-content/uploads/2016/03/kistler_PiezoStar.pdf)
- [13] An American National Standard IEEE standard on piezoelectricity, ANSI/IEEE Std 176–1987, The institute of Electrical and Electronics Engineers Inc. New York, USA, 1988.

- [14] Erturk A., Inman D.J. "Piezoelectric Energy Harvesting". John Wiley and Sons, Ltd., Publication, United Kingdom, 2011.
- [15] **Acciani G., Di Modugno F., Gelao G. "Comparative Studies of Piezoelectric Harvester Devices". Energy Harvesting: Technology, Methods and Applications, Nova Science Publishers, 2016, pp. 1-18,**
- [16] Martienssen W., Warlimont H. "Condensed Matter and Materials Data", Springer Berlin Heidelberg, 2005.
- [17] **Acciani G., Di Modugno F., Giaquinto A., Maiullari D., Dimucci A., Fornarelli G. "Models of Piezoelectric Materials for Transduction and Energy Harvesting",. Advances in Materials Science Research. Nova Science Publishers, 2015, Vol. 19, pp. 1-42.**
- [18] **Acciani G., Di Modugno F., Amoruso V. "An electromechanical model for harvesting simulation", Proc. of 1st Workshop on the State of the Art and Challenges of Research Efforts at POLIBA, 2014.**
- [19] Bona, B. "Dynamic modelling of mechatronic systems" CELID, 2013, pp. 321.

## *2. Chapter 2*

### *A mathematical model for mechanical vibrations*

The piezoelectric effect and the constitutive equations underlines the importance of stress and strain for piezoelectric materials. Different kinds of stress which can be applied to the piezoelectric materials are analysed in this chapter. Mechanically induced vibrations are examples of these, such as those produced by earthquakes, wind, water and the sea. Their behaviour can be described using a mathematical model that involves a covariance analysis of stochastic linearised systems, in the case of non-stationary excitation. The non-stationary Lyapunov differential matrix covariance equation is considered to model the problem. It is solved for the equivalent linearised system. A numerical algorithm which updates the linearised system coefficient matrix at each step is used to solve the equations. The technique used is a predictor-corrector procedure applied to a backward Euler method for the covariance analysis matrix system. The procedure is applied to a significant applicative case: the seismic response of a Bouc-Wen Single Degree of Freedom (SDoF) system. Accuracy and computational costs are analysed showing the efficiency of the proposed procedure.

The chapter closes with focus on boundary conditions useful to correctly define a vibrational problem.

## 2.1 Introduction

The direct and the converse piezoelectric effects and the reaction of piezoelectric materials to stress applied were well explained in chapter 1, in particular in sections 1.4 and 1.6. The deformation is the result of a stress applied to the material. In order to induce the material to achieve the desired configuration, some deformations are deliberately forced, other are naturally induced. Examples of induced stress come from bending, compression or traction.

When a piezoelectric material is bent by an applied force, the farthest fibres from the force undergo stretching so they expand, while the nearest ones undergo compression so they contract, as shown in Figure 2.1.

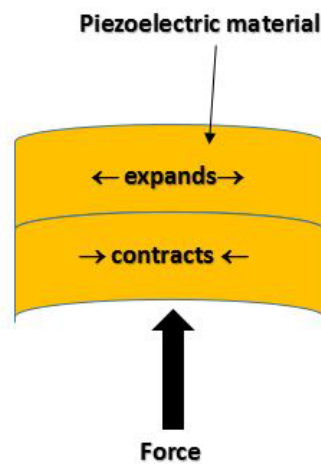


*Figure 2.1 - Bending of a piezoelectric material*

Charge develops across the piezoelectric layer in an effort to counteract the imposed strain. This property is opportunely exploited by actuators and sensors.

The piezoelectric effect caused by compression is exploited by *accelerometers*. They are electromechanical devices able to measure acceleration forces. These forces may be static, such as the constant force of gravity, or dynamic, caused by movement or vibrations. Figure 2.2 shows the structure of an accelerometer produced by Kistler, made using a PiezoStar crystal [1].

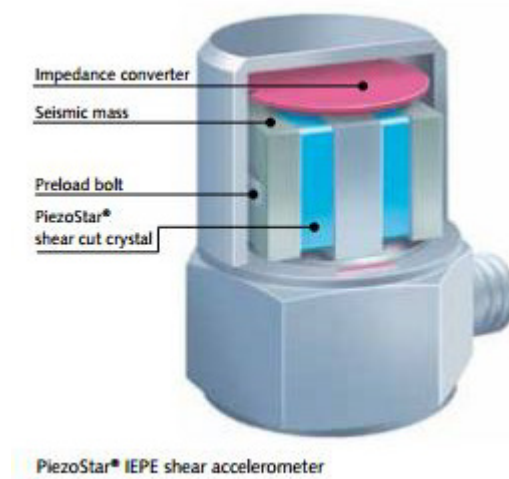


*Figure 2.2 - Structure of an accelerometer (Courtesy of Kistler Group).*

Another important stress for piezoelectric materials is traction. A very interesting development in this field is Energy-Generating Rubber, a novel flexible material which was developed in 2015 by Ricoh Company Ltd., in collaboration with professor Takahiro Yamamoto of the Tokyo University of Science. This material converts pressure and vibrations into electrical energy with high efficiency, overcoming some of the drawbacks which limit the employment of ceramics and polymers as energy harvesters, despite their widespread use as sensors and acoustic emitters. Fragility, weight, toxicity and cost are typical problems of ceramic piezoelectric devices, while polymeric ones have weak action.

The Energy-Generating Rubber is claimed to generate as high a level of electricity as ceramics without their drawbacks and it is a soft and flexible sheet [2].

The piezoelectric materials and devices investigated in this dissertation undergo only natural vibrations and in particular fluid flowing induced vibrations such as those produced by wind. For this reason a mathematical model useful to describe natural vibrations had to be developed and is described in this chapter [3-5].

## **2.2 A mathematical model**

Many vibrational problems deal with loads which have an intrinsically non-deterministic nature, such as earthquakes, wind pressure, rain or sea waves. This intrinsic random nature of inputs requires a random dynamic analysis.

In the analysis of linear systems, the physical solution can be obtained by using standard analytical approaches. These approaches can describe response statistics considering input parameters, both in time and in frequency domains but they do not work for most non-linear systems. Formal solutions to non-linear systems are only available for some simple cases [6]. In the analysis of deterministic non-linear systems, one of the most effective methods is the perturbation method, which was first proposed by Poincare and then extensively studied [7]. A corresponding method in random analysis of non-linear systems has also been studied [8-9]. An alternative approach is the ‘statistical linearization method’, also referred to as ‘stochastic linearization’ or ‘equivalent linearization’ in the literature [10-14]. This technique was proposed independently but simultaneously by Booton [15], Kazakov [16], Lu and Evan-Iwanowski [17].

In many cases, there is a circular interdependency between linearization coefficients and stochastic response. An iterative algorithm can represent a good solution to break this complex loop. The complexity of the procedure usually increases with non-stationary situations, where evolutive state space and joint probability density induce time variant stochastic equivalent linearization coefficients. The problem is even more complex when the inputs are also non-stationary, for example when external forces such as seismic actions are considered. The inner evolutive nature of the input has a big impact on responses, and this has been observed both in general cases, such as Duffing models [8], or real engineering problems, such as real buildings or bridges [18-19].

A multi-correlated input approach is better suited to non-stationary situations. Unfortunately, it produces numerical difficulties because the input should be defined using processes modulated in amplitude and/or in frequency [20]. It is quite difficult to obtain analytical solutions for random responses to this kind of problem and few solutions are described in the literature [21-23].

In this section a computational method is described, aimed at solving these issues. It has a reduced computational cost due to some properties of covariance matrices [24]. A numerical approach for space state evolutive covariance matrix evaluation is proposed. The non-linear behaviour is overcome by implementing the equivalent statistical linearization technique, and the Lyapunov matrix differential equations are used to solve a Euler implicit integration scheme, studied as an expansion of a similar one proposed

for linear systems [25-26]. The algorithm is thus described and a predictor-corrector scheme for a step by step linearised coefficient update is proposed.

The algorithm proposed for the numerical solution is applied to a non-stationary Gaussian filtered input, modulated in amplitude and frequency. It acts on a generic SDoF base excited system and it is modelled on the well known Bouc-Wen model. Its effectiveness is evaluated, determining the response and sensitivity to the integration time step.

### 2.2.1. Statistical Linearization approach

The Statistical Linearization approach basically consists of replacing non-linear terms with linear ones. The coefficients of these new terms are determined by minimizing a stochastic measurement of differences between the two solutions. This stochastic measurement needs knowledge of state space (system displacement and velocity) and joint probability distribution, but these elements are often unknown.

Consider the non-linear SDoF system:

$$m\ddot{x} + g(x, \dot{x}) = \xi(t) \quad (2.1)$$

where  $m$  is the mass,  $g(x, \dot{x})$  is the non-linear force including the non-linear damping and restoring forces and  $\xi(t)$  is a stochastic excitation. The main idea behind a statistical linearization approximation is to replace Equation (2.1) with an equivalent linear system:

$$m\ddot{y} + c_{eq}\dot{y} + k_{eq}y = \xi(t) \quad (2.2)$$

where  $c_{eq}$  and  $k_{eq}$  are the equivalent damping and stiffness, respectively. The error  $e_{ex}$  (2.3) between the solutions of the two systems can be minimized with the mean-square method.

$$e_{ex} = m\ddot{x} + g(x, \dot{x}) - (m\ddot{y} + c_{eq}\dot{y} + k_{eq}y) \quad (2.3)$$

In other words, Equation (2.3) represents the error made by approximating the solution for Equation (2.1) to the solution for Equation (2.2). However, the response  $x$  of the non-linear system is unknown and, therefore, the error so defined would be intractable. In contrast, obtaining the equivalent response  $y$  in Equation (2.2) is easier. Thus it is

better to solve Equation (2.2) instead of Equation (2.1), defining the error by Equation (2.3) but where  $x$  is replaced by  $y$ :

$$e_{app} = g(y, \dot{y}) - c_{eq}\dot{y} - k_{eq}y \quad (2.4)$$

In order to choose the best equivalent damping  $c_{eq}$  and the equivalent stiffness  $k_{eq}$ , it is necessary to minimize the error using a statistical procedure that starts from the natural expectation of the mean value to be null,

$$E\langle e_{app} \rangle = 0 \quad (2.5)$$

where  $E\langle \bullet \rangle$  denotes the mathematical expectation. In the following  $E\langle \bullet^2 \rangle$  denotes the second-order moment, namely the mean-square error, which has to be minimized:

$$E\langle e_{app}^2 \rangle = E\langle (g(y, \dot{y}) - c_{eq}\dot{y} - k_{eq}y)^2 \rangle \quad (2.6)$$

This requires that:

$$\frac{\partial E\langle e_{app}^2 \rangle}{\partial c_{eq}} = 0 \quad (2.7)$$

and

$$\frac{\partial E\langle e_{app}^2 \rangle}{\partial k_{eq}} = 0 \quad (2.8)$$

Equations (2.7) and (2.8) yield two linear equations and, therefore, give the optimal values of  $c_{eq}$  and  $k_{eq}$ :

$$c_{eq} = \frac{E\langle g(y, \dot{y})\dot{y} \rangle E\langle y^2 \rangle - E\langle g(y, \dot{y})y \rangle E\langle y\dot{y} \rangle}{E\langle \dot{y}^2 \rangle E\langle y^2 \rangle - (E\langle y\dot{y} \rangle)^2} \quad (2.9)$$

$$k_{eq} = \frac{E\langle g(y, \dot{y})y \rangle E\langle \dot{y}^2 \rangle - E\langle g(y, \dot{y})\dot{y} \rangle E\langle y\dot{y} \rangle}{E\langle \dot{y}^2 \rangle E\langle y^2 \rangle - (E\langle y\dot{y} \rangle)^2} \quad (2.10)$$

It is important to note that to obtain the optimal values of  $c_{eq}$  and  $k_{eq}$ , in this procedure in both (2.9) and (2.10) the joint Probability Density Function (PDF)  $p_z(z)$  of the state

space  $z = \begin{pmatrix} y \\ \dot{y} \end{pmatrix}$  is needed.

This means that to solve the linear stochastic set of vibration equations (2.2), the values of  $c_{eq}$  and  $k_{eq}$  are needed. So a circular interdependency is produced for this problem and therefore, an iterative algorithm can be used to break the loop. It consists of starting from a tentative value for both the linearised coefficients  $c_{eq}^{(0)}$  and  $k_{eq}^{(0)}$ , then by solving (2.2), evaluating a first attempt of  $p_z^{(0)}(z)$  and then evaluating new values of  $c_{eq}^{(1)}$  and  $k_{eq}^{(1)}$  by (2.9) and (2.10). Subsequently the procedure is iterated until the distance between two subsequent iteration values becomes smaller than a fixed tolerance.

This scheme is illustrated in Figure 2.3, where the superscripts represent the steps of iteration and  $p_z(z)$  represents the probabilistic information (e.g. the joint statistics or PDF). The iteration could reach the end if the error of  $c_{eq}$  and  $k_{eq}$  between two subsequent iterations is limited within the tolerance:

$$\|c_{eq}^{(j+1)} - c_{eq}^{(j)}\| < \varepsilon_{c_{eq}} \quad (2.11)$$

$$\|k_{eq}^{(j+1)} - k_{eq}^{(j)}\| < \varepsilon_{k_{eq}} \quad (2.12)$$

or the error of the probabilistic characteristics of the state space  $z$  is limited within the tolerance:

$$\left\| \left( E \langle y^2 \rangle \right)^{(j+1)} - \left( E \langle y^2 \rangle \right)^{(j)} \right\| < \varepsilon_{E \langle y^2 \rangle} \quad (2.13)$$

$$\left\| \left( E \langle \dot{y}^2 \rangle \right)^{(j+1)} - \left( E \langle \dot{y}^2 \rangle \right)^{(j)} \right\| < \varepsilon_{E \langle \dot{y}^2 \rangle} \quad (2.14)$$

where  $\varepsilon$ , are the corresponding error tolerances.

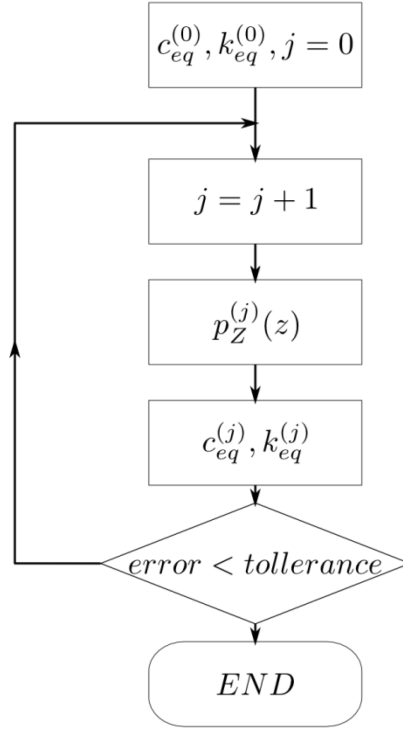


**Figure 2.3 - Scheme to evaluate the best equivalent damping  $c_{eq}$  and the equivalent stiffness  $k_{eq}$**

In a more general case of Multi-Degree of Freedom (MDoF) mechanical problems, the state space  $\bar{z} = \begin{pmatrix} \bar{y} \\ \dot{\bar{y}} \end{pmatrix}$  is considered, where  $\bar{y}$  is the displacement vector and  $\dot{\bar{y}}$  is the velocity vector, both with  $n$  degrees of freedom. In this case the problem has to be considered as a linearised equation in the space  $\bar{z}$ .

$$\dot{\bar{z}} = \mathbf{A}_{eq} \bar{z} + \bar{\xi} \quad (2.15)$$

In Equation (2.15)  $\mathbf{A}$  is the state space matrix; its coefficients depend on the state space covariance matrix  $R_{zz}$  :

$$R_{zz} = E \left\langle \bar{z} \bar{z}^T \right\rangle \quad (2.16)$$

that is, the solution of the stationary Lyapunov matrix equation:

$$\mathbf{A}_{eq} (\mathbf{R}_{zz}) \mathbf{R}_{zz} + \mathbf{R}_{zz} \mathbf{A}_{eq}^T (\mathbf{R}_{zz}) + \mathbf{B} = \mathbf{0} \quad (2.17)$$

expressed in the following form:

$$\mathbf{A}_{eq} = \mathbf{A}_{eq}(\mathbf{R}_{zz}) \quad (2.18)$$

A scheme similar to that proposed in Figure 2.3 is applicable to solve the problem of (2.17): the problem so stated is well known in the literature and many standard and commercial codes to solve the Lyapunov equation in (2.17) exist, such as the Lyap command in Matlab.

The scheme proposed only holds for stationary problems, while non-linear and non-stationary ones require the solution of a time dependent Lyapunov Equation.

It is important to note that if the response is a non-stationary process, such determined optimal values of  $c_{eq}$  and  $k_{eq}$  are time variant and therefore, the equivalent system in Equation (2.2) or in (2.17) for a general non-linear system is a time-variant linear system.

The first observation that can be made is that the state matrix has to be updated at each integration step because linearised coefficients are implicitly dependent on the same unknown covariance matrix  $R_{zz}$ . In this case  $R_{zz}$  is time dependent:

$$\mathbf{A}_{eq} = \mathbf{A}_{eq}(\mathbf{R}_{zz}(t), t) \quad (2.19)$$

Here the state space covariance matrix is the solution of non-stationary Lyapunov equation in the form:

$$\dot{\mathbf{R}}_{zz}(t) = \mathbf{A}_{eq}(\mathbf{R}_{zz}, t)\mathbf{R}_{zz}(t) + \mathbf{R}_{zz}(t)\mathbf{A}_{eq}^T(\mathbf{R}_{zz}, t) + \mathbf{B}(t) \quad (2.20)$$

where  $\dot{\mathbf{R}}_{zz} = \frac{d}{dt} \mathbf{R}_{zz}$ .

To solve this specific problem a simple numerical predictor-corrector algorithm is described in this section, using an iterative procedure. It updates the linearised system matrix at each step as its time varying coefficients. The total duration  $[0, T]$  is divided into  $m$  equal sub periods  $\Delta t = t^{(h+1)} - t^{(h)}$  ( $h=0, 1, \dots, m-1$ ) and in each sub-period  $\Delta t$  a linear variation of the time derivative covariance matrix  $\dot{\mathbf{R}}(t)$  is assumed.

A backward Euler method is used as predictor:

$$\text{Predictor} \quad \mathbf{R}_{(h+1)}^p = \mathbf{R}_{(h)} + \Delta t \dot{\mathbf{R}}_{(h)} \quad (2.21)$$

while the trapezoidal method is used as corrector:

$$\text{Corrector} \quad \mathbf{R}_{(h+1)}^c = \mathbf{R}_{(h)} + \frac{\Delta t}{2} \left( \dot{\mathbf{R}}_{(h)} + \dot{\mathbf{R}}_{(h+1)}^p \right) \quad (2.22)$$

where the symbol  $a_{(h)}$  denotes the generic quantity  $a$  evaluated at time  $t = h\Delta t$ . For each integration step,  $h$  is evaluated as a prediction of the covariance matrix with (2.21); then it is used to obtain a corrected value using the implicit scheme in (2.22).

Moreover, the coefficients of linearised state matrix  $\mathbf{A}$  depend on the covariance matrix so there is an implicit evolution of  $\mathbf{A}$ . In this way the system matrix  $\mathbf{A}_{eq}$  has to be updated at each time, depending on the covariance matrix at the same time:

$$\mathbf{A}_{eq(h)} = \mathbf{A}_{eq} \left( \mathbf{R}_{(h)}, t_h \right). \quad (2.23)$$

At step  $h+1$ , the evaluation of generic unknown covariance  $\mathbf{R}_{(h+1)}$  needs the still unknown state space matrix  $\mathbf{A}_{eq(h+1)}$  so equation (2.23) is still implicit, while  $\mathbf{A}_{eq(h)}$  is known because it only depends on  $\mathbf{R}_{(h)}$ . So a first evaluation of  $\mathbf{A}_{eq(h)}$  is obtained using (2.23) with predictor  $\mathbf{R}_{(h+1)}^p$  from (2.21). Then a second more accurate evaluation is obtained using (2.23) with corrector  $\mathbf{R}_{(h+1)}^c$  from (2.22). For a more accurate evaluation of  $\mathbf{A}_{eq(h+1)}$  and  $\mathbf{R}_{(h+1)}$ , an iterative scheme based on a modification of (2.22) is then possible.

Starting from the corrector evaluation of the covariance matrix  $\mathbf{R}_{(h+1)}^1 = \mathbf{R}_{(h+1)}^c$ , (2.22) is updated with the following scheme:

$$\mathbf{R}_{(h+1)}^{j+1} = \mathbf{R}_{(h)} + \frac{\Delta t}{2} \left( \dot{\mathbf{R}}_{(h)} + \dot{\mathbf{R}}_{(h+1)}^j \right) \quad (2.24)$$

$$\mathbf{A}_{eq(h)}^{j+1} = \mathbf{A}_{eq} \left( \mathbf{R}_{(h+1)}^{j+1}, t_h \right) \quad (2.25)$$

$$j = j + 1. \quad (2.26)$$

This iteration scheme ends when a stop criterion is met; usually the stop criterion is applied to linearised coefficients.

$$\mathcal{E}_{A_{eq}}^{(j+1)} = \left\| \mathbf{A}_{eq} \left( \mathbf{R}_{(h+1)}^{j+1} \right) - \mathbf{A}_{eq} \left( \mathbf{R}_{(h+1)}^j \right) \right\| \leq \mathcal{E}_{\max} \quad (2.27)$$

In order to obtain knowledge on the covariance matrix evolution, the scheme proposed has to be repeated for each time step integration and must be solved in sequence for each time value  $t_{(h)}$ , starting from  $t_0 = 0$  (which has  $\mathbf{R}_{(0)} = 0$  as covariance matrix value).

In this way, the  $m$  unknown matrices  $\mathbf{R}_{(h)}$ ,  $h=1, \dots, m$ , can be determined, defining statistics of response.

### 2.2.2. Predictor - corrector algorithm for Lyapunov equation integration

The integration scheme, written in pseudo-code, is the following.

#### Initial conditions

$$h=1, t_1=0; \mathbf{R}_1 = \mathbf{R}(t=0)=0, \mathbf{A}_1 = \mathbf{A}_{eq}(\mathbf{R}_1);$$

**while** ( $t_{h+1} \leq t_{TOT}$ )

$$\begin{aligned} t_{h+1} &= t_h + \Delta t; \\ \mathbf{R}_{(h+1)}^p &= \mathbf{R}_{(h)} + \Delta t \dot{\mathbf{R}}_{(h)} \\ \dot{\mathbf{R}}_{h+1}^p &= \mathbf{A}_{eq(h)} \mathbf{R}_{(h+1)}^p + \mathbf{R}_{(h+1)}^p \mathbf{A}_{eq(h)}^T + \mathbf{B}_{(h+1)} \\ \mathbf{R}_{(h+1)}^c &= \mathbf{R}_{(h)} + \frac{\Delta t}{2} \left( \dot{\mathbf{R}}_{(h)} + \dot{\mathbf{R}}_{(h+1)}^p \right) \\ \dot{\mathbf{R}}_{h+1}^c &= \mathbf{A}_{eq(h)} \mathbf{R}_{(h+1)}^c + \mathbf{R}_{(h+1)}^c \mathbf{A}_{eq(h)}^T + \mathbf{B}_{(h+1)} \\ j &= 1; \\ \mathbf{R}_{(h+1)}^1 &= \mathbf{R}_{(h+1)}^c \\ \mathbf{A}_{eq(h+1)}^1 &= \mathbf{A}_{eq} \left( \mathbf{R}_{(h+1)}^1 \right); \end{aligned}$$

**while**  $\left\| \mathbf{A}_{h+1}^{(j+1)} - \mathbf{A}_{h+1}^{(j)} \right\| \leq \mathcal{E}_{A_{eq}}$

$$\mathbf{R}_{(h+1)}^{j+1} = \mathbf{R}_{(h)} + \frac{\Delta t}{2} \left( \dot{\mathbf{R}}_{(h)} + \dot{\mathbf{R}}_{(h+1)}^j \right)$$

$$\mathbf{A}_{h+1}^{(j+1)} = \mathbf{A}_{eq} \left( \mathbf{R}_{(h+1)}^{(j)} \right);$$

$$\dot{\mathbf{R}}_{(h+1)}^{j+1} = \mathbf{A}_{eq(h)}^{j+1} \mathbf{R}_{(h+1)}^{j+1} + \mathbf{R}_{(h+1)}^{j+1} \mathbf{A}_{eq(h)}^{j+1 T} + \mathbf{B}_{(h+1)}$$

$$j = j + 1$$

**end**

$$h = h + 1;$$

**end**

2.2.3. *Application: Bouc-Wen systems subjected to non-stationary base random input*

The Bouc-Wen model [27-29] is a non-linear differential model, often adopted to assess the structural response of buildings to earthquakes.

The Bouc-Wen model (Figure 2.4) describes a SDoF system, having a mass  $m$ , subjected to a generic base acceleration  $a(t)$  and characterized by a hysteretic constitutive law (Figure 2.5).

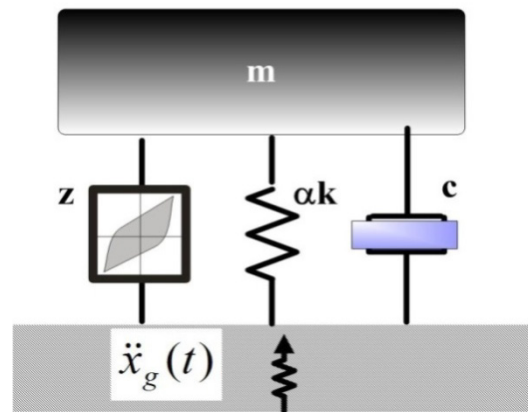


Figure 2.4- SDoF non-linear system Bouc-Wen model

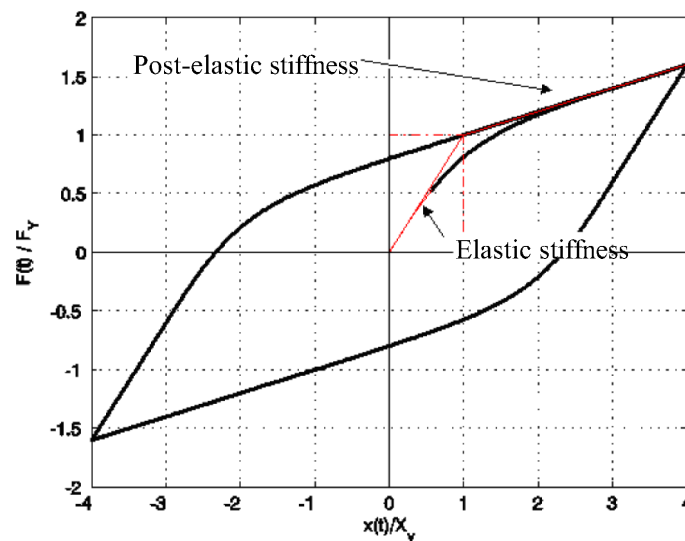


Figure 2.5 - Bouc-Wen Hysteretic force – displacement Model

The motion equation is the following:

$$m\ddot{x}(t) + F(x, \dot{x}, z, t) = ma(t) \quad (2.28)$$

In (2.28) the first term represents the inertia force whereas  $F(x, \dot{x}, z)$  is the restoring force. This term can be divided into two addends:

$$F(x, \dot{x}, z; t) = L(x, \dot{x}; t) + H(x, \dot{x}, z; t) \quad (2.29)$$

where the first one  $L(x, \dot{x}; t)$  is due to the linear viscous-elastic contribution, and the second one  $H(x, \dot{x}, z; t)$  is due to the hysteretic contribution:

$$L(x, \dot{x}; t) = c\dot{x}(t) + \alpha kx(t) \quad (2.30)$$

$$H(x, \dot{x}, z; t) = (1 - \alpha)kz(t) \quad (2.31)$$

where  $c$  is the damping and  $k$  is the initial elastic stiffness. The variable  $z(t)$  is an additional internal variable which satisfies the following non-linear equation:

$$\dot{z}(t) = G(z, \dot{x}) = \dot{x}(t) \left[ \lambda - |z(t)|^\eta (\beta + \gamma \cdot \text{sig}\{z(t)\} \cdot \text{sig}\{\dot{x}(t)\}) \right] \quad (2.32)$$

The five parameters  $\beta$ ,  $\gamma$ ,  $\eta$ ,  $\alpha$  and  $\lambda$  in (2.30-2.32) are the shape factors of the hysteretic cycle. Engineering mechanical quantities can be related to the analytical parameters previously described to model real structural elements. In order to soften laws which describe structural elements subjected to strong earthquakes, it is possible to define the initial and the post-elastic stiffness,  $k_i$  and  $k_f$ , as:

$$k_i = \left( \frac{\partial G}{\partial x} \right)_{z=0} = \alpha k + (1 - \alpha)k\lambda \quad (2.33)$$

and

$$k_f = \left( \frac{\partial G}{\partial x} \right)_{z_{\max}} = \alpha k. \quad (2.34)$$

The maximum asymptotic value of internal variable  $z$  is:

$$z_{\max} = \left( \frac{\lambda}{\beta + \gamma} \right)^{\frac{1}{\eta}} \quad (2.35)$$

The ultimate hysteretic restoring force is given by:

$$F_h^{\max} = (1 - \alpha)kz_{\max} \quad (2.36)$$

In addition it is possible to define the elastic limit displacement  $X_Y$  [12]:

$$X_Y = \frac{F_h^{\max}}{(1 - \alpha)k\lambda} = \frac{z_{\max}}{\lambda} = \lambda^{\frac{1-\eta}{\eta}} (\beta + \gamma)^{-\frac{1}{\eta}} \quad (2.37)$$

The corresponding yielding resistance is given by:

$$F_Y = k_i X_Y = (\alpha k + (1 - \alpha)k\lambda) \lambda^{\frac{1-\eta}{\eta}} (\beta + \gamma)^{-\frac{1}{\eta}} \quad (2.38)$$

From the previous equations (2.37) and (2.38), it is possible to observe that if  $\lambda = 1$ , then  $k = k_i$ ,  $\alpha$  becomes the ratio between the post-elastic and initial elastic stiffness and for  $\beta = \gamma$ :

$$X_Y = \left(\frac{1}{2\beta}\right)^{\frac{1}{\eta}} \quad (2.39)$$

and:

$$F_Y = kX_Y = k\left(\frac{1}{2\beta}\right)^{\frac{1}{\eta}} \quad (2.40)$$

so that:

$$\beta = \frac{1}{2(X_Y)^\eta} \quad (2.41)$$

It has been found [30] that the parameters of the Bouc–Wen model are functionally redundant. This redundancy is suppressed by setting  $\lambda=1$ . Moreover, if the unloading stiffness is equal to the elastic one (as happens in many cases), then  $\beta = \gamma$ . In order to describe the mechanical constitutive law, only three mechanical parameters are needed:

- initial elastic stiffness  $k_i$ ;
- post-elastic stiffness  $k_f$ ;
- maximum hysteretic restoring force  $F_Y$  (or maximum elastic displacement  $x_Y$ ).

Considering a seismic excitation where  $F(t) = -m\ddot{x}_g$ , from (2.28-2.32) the motion equations with the seismic excitation are:

$$\begin{cases} m\ddot{x}(t) + c\dot{x}(t) + \alpha kx(t) + (1 - \alpha)kz(t) = -m\ddot{x}_g(t) \\ \dot{z}(t) = \dot{x}(t)[1 - |z(t)|^\eta]\beta(1 + \text{sig}\{z(t)\}) \cdot \text{sig}\{\dot{x}(t)\} \end{cases} \quad (2.42)$$

#### 2.2.4. The Bouc-Wen model equivalent linearization

The approximate linearised form of the original non-linear equation is then achieved by

minimizing the difference between the non-linear equation and the linearised one. Then, the equation governing the internal variable  $z(t)$  is replaced with the following:

$$\dot{z}(t) = G(z, \dot{x}) = -c_{eq}(t)\dot{x}(t) - k_{eq}(t)z(t) \quad (2.43)$$

where the linearised evolutive coefficients  $c_{eq}(t)$  and  $k_{eq}(t)$  are non-linear functions of covariance response elements. Atalik and Utku [31] provided these equivalent coefficients, which appear in equations (2.9) and (2.10): for the most common case where  $\eta = 1$ ,  $\beta = \gamma$  and  $\lambda = 1$ , in the hypothesis of processes  $z$  and  $\dot{x}$  being jointly Gaussian, the time variant equivalent coefficients are:

$$c_{eq}(t) = \sqrt{\frac{2}{\pi}}\beta \left[ \sigma_z(t) + \frac{E\langle \dot{x}(t)z(t) \rangle}{\sigma_{\dot{x}}(t)} \right] - 1 \quad (2.44)$$

$$k_{eq}(t) = \sqrt{\frac{2}{\pi}}\beta \left[ \sigma_{\dot{x}}(t) + \frac{E\langle \dot{x}(t)z(t) \rangle}{\sigma_z(t)} \right] \quad (2.45)$$

where terms  $\sigma_z(t)$  and  $\sigma_{\dot{x}}(t)$  are the standard deviations of variables  $z$  and  $\dot{x}$ , respectively and  $E\langle \dot{x}(t)z(t) \rangle$  is the cross covariance of the mentioned variables.

### 2.2.5. Modelling of Input Ground Motion

It is widely known that seismic accelerograms are often modelled as zero mean stochastic non-stationary processes. Moreover, a widely used description with constant content both in amplitude and in frequency could be considered. An extensively applied stochastic approach is proposed by Clough and Penzien [32] which considers a linear fourth-order filter, obtainable from a series of two linear oscillators, forced by modulated white noise [33-35]. Ground acceleration  $\ddot{X}_g(t)$  is therefore given by:

$$\begin{cases} \ddot{X}_g(t) = -\omega_p^2 X_p(t) - 2\xi_p \omega_p \dot{X}_p(t) + \omega_f^2 X_f(t) + 2\xi_f \omega_f \dot{X}_f(t) \\ \ddot{X}_p(t) + \omega_p^2 X_p(t) + 2\xi_p \omega_p \dot{X}_p(t) = \omega_f^2 X_f(t) + 2\xi_f \omega_f \dot{X}_f(t) \\ \ddot{X}_f(t) + 2\xi_f \omega_f \dot{X}_f(t) + \omega_f^2 X_f(t) = -\varphi(t)W(t) \end{cases} \quad (2.46)$$

where  $X_f(t)$  is the response of the first filter, having frequency  $\omega_f$  and damping coefficient  $\xi_f$ ,  $X_p(t)$  is the response of the second filter characterized by frequency  $\omega_p$

and damping ratio  $\xi_p$ . Moreover,  $W(t)$  is the white noise stochastic process, the constant bilateral Power Spectral Density function of which is  $S_0$  and  $\varphi(t)$  is the modulation function. In this study the function proposed by Jennings et al. [36] is adopted.

Several expressions relate the maximum value of ground acceleration to  $S_0$ : this maximum value is called the Peak Ground Acceleration (PGA) and is indicated with  $\max\left(\left|\ddot{X}_g(t)\right|\right)$ . A commonly used conventional way is to express the PGA as:

$$PGA = 3\sigma_{\ddot{X}_g} \quad (2.47)$$

In this way, by means of some rearranging, it is possible to obtain [35]:

$$S_0 = \frac{0.222}{\pi} \frac{PGA^2 \xi_f \xi_p \left( (\omega_f^4 + 4\xi_f \xi_p \omega_f^3 \omega_p + 2(-1 + 2\xi_f^2 + 2\xi_p^2) \omega_f^2 \omega_p^2 + 4\xi_f \xi_p \omega_f \omega_p^3 + \omega_p^4) \right)}{\omega_f^2 \left( (1 + 4\xi_f^2) \xi_p \omega_f^3 + \xi_f (1 + 16\xi_f^2 \xi_p^2) \omega_f^2 \omega_p + 16\xi_f^4 \xi_p \omega_f \omega_p^2 + 4\xi_f^3 \omega_p^3 \right)} \quad (2.48)$$

### 2.2.6. Stochastic Analysis

The linearised motion equations for the system plus filter are given by:

$$\begin{cases} \ddot{X}(t) + 2\xi_s \omega_s \dot{X}(t) + \alpha \omega_s^2 X(t) + (1 - \alpha) Z(t) \omega_s^2 = \omega_p^2 X_p(t) + 2\xi_p \omega_p \dot{X}_p(t) - \omega_f^2 X_f(t) - 2\xi_f \omega_f \dot{X}_f(t) \\ \ddot{X}_p(t) + \omega_p^2 X_p(t) + 2\xi_p \omega_p \dot{X}_p(t) = \omega_f^2 X_f(t) + 2\xi_f \omega_f \dot{X}_f(t) \\ \ddot{X}_f(t) + 2\xi_f \omega_f \dot{X}_f(t) + \omega_f^2 X_f(t) = -\varphi(t) W(t) \\ \dot{Z}(t) = -c_{eq} \dot{X}(t) - k_{eq} Z(t) \end{cases} \quad (2.49)$$

Introducing the state vector  $\bar{Y}(t)$ :

$$\bar{Y}(t) = \left[ X(t) \ X_p(t) \ X_f(t) \ Z(t) \ \dot{X}(t) \ \dot{X}_p(t) \ \dot{X}_f(t) \right]^T \quad (2.50)$$

Equation (2.49) becomes:

$$\dot{\bar{Y}}(t) = \mathbf{A}_{eq}(\mathbf{R}, t) \bar{Y}(t) + \bar{F}(t) \quad (2.51)$$

where

$$\bar{F}(t) = \left[ 0 \ 0 \ 0 \ 0 \ 0 \ 0 \ -\varphi(t) W(t) \right]^T \quad (2.52)$$

is the forcing vector and

$$\mathbf{A}_{eq}(\mathbf{R}, t) = \begin{pmatrix} 0 & 0 & 0 & 0 & 1 & 0 & 0 \\ 0 & 0 & 0 & 0 & 0 & 1 & 0 \\ 0 & 0 & 0 & 0 & 0 & 0 & 1 \\ 0 & 0 & 0 & -k_{eq}(\mathbf{R}, t) & -c_{eq}(\mathbf{R}, t) & 0 & 0 \\ -\alpha\omega_s^2 & +\omega_p^2 & -\omega_f^2 & -(1-\alpha)\omega_s^2 & -2\xi_s\omega_s & +2\omega_p\xi_p & -2\omega_f\xi_f \\ 0 & -\omega_p^2 & +\omega_f^2 & 0 & 0 & -2\omega_p\xi_p & +2\omega_f\xi_f \\ 0 & 0 & -\omega_f^2 & 0 & 0 & 0 & -2\omega_f\xi_f \end{pmatrix} \quad (2.53)$$

is the equivalent system matrix.

It is possible to perform the covariance analysis starting from equation (2.51) and solving the matrix differential Lyapunov equation:

$$\dot{\mathbf{R}}(t) = \mathbf{A}_{eq}(\mathbf{R}, t)\mathbf{R}(t) + \mathbf{R}(t)\mathbf{A}_{eq}^T(\mathbf{R}, t) + \mathbf{B}(t) \quad (2.54)$$

where  $\mathbf{R}(t) = \langle \overline{YY^T} \rangle$  is the covariance matrix, while  $\mathbf{B}(t)$  is a square matrix having all zero elements except for the last one equal to  $2\pi S_0\phi(t)^2$ .

Coefficients  $k_{eq}$  and  $c_{eq}$  in matrix  $A_{eq}$  depend on the elements of  $\mathbf{R}(t)$ , and therefore an iterative procedure is required to solve equation (2.47) as for equation (2.20). This is solved by means of a Matlab Code in which the coefficients of the equivalent linear system are updated at each step and the solution of the response covariance matrix equation is searched for.

### 2.2.7. Numerical analysis

Using a Bouc-Wen model, in Figure 2.6 a non-linear single degree of freedom system is analysed under a non-stationary base acceleration, modelled using a filtered separable white noise process.

To evaluate the numerical efficiency of the proposed algorithm, the non-stationary covariance response is evaluated under different non-linear mechanical parameters and using a different time step value  $dt$ .

The modulation function used is the following [35]:

$$\varphi(t) = \alpha_{\varphi} t e^{-\beta_{\varphi} t} \quad (2.55)$$

where the maximum intensity is reached at  $T_{\max} = 10$  s,  $\varphi(T_{\max}) = 1$  (see Figure 2.6) and  $\alpha_{\varphi}$  and  $\beta_{\varphi}$  are thus defined:

$$\alpha_{\varphi} = \frac{e}{T_{\max}} \quad (2.56)$$

$$\beta_{\varphi} = \frac{1}{T_{\max}} \quad (2.57)$$

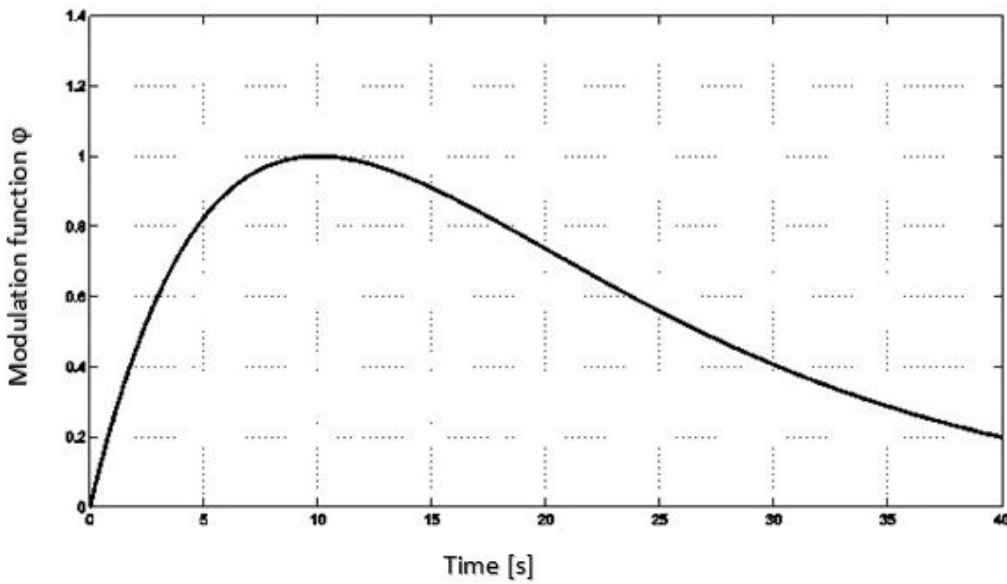


**Figure 2.6 - Modulation function**

The filtered white noise in (2.46) is modelled with the following parameters:

$$\omega_f = 20 \frac{rad}{s}, \omega_p = 5 \frac{rad}{s}, \xi_f = 0.6, \xi_p = 0.7.$$

The PGA is assumed as  $0.15g^5$ . The other main system elastic mechanical parameters are a natural period  $T_0 = 1.0s$ ,  $\omega_0 = 6.28 \frac{rad}{s}$ , a damping of  $\xi_0 = 0.05$ .

Three different values of the post-elastic/elastic ratio are used ( $\alpha=0.1, 0.5, 0.8$ ) to compare numerical performance under different levels of non-linearity. In the following Figures 2.7-2.9 the blue line refers to  $\alpha=0.1$ , the green line refers to  $\alpha=0.5$  and the red line refers to  $\alpha=0.8$ .

<sup>5</sup> The unit of measure of PGA is the gravity acceleration g.

For each of the three cases, numerical results have been evaluated under different time step values  $dt$ , in the range between 0.005s and 0.045s. Finally, as stop criterion in (2.27),  $\varepsilon_{\max} = 10^{-7}$  is assumed.

The evaluated linearised coefficients for the three analysed cases are reported in Figures 2.7 and 2.8.

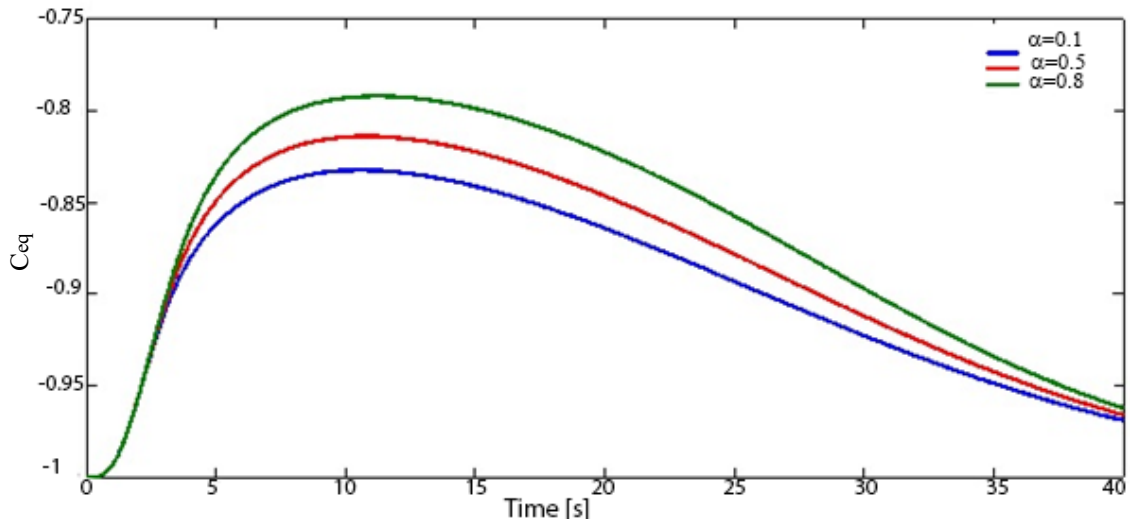


Figure 2.7 - Evolution of linearised coefficients  $C_{eq}$

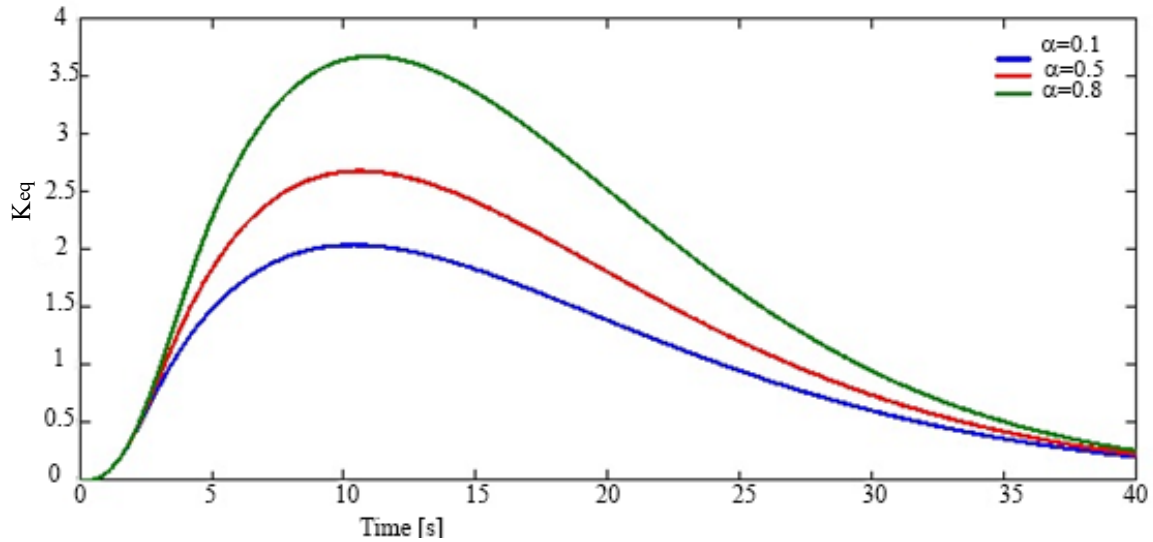


Figure 2.8 - Evolution of linearised coefficients  $K_{eq}$

The obtained results are stable both for covariance and linearised coefficients for the time steps in the range of analysis (from 0.005 to 0.045 s).

Moreover, another interesting result is the evaluation of the computational cost under different time steps. The computational cost has been evaluated as the number of iterations  $j_{tot}$  necessary to end the loop in the cycle of the predictor-corrector scheme. This value is then multiplied by the number of time steps necessary to compute the entire process in a time window  $[0, T_{tot}]$ , where  $T_{tot}=40s$ .

This is the total number of iterations required to obtain the covariance response evolution.

These results are shown in Figure 2.9, from which it is evident that, for a given accuracy, computational costs are strongly influenced by time steps. When the time-step is very small the method requires less iterations to satisfy the stop criterion, but a greater number of integration points is required. On the contrary, increasing the time step size decreases the number of integration points required, but to reach the given accuracy a greater number of iterations is required at each time step. It is important to decide the most appropriate time-step value to perform numerical integration but it depends on the problem and its parameters.

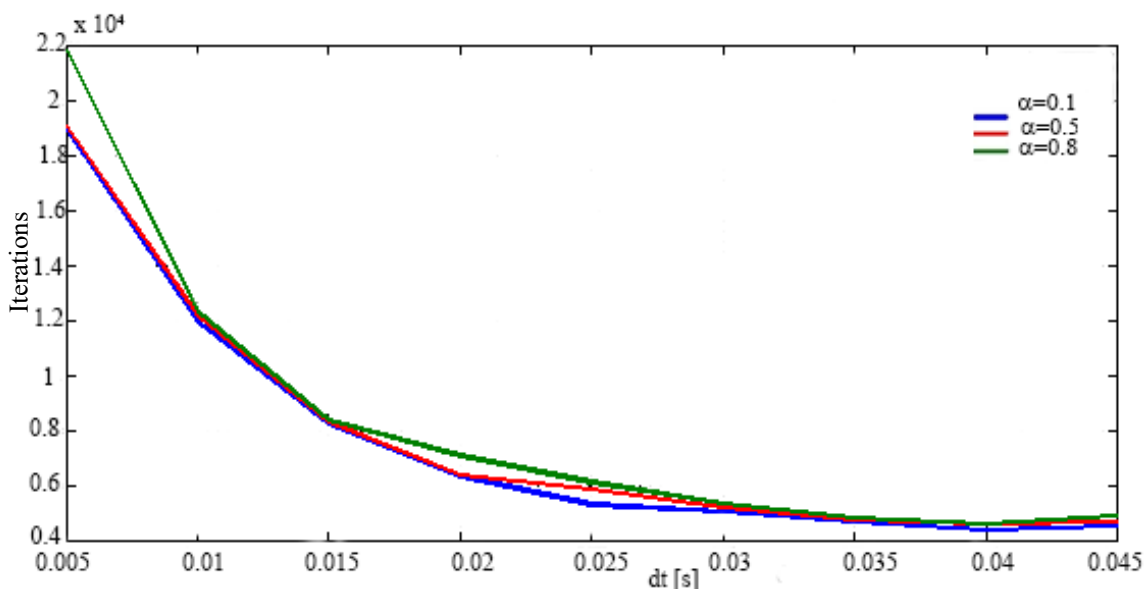


Figure 2.9 - Iterations required as a function of the time step, for different values of post-yielding stiffness.

### 2.2.8. Future Research

The most important future research will be to use a variable step size technique for the predictor-corrector scheme, such as the following:

If: 
$$e_{n+1} = \frac{\left\| \mathbf{A}_{eq} \left( \mathbf{R}^{j+1} \right) - \mathbf{A}_{eq} \left( \mathbf{R}^j \right) \right\|_F}{\left\| \mathbf{A}_{eq} \left( \mathbf{R}^j \right) \right\|_F} \quad (2.58)$$

and  $\delta > \varepsilon_{\max}$ ,  $a > 1$ ,  $b < 1$ , with  $\delta$ ,  $a$  and  $b$  chosen parameters. It is possible to define  $\Delta t$  according to the following criterion, which written in pseudo-code is:

*If*  $e_{n+1} \leq \varepsilon_{\max}$   
 $\Delta t = a \Delta t$   
*Elseif*  $e_{n+1} \geq \delta$   
 $\Delta t = b \Delta t$ .

$\Delta t$  only remains the same when the condition  $\varepsilon_{\max} < e_{n+1} < \delta$  is satisfied. Some possible values for parameters are:  $a = 1.2$ ,  $b = 0.8$ ,  $\varepsilon = 10^{-5}$ ,  $\delta = 10^{-4}$ .

In equation (2.58) it is also possible to use an infinity norm instead of a Frobenius one [38-40].

### 2.3 Boundary conditions for vibrational and piezoelectric problems

In the following two chapters of this dissertation, several problems with piezoelectric devices, subjected to natural induced vibrations, will be described. To obtain numerical well-posed problems, it is necessary to specify appropriate boundary conditions.

The problems which involve piezoelectric materials require specific boundary conditions both in the mechanical and electrical fields.

As for mechanical conditions, it is important to specify which surfaces of the objects are free to move and deform and which ones are fixed. The nature, intensity and direction of applied load (forces, pressure) must be specified. The loads could be applied on assigned surfaces or on the whole volume.

As far as electrical conditions are concerned, it is necessary to declare which surfaces of the objects have electric potential at 0V, which ones have a zero charge and if there are surfaces that behave as a terminal.

Problems which involve fluid dynamic analysis require additional boundary

conditions. When the fluid is in a container, a channel or a box, it is necessary to specify the 'walls' of the container and whether the walls are rough or smooth. Other important surfaces are the 'inlet' and the 'outlet', which are the surfaces the fluid enters through and exits from respectively. The initial fluid velocity (intensity and direction) has to be specified at the inlet and the pressure of the fluid has to be given at the outlet, or vice versa.

Initial values of all output variables of the mathematical model used to describe the phenomenon numerically (such as displacement of the object, velocity of the objects, velocity of the fluid, electric potential on each surface of the object) must be specified.

## 2.4 Conclusions

A vibrational model has been described in this chapter. A numerical approach to integrate non-stationary Lyapunov matrix equation has been presented to improve the stochastic linearization technique adopted for non-linear system representation.

The proposed algorithm is implemented using a predictor/corrector scheme, where the linearised coefficient update is performed by an iterative scheme at each step.

The numerical integration algorithm has been used for an important case of mechanical non-linearity, the hysteretic Bouc-Wen model. A single degree of freedom system modelled and subjected to non-stationary filtered white noise has been evaluated under different mechanical conditions and time step sizes.

The results show that the proposed algorithm is stable and accurate, while time step size plays a central role in total computational costs, so that an “*optimum*” time step can be found by comparing total computational costs for different steps  $\Delta t$ .

Finally, useful conditions to well define a vibrational problem are discussed at the end of the chapter.

## References

- [1] [https://www.kistler.com/fileadmin/files/divisions/sensor-technology/test-and-measurement/t-m\\_acceleration/900-380a.pdf](https://www.kistler.com/fileadmin/files/divisions/sensor-technology/test-and-measurement/t-m_acceleration/900-380a.pdf)
- [2] <http://www.idtechex.com/research/articles/piezoelectric-elastic-energy-harvesting-arrives-00008256.asp>

- [3] Acciani G., Abrescia A., Di Modugno F., Marano G.C. “Numerical algorithm for non-stationary covariance analysis of non linear mechanical system using equivalent stochastic linearization”. *Advances in Computer Science and Engineering*. Ed. Pushpa Publishing House, 2014, Vol. 13, No. 1, pp. 27 - 49.
- [4] Marano G.C., Acciani G., Abrescia A., Di Modugno F. “Equivalent Stochastic Linearization Algorithm for Non-Stationary Covariance Analysis of Mechanical Systems”. *SDS 2014 – 8th Workshop on Structural Dynamical Systems*, 2014.
- [5] Acciani G., Di Modugno F., Abrescia A., Marano G.C. “Integration algorithm for covariance nonstationary dynamic analysis using equivalent stochastic linearization”. *Mathematics and Computers in Simulation*, 2016, Vol. 125, pp. 70-82.
- [6] Nayfeh A.H., Mook D.T. “Non-linear Oscillations”. John Wiley Sons, 1995, pp. 720.
- [7] Nayfeh A.H. “Non-linear Interactions”. Wiley, 2000.
- [8] Lin Y.K. “Probabilistic Theory of Structural Dynamics”. McGraw-Hill, 1967.
- [9] Skorokhod A.V., Hoppenstead F.C., Salehi H. “Random Perturbation Methods”. Springer Verlag, 2002.
- [10] Roberts J.B., Spanos P.D. “Random vibration and statistical linearization”. John Wiley & Sons, 1990.
- [11] Roy D. “Explorations of the Phase-Space Linearization Method for Deterministic and Stochastic Non-linear Dynamical Systems”. *Non-linear Dynamics*, 2000, Vol. 23, No. 3, pp. 225-258.
- [12] Caughey T.K. "Equivalent linearization techniques". *Journal of the Acoustical Society of America*, 1963 Vol.35, No.11, pp. 1706-1711.
- [13] Crandall S.H. “A half-century of stochastic equivalent linearization”. *Structural Control and Health Monitoring*. 2006, Vol. 13, No. 1, pp. 27–40.
- [14] Cunha A.A.M.F. “The role of the stochastic equivalent linearization method in the analysis of the non-linear seismic response of building structures”. *Earthquake Engineering and Structural Dynamics*, 1984, Vol. 23, pp. 837-857.
- [15] Booton R.C. “Non-linear control systems with random inputs, Circuit Theory”. *IRE Transactions*, 1954, Vol. 1, No. 1, pp. 9-18.
- [16] Kazakov I.E. "An approximate method for the statistical investigation of non-linear systems". *Trudy VVIA im Prof. NE Zhukovskogo* 394, 1954, pp. 1-52.
- [17] Lu C.H., Evan-Iwanowski R.M. “Period doubling bifurcation problems in the softening Duffing oscillator with non-stationary excitation”. *Non-linear Dynamics*, 1994, Vol. 5, No. 4, pp 401-420.
- [18] Ates S. “Seismic behaviour of isolated multi--span continuous bridge to non-stationary random seismic excitation”. *Non-linear Dynamics*, 2012, Vol. 67, No. 1, pp 263-282.
- [19] Jia H.Y., Zhang D.Y., Zheng S.X., Xie W.C., Pandey M.D. “Local site effects on a high-pier railway bridge under tri-directional spatial excitations: Non-stationary stochastic analysis”. *Journal of Soil Dynamics and Earthquake Engineering*, 2013, Vol. 52, pp. 55.
- [20] Marano G.C. “Envelope process statistics for linear dynamic system subject to non-stationary random vibrations”. *Far East Journal of Theoretical Statistics*, 2008, pp. 29-46.
- [21] Jin X.L., Huang Z.L. “Non-stationary probability densities of strongly non-linear single-degree-of-freedom oscillators with time delay”. *Non-linear Dynamics*, 2010, Vol. 59, No. 1-2, pp. 195-206.
- [22] Qi L., Xu W., Gu X. “Non-stationary probability densities of a class of non-linear system excited by external colored noise”. *Science China Physics Mechanics and Astronomy*, 2012, Vol. 55, No. 3, pp. 477-482.
- [23] Carli F. ”Non-linear response of hysteretic oscillator under evolutionary excitation”. *Advances in Engineering Software*, 1999, Vol. 30, No. 9-11, pp. 621-630.
- [24] Lutes L.D., Sarkani S. “Random Vibrations: Analysis of Structural and Mechanical Systems”. Elsevier *Random Vibrations: Analysis of Structural and Mechanical Systems*, 2003, pp. 1-638.

- [25] Greco R., Trentadue F. "Structural Reliability Sensitivities under Non-stationary Random Vibrations". *Mathematical Problems in Engineering*, 2013 Vol. 2013, pp. 1-21.
- [26] Marano G.C., Acciani G., Cascella L.G. "Non-stationary numerical covariance analysis of linear multy degree of freedom mechanical system subject to random inputs", *Int. J. Computational Methods*, 2007, Vol. 04, No. 173.
- [27] Bouc R. "Forced vibration of mechanical systems with hysteresis". *Proc. of 4<sup>th</sup> Conf. on Non-Linear Oscillations*, Prague, Czechoslovakia, 1967, p.315-315.
- [28] Baber T.T., Wen Y. "Random vibration of hysteretic degrading system". *Journal of the Engineering Mechanics Division, Proceedings of ASCE*, 1981, Vol 107, No. 6, pp. 1069-1087.
- [29] Wen Y.K. "Method for random vibration of hysteretic systems". *Journal of the Engineering Mechanics Division ASCE*, 1976, Vol. 102, pp.150-154.
- [30] Ma F., Zhang H., Bockstedte A., Foliente G.C., Paevere P. "Parameter analysis of the differential model of hysteresis". *Journal of applied mechanics ASME*, 2004, Vol. 71, pp. 342–349.
- [31] Atalik T.S., Utku S. "Stochastic linearization of multi-degree of freedom non-linear systems". *Earthquake Engineering and Structural Dynamics*, 1976, Vol. 4, No. 4, p. 411-420.
- [32] Clough R., Penzien J. "Dynamics of structures", Mac Graw-Hill, 1975.
- [33] Fan F.G., Ahmadi G. "Non-stationary Kanai-Tajimi models for El Centro 1940 and Mexico City 1985 earthquakes", *Probabilistic Engineering Mechanics*, 1990, Vol. 5, No. 4, pp. 171-181.
- [34] Hsu T.I., Bernard M.C. "A random process for earthquake simulation". *Earthquake Engineering and Structural Dynamics*, 1978, Vol. 7, No. 4, pp.347-362.
- [35] Marano G.C., Morga M., Sgobba S. "Parameters Identification of Stochastic Non-stationary Process Used in Earthquake Modelling". *International Journal of Geosciences*, 2013, Vol. 4, No.2, pp. 290-301.
- [36] Jennings P.C., Housner G.W. "Simulated earthquake motions for design purpose". *Proc. 4th World Conference Earth. Eng.*, 1968, pp.145-160.
- [37] Marano G.C., Trentadue F., Morrone E., Amara L. "Sensitivity analysis of optimum stochastic non-stationary response spectra under uncertain soil parameters". *Soil Dynamics and Earthquake Engineering*, 2008, Vol. 28, No. 12, pp.1078-1093.
- [38] Choi C.H. "A Variable Step-Size Method for Solving Stiff Lyapunov Differential Equations". *Proc. American Control Conference*, 2001, pp. 4197-4199.
- [39] Choi C.H: "Computational Methods for Medium Scale Stiff Lyapunov Differential Equations". *Proc. Asian Control Conference*, 2009, pp. 1520-1525.
- [40] Choi C.H. "Improving the Accuracy of a Variable Step-Size Method for Solving Stiff Lyapunov Differential Equations". *Proc. of the American Control Conference*, 2003, Vol. 3, pp. 2755-2760.

### ***3. Chapter 3***

## ***Modelling, simulation and experimental validation of a cantilever beam***

Chapter 3 presents the modelling, simulation, optimization and experimental validation of the behaviour of a piezoelectric cantilever beam. The analysis has been carried out with four different case studies, describing the cantilever beam in situations with an increasing grade of difficulty. The first case study simulates a ‘hypothetical’ cantilever beam under the effect of a force which has the same intensity as that of the wind. In the second case study, the same force is applied in a simulation on a device that reproduces a real force. The simulation is validated by experimental results. The third case study also involves the validation of a simulation environment with experimental results but the wind is simulated as a flowing fluid. The last case study considers a simulated situation with a device anchored to a bluff body.

### 3.1. Introduction

The theoretical analysis of piezoelectric materials and the vibrational model in the first two chapters find several pragmatic applications in this chapter, both in the experimental and simulation fields.

Natural vibrations can become an “endless” source of inexpensive and non-polluting energy for piezoelectric transducers because of the conversion of kinetic energy into electrical energy. Moreover, piezoelectric transducers are more suitable than their electrostatic and electromagnetic counterparts to convert kinetic into electrical energy because of their higher energy density [1-2].

This chapter proposes the analysis of a piezoelectric cantilever beam subjected to natural induced vibrations. Four different case studies have been investigated. The first two cases are the basis for the others. They consider a unimorph cantilever beam stressed by a uniform pressure [3-5]. A pressure applied on the surface of the beam simulates the wind force acting on the beam. The device analysed in the first case is ideal while that in the second case is real. The third interacts with a flowing fluid in the other case studies [6-7] but in the fourth case the fluid-piezoelectric beam interaction is also influenced by the presence of a D-bluff body which holds the beam itself [7]. The modelling and simulation of the piezoelectric cantilever beam in the second and third case studies are validated by experimental results. The validated models can be used to enlarge the number and the range of case studies, thus enabling the analysis of situations that are difficult to realize experimentally. The simulated and validated models allow an appropriate choice of some parameters of the cantilever beam to be selected as the most suitable ones in order to generate more electric potential. The response of the piezoelectric beam in different situations was observed. Several piezoelectric materials, thicknesses and shapes of the piezoelectric layer are considered [3-4], [7-8].

The piezoelectric device is simulated using Comsol Multiphysics, in all the situations described. Comsol Multiphysics is a software package that implements the equations of the mathematical model using the Finite Element Method (FEM). The real devices considered in this dissertation are often in the form of a thin layer; their thickness has a micrometric scale while the other two dimensions are expressed in

millimetres, so their aspect ratio often has a magnitude order of  $10^3$ . A good mesh needs elements with an aspect ratio close to unity but, due to this very high aspect ratio, it is nearly impossible to reach this goal in simulations of thin layers. Thus, the building of a mesh for such objects is one of the most critical aspects for their simulation using the FEM. It is in fact necessary to look for a good compromise between a high number of cells and the degrees of freedom, good mesh quality and the computational time required by numerical algorithms to converge in order to find an acceptable solution.

At the end of the first two case studies, an in-depth analysis of some criteria to improve the building of the mesh to simulate a stressed piezoelectric thin layer are proposed [9]. The comparison between numerical results obtained with different kinds of mesh supports the improvements obtained with the untraditional configuration, in terms of lower number of degrees of freedom and reduced computational time.

### **3.2. Case study 1: an ideal cantilever beam under pressure**

In this first case study, the system analysed is an ideal cantilever beam (Figure 3.1) subjected to a force uniformly applied on the upper surface of the beam. This force simulates the wind action on the beam so its intensity corresponds to that of the wind force.

The system consists of two components: a thin metallic layer which supports a piezoelectric layer. The structural steel prevents rapid deterioration of the piezoelectric layer due to the applied forces.

Table I provides the geometrical characteristics of the two elements used to simulate the cantilever.

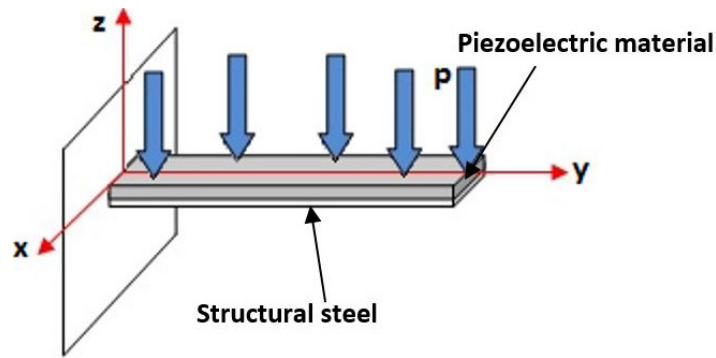


Figure 3.1 – Schematic representation of the ideal cantilever beam.

TABLE I - GEOMETRICAL CHARACTERISTICS OF STEEL AND PIEZOELECTRIC MATERIAL

	Structural steel layer	Piezoelectric layer
<b>Width [mm]</b>	9.5	9.5
<b>Length [mm]</b>	31	31
<b>Thickness [mm]</b>	0.05	0.127

A three-dimensional representation of the cantilever simulated using Comsol Multiphysics is depicted in Figure 3.2.

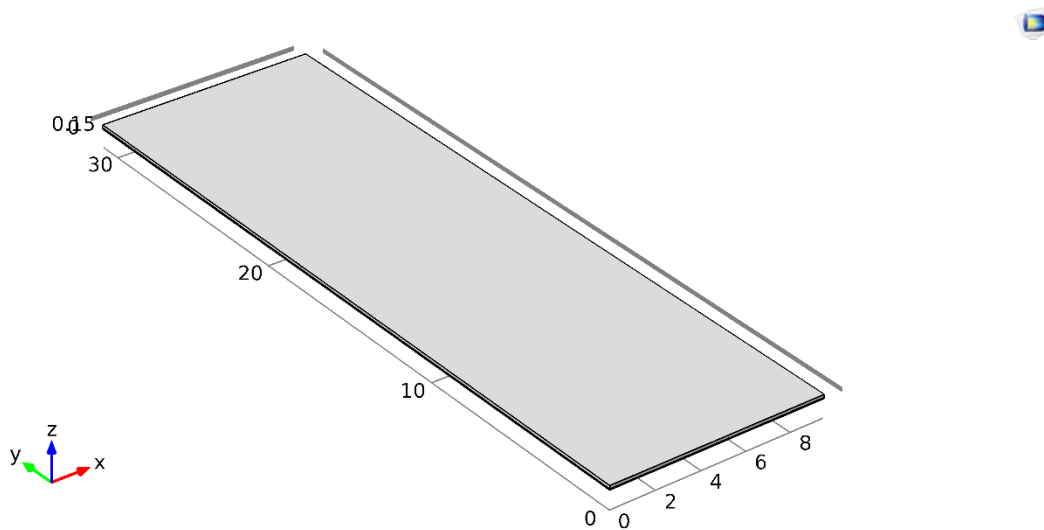


Figure 3.2 - Cantilever simulated with Comsol Multiphysics (all dimensions are expressed in millimetres).

### 3.2.1. Piezoelectric Materials

The piezoelectric materials used for simulations in this section are PZT-5H, BGO, PVDF and CdS. In order to solve the equations of the mathematical model and to properly study piezoelectric materials, Comsol Multiphysics needs all the coefficients of matrices  $c^E$ ,  $e$  and  $\epsilon^S$  as input data. Some of the materials considered are already present

in the Comsol Multiphysics library and all the coefficients of matrices  $c^E$ ,  $e$  and  $\varepsilon^S$  are known. However, this is not true for all piezoelectric materials, so the coefficients of PVDF had to be expressly calculated for this study. For this purpose, a specific algorithm had to be implemented. The relationships between the coefficients of the four sets of constitutive equations for piezoelectric materials, proposed by the IEEE Standard of Piezoelectricity [10], were applied to the coefficients known in the literature [11] and the algorithm provided the unknown coefficients. Despite the approximations due to numerical computation, the results had a low overall error.

The first material considered was PZT-5H. Its constitutive matrices extracted with the mentioned algorithm are reported in (3.1), (3.2) and (3.3), with appropriate units.

$$c^E = \begin{bmatrix} 1.272e^{11} & 8.021e^{10} & 8.467e^{10} & 0 & 0 & 0 \\ 8.021e^{10} & 9.068e^{10} & 8.467e^{10} & 0 & 0 & 0 \\ 8.467e^{10} & 8.467e^{10} & 1.174e^{11} & 0 & 0 & 0 \\ 0 & 0 & 0 & 2.298e^{10} & 0 & 0 \\ 0 & 0 & 0 & 0 & 2.298e^{10} & 0 \\ 0 & 0 & 0 & 0 & 0 & 2.347e^{10} \end{bmatrix} [\text{Pa}] \quad (3.1)$$

$$e = \begin{bmatrix} 0 & 0 & 0 & 0 & 17.034 & 0 \\ 0 & 0 & 0 & 17.034 & 0 & 0 \\ -6.622 & -6.622 & 23.240 & 0 & 0 & 0 \end{bmatrix} \left[ \frac{\text{C}}{\text{m}^2} \right] \quad (3.2)$$

$$\varepsilon^S = \begin{bmatrix} 1704.4 & 0 & 0 \\ 0 & 1704.4 & 0 \\ 0 & 0 & 1433.6 \end{bmatrix} \quad (3.3)$$

The second material considered was CdS, which belongs to the same crystal class as PZT-5H and so its matrices (3.4), (3.5) and (3.6) have the same structure and properties as those of PZT-5H.

$$c^E = \begin{bmatrix} 9.068e^{10} & 5.808e^{10} & 5.093e^{10} & 0 & 0 & 0 \\ 5.808e^{10} & 9.068e^{10} & 5.093e^{10} & 0 & 0 & 0 \\ 5.093e^{10} & 5.093e^{10} & 9.380e^{10} & 0 & 0 & 0 \\ 0 & 0 & 0 & 1.503e^{10} & 0 & 0 \\ 0 & 0 & 0 & 0 & 1.503e^{10} & 0 \\ 0 & 0 & 0 & 0 & 0 & 1.629e^{11} \end{bmatrix} [\text{Pa}] \quad (3.4)$$

$$e = \begin{bmatrix} 0 & 0 & 0 & 0 & -0.2105 & 0 \\ 0 & 0 & 0 & -0.2105 & 0 & 0 \\ -0.2192 & -0.2192 & 0.4568 & 0 & 0 & 0 \end{bmatrix} \left[ \frac{\text{C}}{\text{m}^2} \right] \quad (3.5)$$

$$\varepsilon^S = \begin{bmatrix} 9.0171 & 0 & 0 \\ 0 & 9.0171 & 0 \\ 0 & 0 & 9.5210 \end{bmatrix} \quad (3.6)$$

The third material considered was BGO. Its constitutive matrices are shown in (3.7), (3.8) and (3.9).

$$c^E = \begin{bmatrix} 1.133e^{10} & -1.82e^{10} & -1.82e^{10} & 0 & 0 & 0 \\ -1.82e^{10} & 1.133e^{10} & -1.82e^{10} & 0 & 0 & 0 \\ -1.82e^{10} & -1.82e^{10} & 1.133e^{10} & 0 & 0 & 0 \\ 0 & 0 & 0 & 4.347e^{10} & 0 & 0 \\ 0 & 0 & 0 & 0 & 4.347e^{10} & 0 \\ 0 & 0 & 0 & 0 & 0 & 4.347e^{10} \end{bmatrix} [\text{Pa}] \quad (3.7)$$

$$e = \begin{bmatrix} 0 & 0 & 0 & 0.0378261 & 0 & 0 \\ 0 & 0 & 0 & 0 & 0.0378261 & 0 \\ 0 & 0 & 0 & 0 & 0 & 0.0378261 \end{bmatrix} \left[ \frac{\text{C}}{\text{m}^2} \right] \quad (3.8)$$

$$\varepsilon^S = \begin{bmatrix} 16 & 0 & 0 \\ 0 & 16 & 0 \\ 0 & 0 & 16 \end{bmatrix} \quad (3.9)$$

The last material considered was PVDF. Its matrices are expressed in (3.10-3.12).

$$c^E = \begin{bmatrix} 3.5783e^{-9} & 1.6096e^{-9} & 1.4293e^{-9} & 0 & 0 & 0 \\ 1.6096e^{-9} & 3.1300e^{-9} & 1.3102e^{-9} & 0 & 0 & 0 \\ 1.4293e^{-9} & 1.3102e^{-9} & 1.5960e^{-9} & 0 & 0 & 0 \\ 0 & 0 & 0 & 0.5482e^{-9} & 0 & 0 \\ 0 & 0 & 0 & 0 & 0.5778e^{-9} & 0 \\ 0 & 0 & 0 & 0 & 0 & 0.69e^{-9} \end{bmatrix} [\text{Pa}] \quad (3.10)$$

$$e = \begin{bmatrix} 0 & 0 & 0 & 0 & -0.0120 & 0 \\ 0 & 0 & 0 & -0.0121 & 0 & 0 \\ 0.0389 & 0.0008 & -0.0166 & 0 & 0 & 0 \end{bmatrix} \left[ \frac{\text{C}}{\text{m}^2} \right] \quad (3.11)$$

$$\varepsilon^S = \begin{bmatrix} 7.3186 & 0 & 0 \\ 0 & 9.2352 & 0 \\ 0 & 0 & 7.8833 \end{bmatrix} \quad (3.12)$$

### 3.2.2. Boundary Conditions

Since the analysis involves piezoelectric materials, both mechanical and electrical boundary conditions have to be set. As for mechanical conditions, the device is ‘free’ to move under pressure caused by wind, except for its left surface that is locked.

The IEEE National Electrical Safety Code [12] proposes two equations useful to convert the value of the wind velocity into the value of the pressure applied on the object:

$$\text{wind pressure (psf)} = 0.00256 v^2 \text{ (mph}^2\text{)} \quad (3.13)$$

$$\text{wind pressure (Pa)} = 0.613 v^2 \text{ (m/s}^2\text{)} \quad (3.14)$$

where *wind pressure* is expressed in Pound-force per square foot in (3.13) and in Pascal in (3.14), while  $v$  is the wind velocity expressed in miles per hour in (3.13) and in metres per second in (3.14). The wind direction is normal to the surface. Using equation (3.14) it is possible to calculate that the pressure on the upper surface of the piezoelectric element of 11Pa corresponds to a wind velocity of 4.23m/s.

As for electrical boundary conditions, the upper surface of the piezoelectric layer of the cantilever is at ‘zero charge’ whereas the lower piezoelectric surface and the vertical surfaces are at ‘zero voltage’, i.e. ‘ground’. In Figure 3.3 the edges at ground are highlighted.

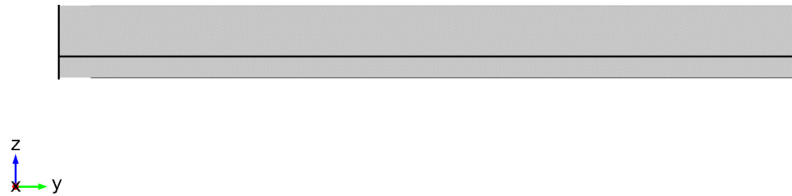


**Figure 3.3 - Electrical conditions.**

### 3.2.3. The mesh

The mesh created for the cantilever used in this case study was built automatically by Comsol Multiphysics as a 'finer' mesh with free tetrahedra. It consisted of 242,976 domain elements, 118,942 boundary elements, and 1,980 edge elements. The number of DoF to solve was 1,685,281. A detail of the mesh is depicted in Figure 3.4

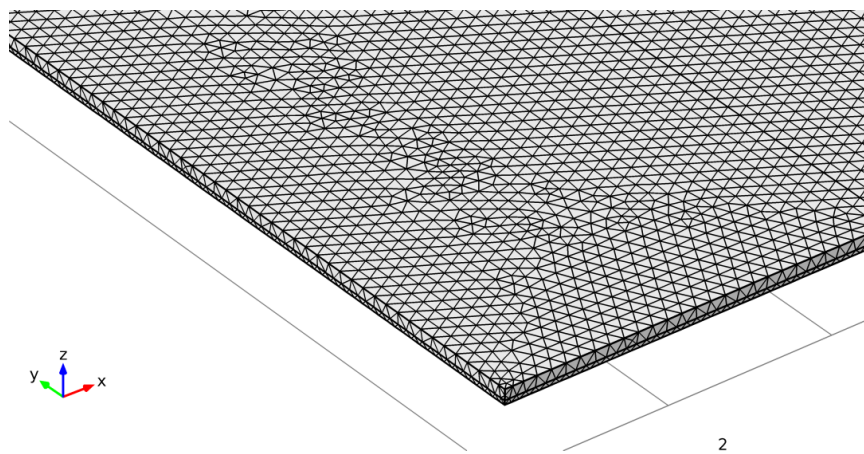


**Figure 3.4 - The mesh created for the simulation of the cantilever beam. (All dimensions are expressed in millimetres).**

### 3.2.4. Simulation results

The following simulations were performed with a three-dimensional approach in steady state and so with a stationary analysis. The cantilever had the same shape, dimensions, boundary conditions and applied pressure in all simulations but it was made of a different piezoelectric material in each case study. The electric potential generated by the cantilever beam under applied pressure is shown in a three-dimensional plot for the different case studies. In order to evaluate the potential, a so-called 'cut line' was considered on the upper surface of the piezoelectric material: it has the same direction as the y-axis, starts from the middle point of the bound extreme and stops at the middle point of the free opposite end, as shown in Figure 3.5.

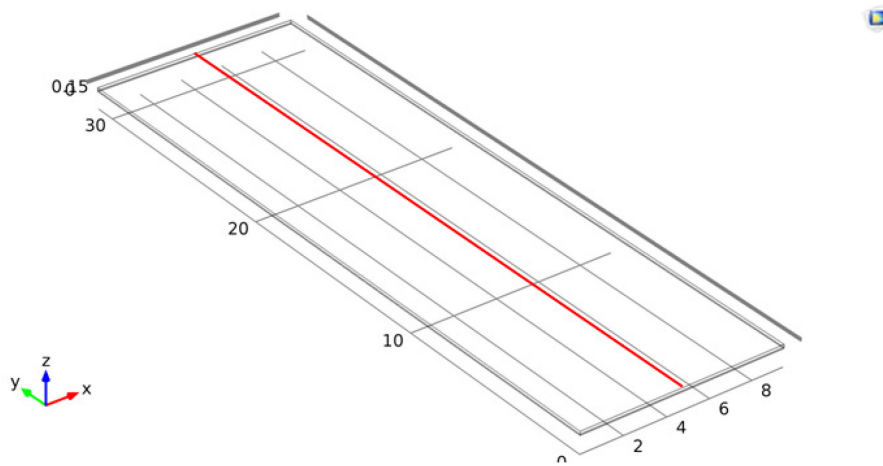


*Figure 3.5 - Cut line on the upper piezoelectric surface, used to evaluate the generated electric potential. (all dimensions are expressed in millimetres).*

#### 3.2.4.1. Lead Zirconate Titanate

The first material considered was PZT-5H. The displacement caused by the pressure applied on the beam is shown in Figure 3.6.

The beam has a maximum displacement of  $2 \cdot 10^{-2}$  mm from its initial position, located at its free end.

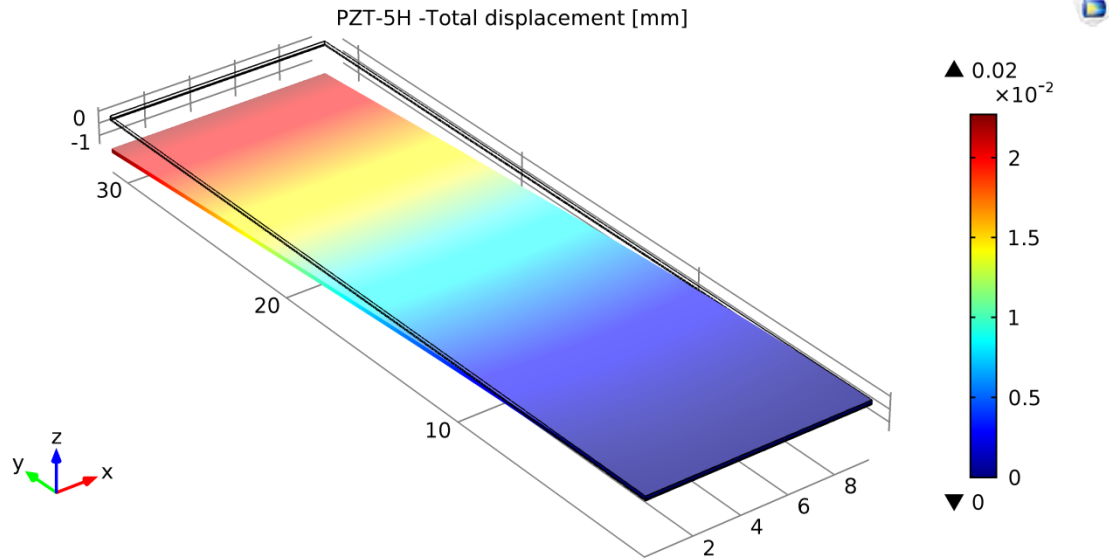


**Figure 3.6 - Total displacement of the cantilever beam made of PZT-5H and steel. (All dimensions are expressed in millimetres)**

A deformation generates an electric potential and Figure 3.7 shows a three-dimensional image of the electric potential generated under wind pressure. The different values of electric potential along the upper surface of the beam are shown according to the colour bar on the right.

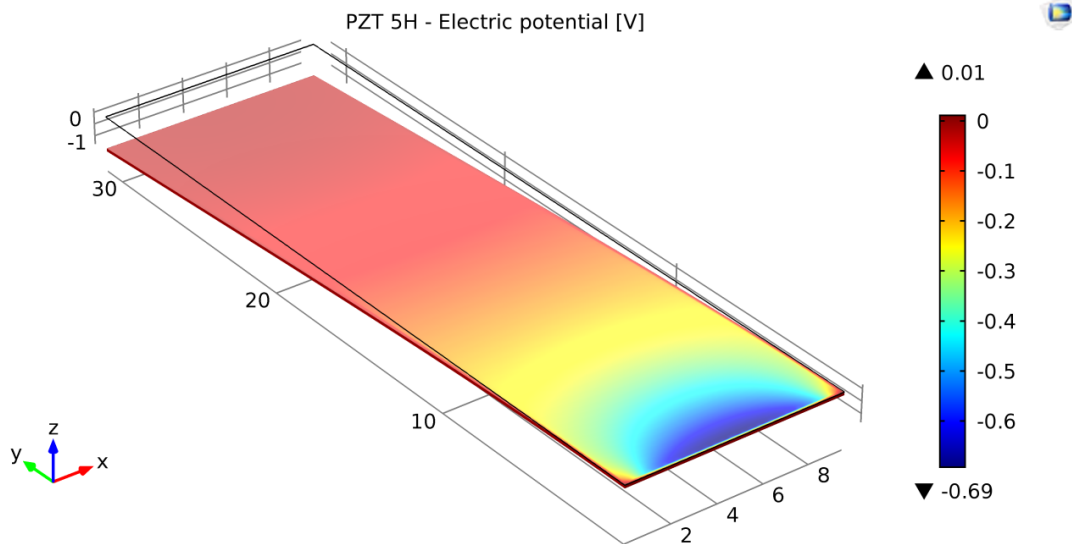


**Figure 3.7 - Electric potential generated by the cantilever beam made of PZT-5H and steel. (All dimensions are expressed in millimetres).**

It was possible to observe uniform values of the potential along the cross sections and a higher intensity near the bound edge. The maximum absolute value of electric potential generated was 0.69V and was located on the locked part of the cantilever while the

value of electric potential at the free edge of the beam was 0.01V, shown in red in Figure 3.7.

### 3.2.4.2. Cadmium Sulfide

The second material simulated was CdS. The displacement caused by the pressure applied on the beam and the electric potential generated are shown in Figure 3.8 and Figure 3.9, respectively.

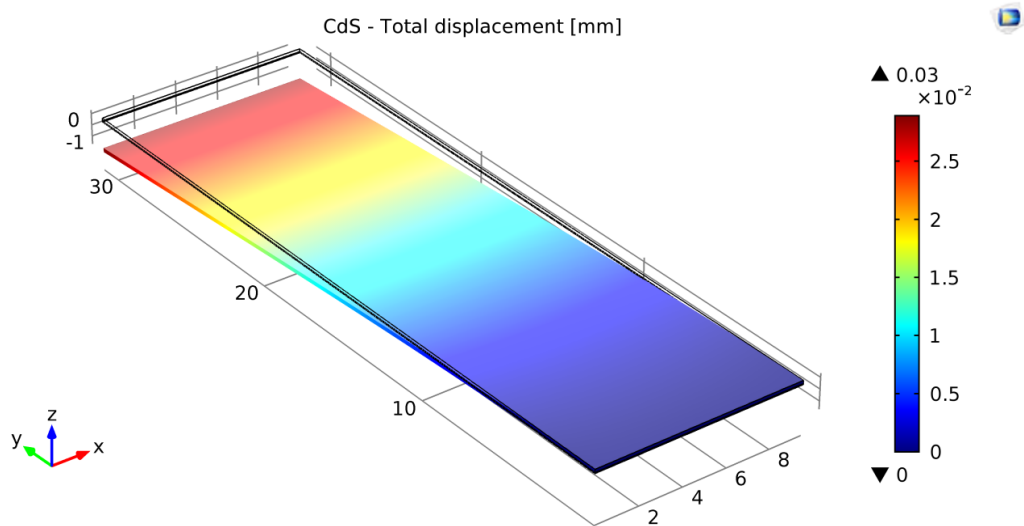


**Figure 3.8 - Total displacement of the cantilever beam made of CdS and steel (All dimensions are expressed in millimetres).**

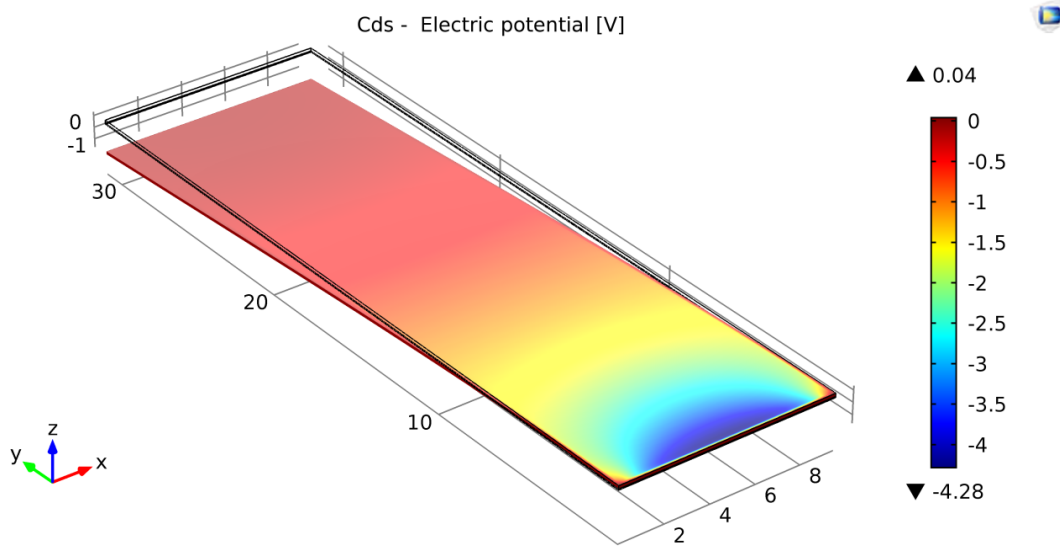


**Figure 3.9 - Electric potential generated by the cantilever beam made of CdS and steel (all dimensions are expressed in millimetres).**

The beam has a maximum displacement of  $3 \times 10^{-2}$  mm from its initial position as Figure 3.8 shows. Figure 3.9 shows that the maximum absolute value of voltage generated was

4.28V and it was again located near the locked end of the beam.

### 3.2.4.3. Bismuth Germanate

The third material considered was BGO. The displacement caused by the pressure applied on the beam is shown in Figure 3.10.

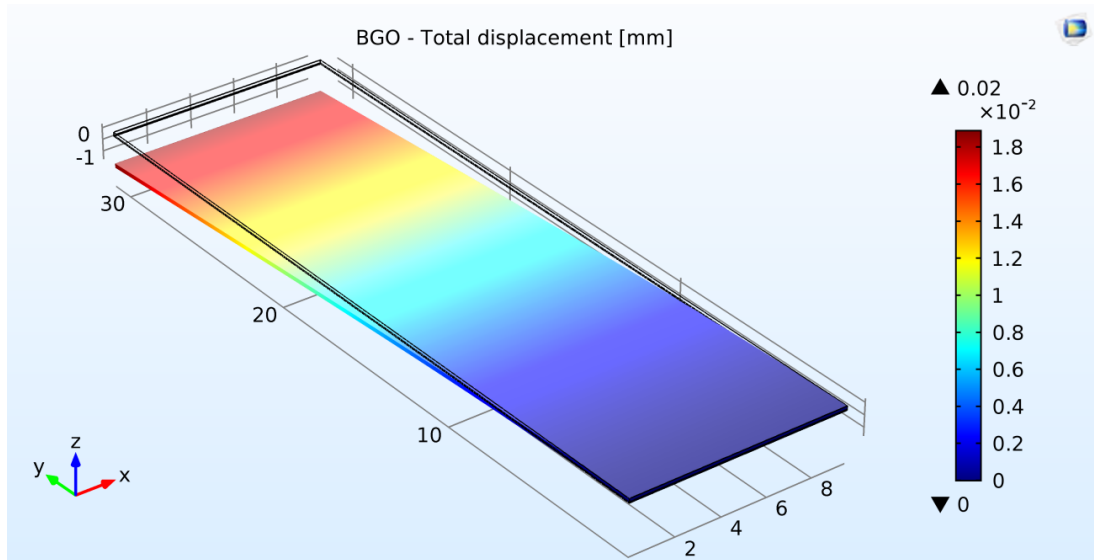


**Figure 3.10 - Total displacement of a cantilever made of BGO and steel (all dimensions are expressed in millimetres).**

The beam has a maximum displacement of  $2 \times 10^{-2}$  mm from its initial position (Figure 3.10), the same obtained with PZT-5H but the electric potential generated (Figure 3.11) was only 0.05V, which is very low compared with those generated by PZT-5H and CdS.

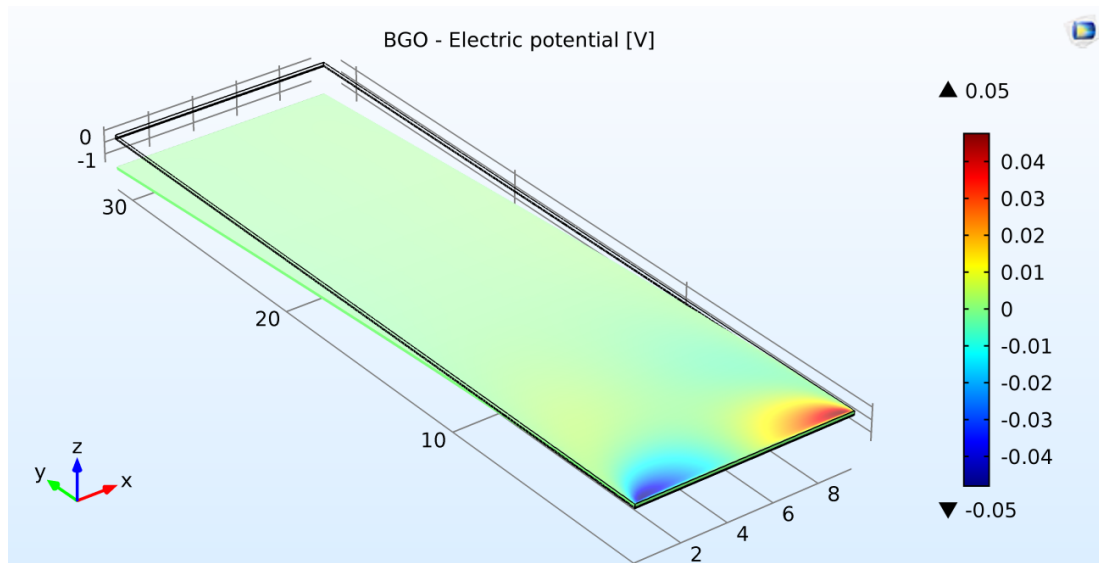


**Figure 3.11 - Electric potential generated by a cantilever made of BGO and steel (all dimensions are expressed in millimetres).**

### 3.2.4.4. Polyvinylidene Fluoride

The last material tested was PVDF. The displacement caused by the pressure applied on the beam is shown in Figure 3.12.

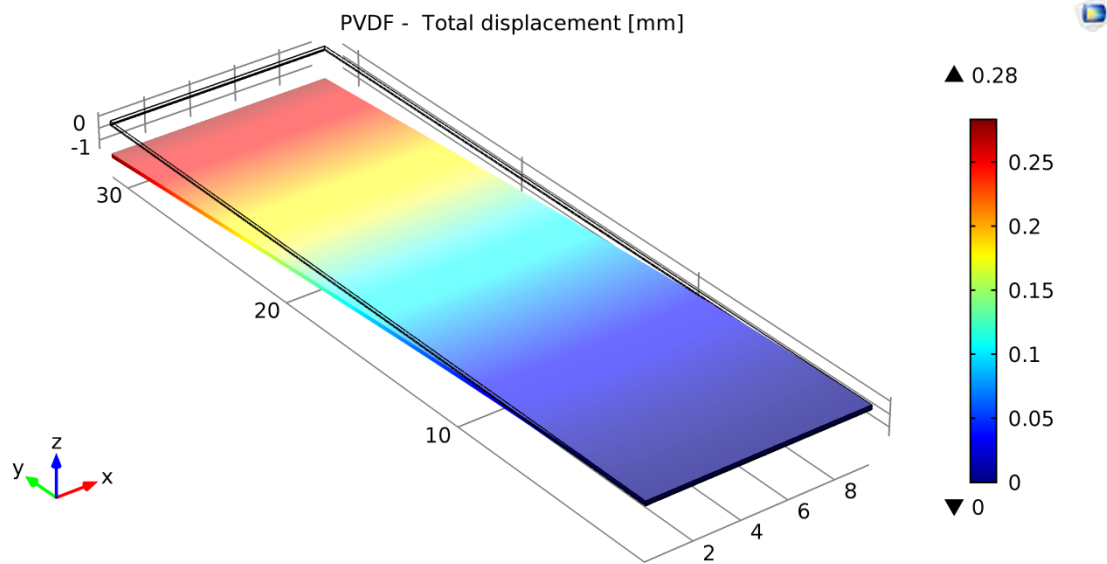


*Figure 3.12 - Total displacement of a cantilever made of PVDF and steel (all dimensions are expressed in millimetres).*

The beam has a maximum displacement of 0.28mm from its initial position (Figure 3.12), the highest of the four materials: this result is due to the high flexibility of PVDF. While the maximum value for electric potential was 2.73V.

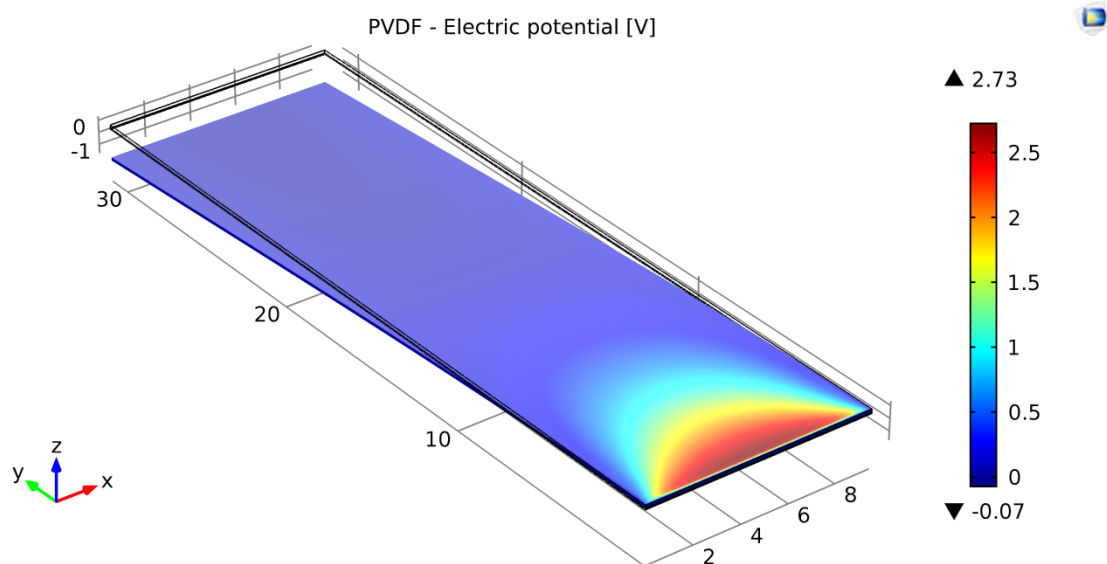


*Figure 3.13 - Electric potential generated by a cantilever made of PVDF and steel (all dimensions are expressed in millimetres).*

The sign of maximum electric potential generated depends on the sign of the coefficient  $d_{31}$  in equations (1.4) and (1.5). The sign of lengthened fibre is in agreement with that of  $d_{31}$ , while the sign related to the potential generated by compressed fibre is discordant. This effect can be exploited to design a suitable harvester circuit to store charge using a boost converter. Table II summarizes the results obtained.

TABLE II - RELATIONSHIP OF  $D_{31}$  COEFFICIENT WITH VOLTAGE GENERATED BY DIFFERENT MATERIALS

	Max value of potential [V]	Min value of potential [V]	$d_{31}$ [C/N]
<b>BGO</b>	0.05	-0.05	0
<b>PZT-5H</b>	0.01	-0.69	5.93E-10
<b>CdS</b>	0.04	-4.28	1.03E-11
<b>PVDF</b>	2.73	-0.07	-3.277E-11

The graph in Figure 3.14 shows a comparison of the maximum absolute values of electric potential generated by the different materials, at constant applied pressure, on a fixed configuration of the cantilever beam. The graph shows that the highest, and thus the best, electric potential is generated by CdS. It reaches a maximum value of 4.28V compared to 2.73V, 0.69V and 0.05V generated by PVDF, PZT-5H and BGO, respectively.

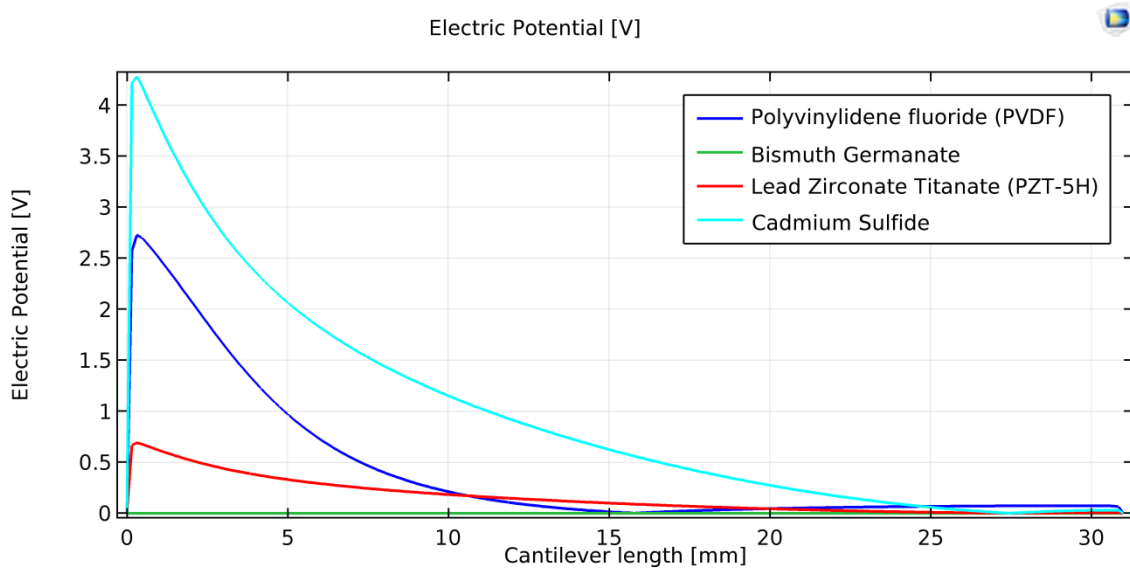


Figure 3.14 - Comparison of electric potential generated by different materials.

The maximum absolute value of the electric potential obtained in simulations on the upper surface of the piezoelectric device is shown in Table III. The root mean square (RMS) value, the corresponding values of energy and surface charge density generated are also shown for each material tested.

TABLE III - COMPARISON OF ELECTRICAL QUANTITIES GENERATED BY DIFFERENT MATERIALS

	Max absolute value of potential [V]	RMS value of potential [V]	Energy [J]	Surface charge density [C/m <sup>2</sup> ]
<b>BGO</b>	0.05	2.7588E-9	3.45E-15	1.4E-7
<b>PZT-5H</b>	0.69	0.14170	1.18E-9	9.78E-5
<b>CdS</b>	4.28	0.88753	2.58E-10	3.48E-6
<b>PVDF</b>	2.73	0.27380	3.99E-11	3.14E-7

The performance evaluation highlights the need to design and produce piezoelectric devices specific to their final use (section 1.4). In particular, it is better to employ materials that generate a higher electric potential difference at the output port for actuators, and it is preferable to employ materials that generate a greater surface charge density for harvester devices. Table III shows a very high value of  $9.78 \cdot 10^{-5} \text{C/m}^2$  for the surface charge density of PZT-5H, which makes it the most suitable material for energy harvesting among the four examined. This confirms what is already known in the literature and in industrial production: PZT-5H is currently one of the most studied and exploited materials for Energy Harvesting.

### 3.2.5. Simulations with different thickness

Once PZT-5H had been identified as the most suitable material for the piezoelectric device under study, an optimisation of the thickness of the piezoelectric layer was carried out.

#### 3.2.5.1. Increasing Thickness

The initial thickness of the PZT layer was 0.127mm. New simulations were performed increasing the thickness with a regular step of 0.1143mm up to a value of 1.27mm. Figure 3.15 shows the electric potential generated along the cut line (see Figure 3.5) for layers with increasing thickness.

It is possible to observe that the best result was that produced by the layer with an initial thickness of 0.127mm. The other values of electric potential generated are inversely proportional to the thickness of the piezoelectric layer. This is due to the weight of the piezoelectric device: if it is lighter, it is also more flexible. This in turn means that it undergoes greater deformation and therefore produces a higher voltage.

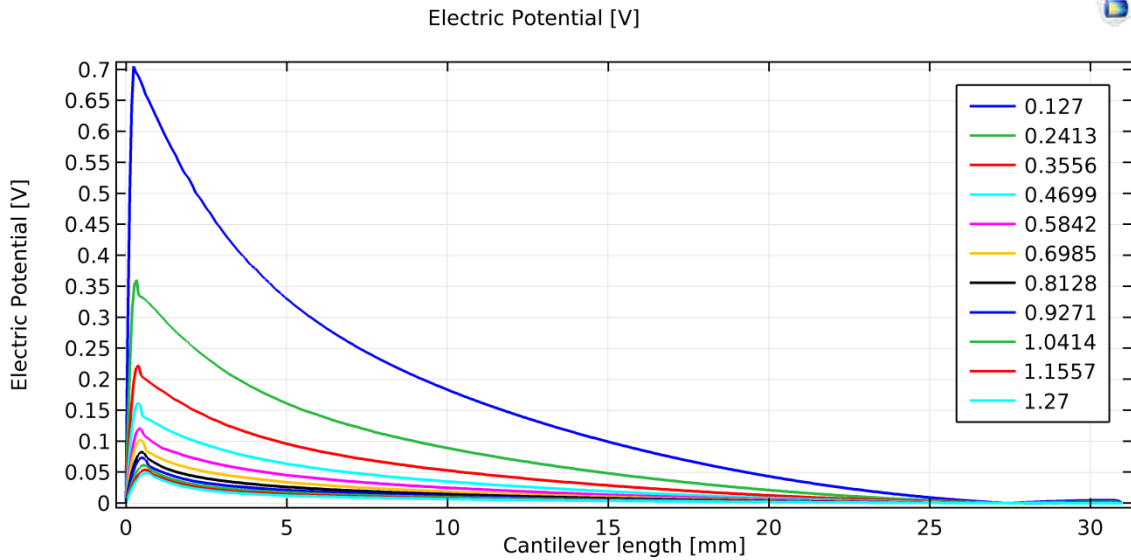


**Figure 3.15 - Comparison of the electric potential generated by PZT layers with increasing thickness.**

### 3.2.5.2. Decreasing Thickness

The previous analysis suggests that a thinner device could imply a higher output voltage. Thus, the same analysis was repeated decreasing the thickness of the piezoelectric layer with a regular step of  $1.45 \cdot 10^{-2}$  mm, down to a thickness of  $2.54 \cdot 10^{-2}$  mm. Thinner devices become very fragile so they were not simulated. Figure 3.16. shows the electric potential generated along the cut line (see Figure 3.5) for layers with increasing thickness.

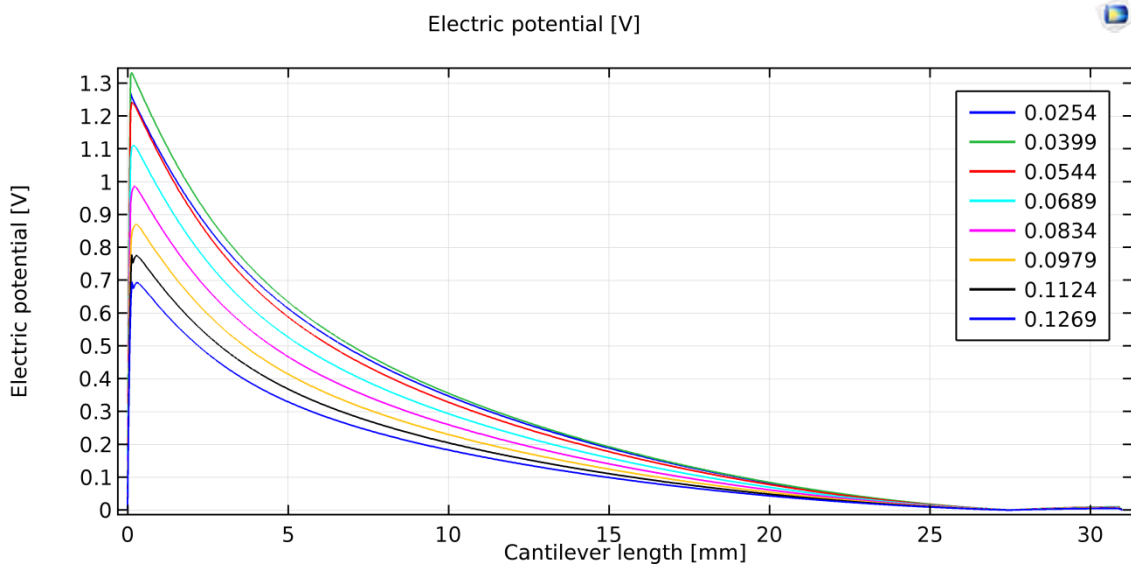


**Figure 3.16 - Comparison of the electric potential generated by different thickness.**

Table IV shows the numerical results provided by the simulations carried out for the 18 thicknesses. The energy and the electric potential were measured on the upper surface of the piezoelectric layer, while the displacement was measured on the upper boundary of the free end of the beam. The blue row in bold indicates the results obtained for the initial thickness of piezoelectric layer studied, while the pink row in italics provides the best value of energy generated. The analysis of the graph in Figure 3.16 confirmed that thinner piezoelectric layers generate higher electric potentials.

The best response of 1.43V was given by the cantilever with one of the lowest thicknesses of 39.9 $\mu$ m but the best value of energy 1.57\*10<sup>-9</sup>J was provided by the cantilever with the minimum thickness (25.4 $\mu$ m), as shown in Table IV.

The last column of Table IV shows the values of the ratio between energy produced and volume of piezoelectric layer. The highest value was 1.57\*10<sup>-9</sup>J/mm<sup>3</sup> and confirms that the best result is provided by the cantilever with the minimum thickness.

TABLE IV - SIMULATION RESULTS FOR 18 THICKNESSES OF THE PZT-5H LAYER

Thickness [mm]	Energy [J]	Max Absolute value of electric potential [V]	Max displacement [mm]	Volume [mm <sup>3</sup> ]	Ratio [J/mm <sup>3</sup> ]
<i>0.0254</i>	<i>1.17E-08</i>	<i>1.388400896</i>	<i>0.269182572</i>	<i>7.4803</i>	<i>1.57E-09</i>
0.0399	8.49E-09	1.430409258	0.168424526	11.75055	7.22E-10
0.0544	5.76E-09	1.299103007	0.109533576	16.0208	3.60E-10
0.0689	3.95E-09	1.129722159	0.074494436	20.29105	1.95E-10
0.0834	2.79E-09	0.986729221	0.052796189	24.5613	1.14E-10
0.0979	2.04E-09	0.873478626	0.038770862	28.83155	7.06E-11
0.1124	1.53E-09	0.778424667	0.029333382	33.1018	4.63E-11
0.1269	1.18E-09	0.698339425	0.022757256	37.37205	3.17E-11
<b>0.127</b>	<b>1.17E-09</b>	<b>0.764896599</b>	<b>0.022703997</b>	<b>37.4015</b>	<b>3.14E-11</b>
0.2413	2.79E-10	0.375048487	0.005320999	71.06285	3.92E-12
0.3556	1.13E-10	0.229271601	0.002070982	104.7242	1.08E-12
0.4699	5.82E-11	0.167543128	0.00102558	138.38555	4.21E-13
0.5842	3.41E-11	0.128519456	5.85E-04	172.0469	1.98E-13
0.6985	2.17E-11	0.102685524	3.67E-04	205.70825	1.05E-13
0.8128	1.46E-11	0.087813698	2.45E-04	239.3696	6.11E-14
0.9271	1.03E-11	0.076504179	1.73E-04	273.03095	3.78E-14
1.0414	7.52E-12	0.066458762	1.26E-04	306.6923	2.45E-14
1.1557	5.66E-12	0.059491828	9.52E-05	340.35365	1.66E-14
1.27	4.34E-12	0.052308401	7.37E-05	374.015	1.16E-14

Figure 3.17 shows the maximum absolute value of the electric potential generated by cantilevers with different thicknesses.

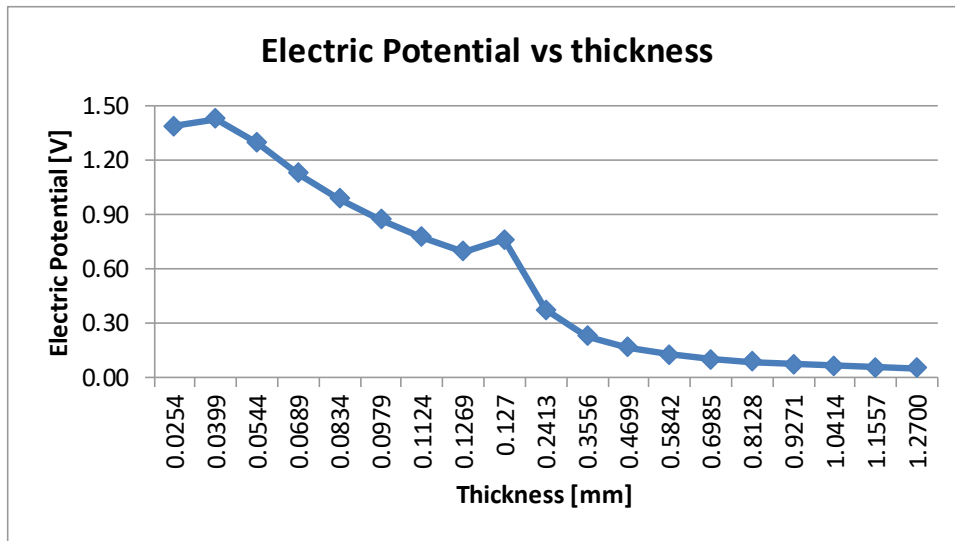


Figure 3.17 - Comparison of the maximum value of electric potential generated by different thickness.

Figures 3.18, 3.19 and 3.20 show the energy generated by cantilevers with different thicknesses, the maximum displacement of the free end of the devices and the ratio between the energy generated and the volume of the transducers, respectively. Despite the diagram in Figure 3.17, the trend of the considered quantities, calculated for increasing thicknesses, can be approximated with a polynomial function, as shown in the diagrams in these last three figures. The light black line shows the polynomial approximation.

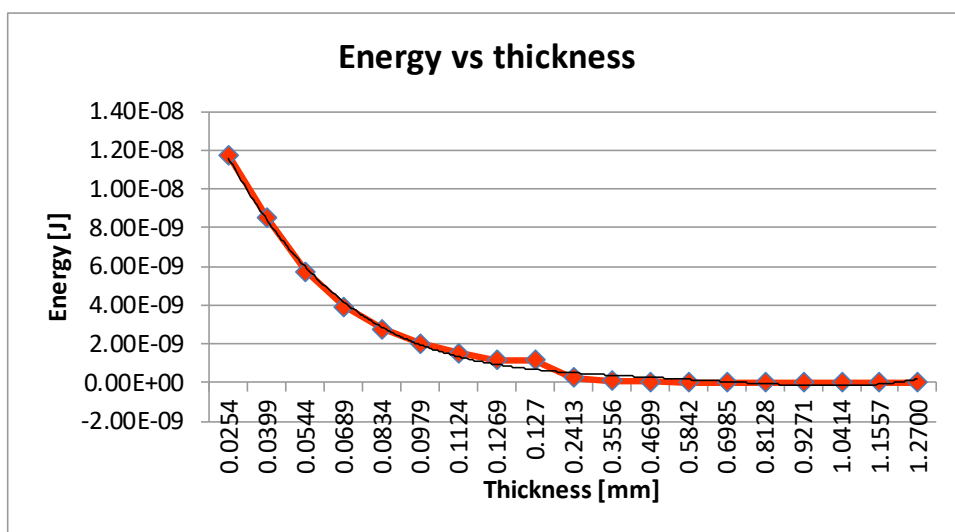


Figure 3.18 - Comparison of the energy generated by different thickness.

In Figure 3.18 the polynomial function which better approximates the trend of the energy generated by the cantilevers can be expressed with the following fourth degree polynomial function:

$$y = 5 \cdot 10^{-13}x^4 - 3 \cdot 10^{-11}x^3 + 5 \cdot 10^{-10}x^2 - 5 \cdot 10^{-9}x + 2 \cdot 10^{-8}.$$

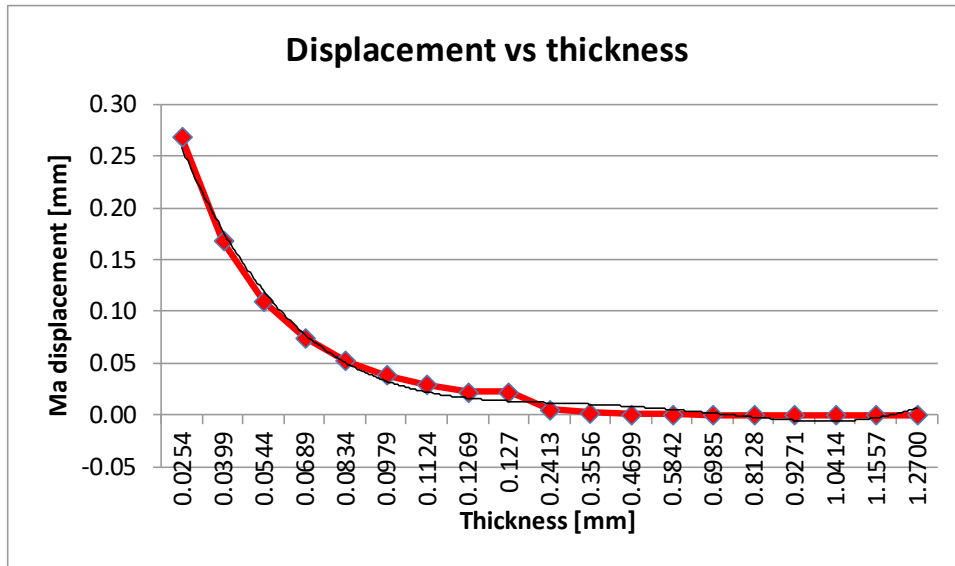


Figure 3.19 - Comparison of the displacement obtained by different thickness.

In Figure 3.19 the polynomial function which better approximates the trend of the maximum displacement reached by the free end of the cantilevers can be expressed with the following fourth degree polynomial function:

$$y = 2 \cdot 10^{-5}x^4 - 9 \cdot 10^{-4}x^3 + 1.5 \cdot 10^{-2}x^2 - 1.2 \cdot 10^{-1}x + 0.3.$$

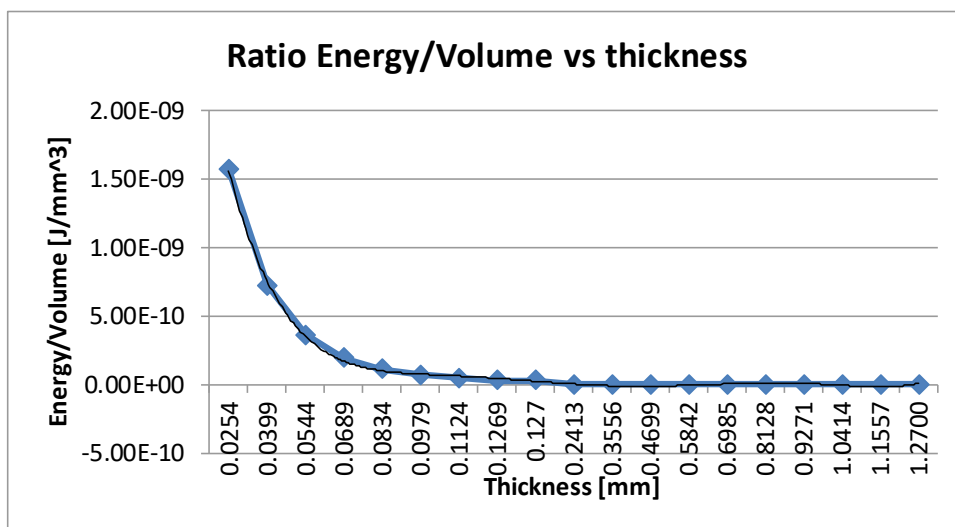


Figure 3.20 - Comparison of the ratio energy/volume obtained by different thickness.

In Figure 3.20 the polynomial function which better approximates the trend of the ratio between the energy generated and the volume of the transducers can be expressed with the following sixth degree polynomial function:

$$y = 2 \cdot 10^{-15}x^6 - 2 \cdot 10^{-13}x^5 + 5 \cdot 10^{-12}x^4 - 6 \cdot 10^{-11}x^3 + 5 \cdot 10^{-10}x^2 - 2 \cdot 10^{-9}x + 3 \cdot 10^{-9}.$$

### 3.3. Case study 2: a real cantilever beam under pressure

The aim of this case study was to validate the modelling and simulation of a wind-stressed piezoelectric cantilever beam, through a comparison between experimental and simulated data. Experimental data were measured on a PVDF cantilever beam with silver elements and subjected to wind force; the latter data were obtained from a software simulation of the same device.

Firstly, the experimental apparatus is presented. Then the approach used to validate the simulation environment is described: the equations of the mathematical model, the software used to simulate the behaviour of the cantilever beam under wind effect and all elements useful for the simulation, such as boundary conditions. The numerical results are presented. Then there is a comparison between the results produced with different materials, belonging to natural crystals, piezo ceramics and piezo polymers, in order to choose the optimal piezoelectric material for this kind of cantilever. This last study was carried out by characterizing the constitutive matrices for the piezoelectric material under test and implementing the equations of the mathematical model for each different material.

#### 3.3.1. *Experimental apparatus*

The simulated object is a real device, also used in the next case study. It is a Meas LDT1-028k cantilever beam. It is a unimorph piezoelectric device, consisting of one layer of PVDF sandwiched between two layers of silver ink. The screen-printed electrodes were coated with a thin protective layer over the active electrode area to prevent oxidation of the top surface of the silver ink. The thickness of the protective coating can be ignored for the purposes of this case study. The structure of the transducer is depicted in Figure 3.21.

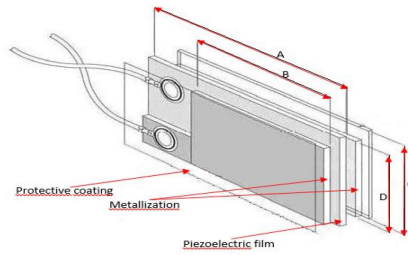


**Figure 3.21 -Structure of the Meas LDT1-028k cantilever beam**

Its dimensions are reported in Table V and were provided by its manufacturer [13].

**TABLE V - DIMENSIONS AND PROPERTIES OF THE CANTILEVER BEAM**

	<b>Parameter</b>	<b>Value</b>	<b>Unit</b>
<b>Metallic beam</b>	Short length B	30	mm
	Width	12	mm
	Thickness	6+6	µm
<b>PVDF</b>	Length A	41	mm
	Width	12	mm
	Thickness	28	µm
	Piezo Strain Constant $d_{31}$	$23 * 10^{-12}$	C/N
	Piezo Strain Constant $d_{33}$	$-33 * 10^{-12}$	C/N
	Piezo Strain Constant $g_{31}$	$216 * 10^{-3}$	Vm/N
	Piezo Strain Constant $g_{33}$	$-330 * 10^{-3}$	Vm/N
	Electromechanical coupling factor $k_{31}$	0.12	
<b>Plastic coating</b>	Thickness	Negligible	

Figure 3.22 shows a photograph of the transducer under study, in which the huge difference between its dimensions can be noticed.

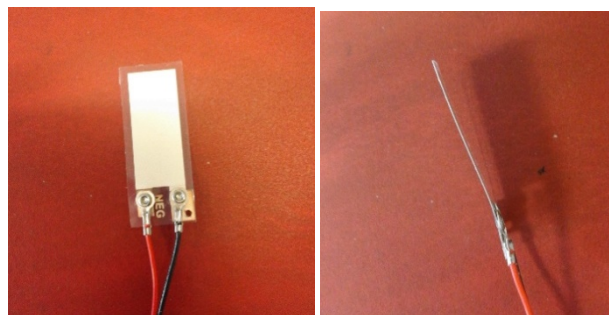


**Figure 3.22 – Photograph of the Meas LDT1-028k transducer under study made of PVDF and silver**

The experimental apparatus also consisted of an ultrasound-based digital anemometer, an oscilloscope and a pc (Figure 3.23). A C# .NET application was specially written to control and read all the devices. It provides velocity and direction of

the wind on the cantilever and, at the same time, it provides the root mean square (RMS) value, the minimum and the maximum value of voltage detected by a digital oscilloscope connected to the cantilever output.

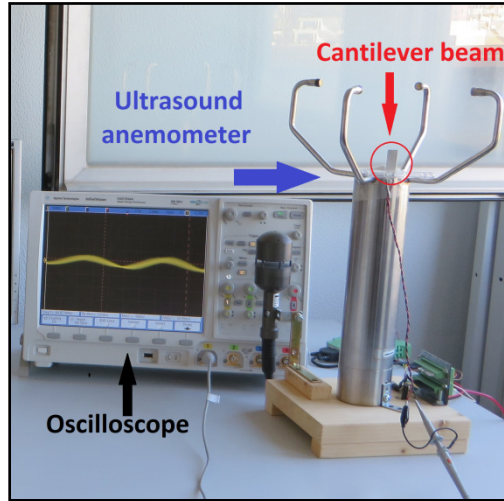


*Figure 3.23 - Experimental setup. The Meas LDT1-028k transducer under study is circled in red.*

The ultrasonic anemometer 2D (a Thies Clima model US2D, seen from above in Figure 3.24) is designed to capture the horizontal components of wind speed and the wind direction. It can also be safely operated in case of unfavourable environmental conditions (rain, snow, etc.).

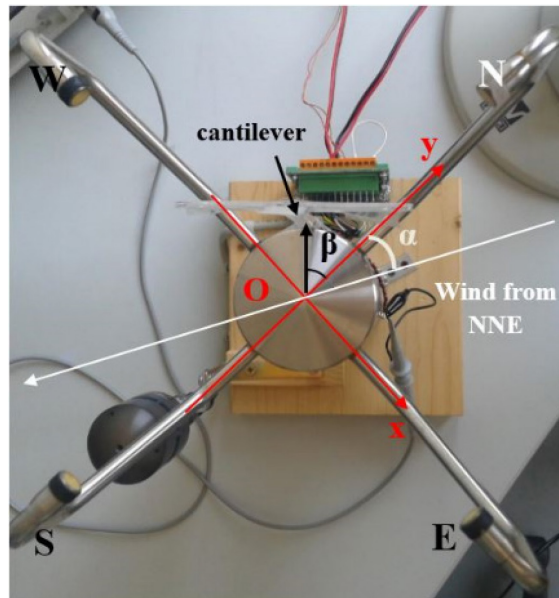


*Figure 3.24 - Cantilever beam on an anemometer. White arrow shows wind direction.*

The ultrasonic anemometer consists of four ultrasonic transformers, arranged in pairs of opposite arms placed at a distance of 200mm. Each transformer acts both as a transmitter and as a receiver. The two measurement paths are perpendicular to each other. An electronic control system selects the measurement paths and their directions. A sequence of four measurements was performed at the maximum speed allowed by the setup: the first one along the direction from south to north, then from west to east, from north to south and finally from east to west. The average values were derived from the four individual measurements in the appropriate directions and then used for further calculations. The duration of a measurement sequence was approximately 2.5ms. Measurements of wind velocity consider the speed of sound. In a stationary environment, it is influenced by the component of the velocity vector with respect to the direction of the wind. If these components agree with the propagation direction of the sound, the result is an increase in sound speed; on the contrary, the result is a reduction in the speed of propagation. The propagation times of sound and wind are closely related to the speed of propagation. As well as the speed of sound depending on the air temperature, the propagation time of sound depends on both measurement paths in both directions (Figure 3.24). Combining the two measurement paths, the results of the measurement and the angle  $\alpha$  of the speed vector of the wind are obtained. Subsequently, by transformation into polar coordinates, one of the two measurement paths detects the angle  $\alpha$  and the other one detects the sum of wind speeds. In Figure 3.24, angle  $\beta=45^\circ$  indicates the position of the cantilever relative to north.

### 3.3.2. Mathematical model

The *mechanical equilibrium equations* are useful to describe the behaviour of a cantilever beam that experiences a deformation because of wind pressure and generates electric potential.

$$-\nabla \cdot T = F_V, \quad (3.15)$$

$$T \cdot n = F_A, \quad (3.16)$$

$$F_A = -pn \quad (3.17)$$

In Equations (3.15-3.17),  $T$  is the stress,  $F_V$  is the volume force,  $F_A$  is the surface force,  $p$  is the pressure,  $n$  is the normal vector to the surface where pressure is applied. The

direct piezoelectric effect, due to the PVDF layer, is mathematically described using the constitutive equations of piezoelectric materials expressed in the stress-charge form (1.3).

Equation (3.14) was used to convert measured values of wind speed into values of wind pressure useful for the simulation.

### 3.3.3. Simulations

All the situations analysed with the experimental apparatus were simulated using the previous Equations (3.15-3.17) and (1.3). The cantilever used was built with the same shape, dimensions and materials as those used in the experimental apparatus. Figure 3.25 shows the geometry of the cantilever beam in its initial status, without any pressure applied.

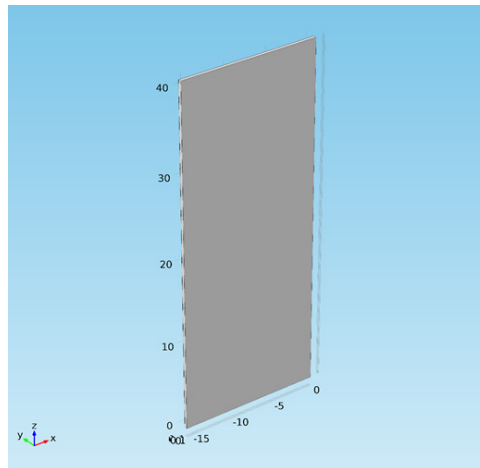


*Figure 3.25 - The simulated cantilever beam (all dimensions are expressed in millimetres).*

The PVDF coefficients used for simulations described in this section were the same as in case study 1, reported in (3.10), (3.11) and (3.12).

Since the analysis involves piezoelectric material, mechanical and electrical conditions have to be set (as in section 3.2.2). They are depicted in Figure 3.26. In terms of mechanical conditions, the device is ‘free’ to move under loads caused by wind, except for its lowest surface that is locked. For the electrical boundary conditions, the cantilever has the nearest piezoelectric surface to the right hand silver layer at ‘ground’.

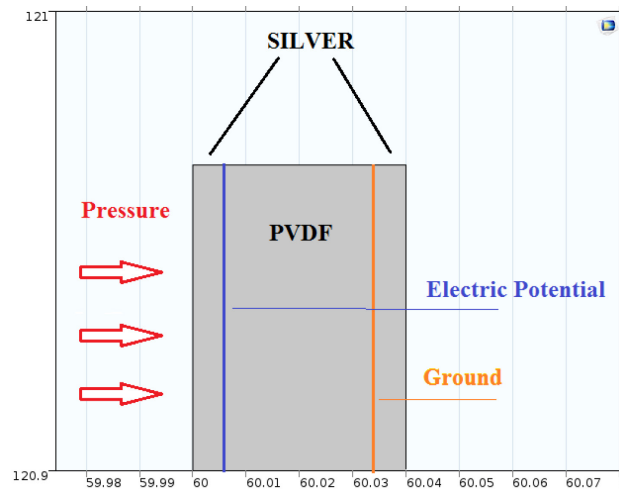


Figure 3.26 – Detail of the geometry of the simulated cantilever beam (all dimensions are expressed in millimetres).

### 3.3.4. Numerical results

In the experimental setup, the induced electric potential was analysed in function of different initial wind velocities. In the simulated environment, the wind velocity of the experimental situation was converted into wind pressure using (3.14). Table VI provides all values of measured wind velocity, calculated wind pressure and the RMS value of generated electric potential, both measured and calculated on the left PVDF surface, after deformation.

TABLE VI - COMPARISON BETWEEN MEASURED AND CALCULATED DATA.

Measured Wind velocity (m/s)	Calculated wind pressure (Pa)	Measured RMS of electric potential (mV)	Calculated RMS of electric potential (mV)	Mean Percentage Error
4.1	10	38.89	38.08	2.08%
4.1	10	41.08	38.08	7.3%
5.3	17.2	54.08	58.27	7.7%
5.3	17.2	57.14	58.27	1.98%
5.3	17.2	51.15	58.27	13.9%
6.7	27.6	98.21	93.51	4.7%
6.7	27.6	95.64	93.51	2.2%

The simulation ignores the mechanical effects due to the plastic film that covers the cantilever beam as well as the higher order dynamics effects, such as resonance or damping on the piezoelectric device. Moreover, the conversion of the value of the wind velocity into that of the wind pressure implies approximations in the calculation of

pressure. Despite these approximations, the average error rate (Table VI) is reasonably low and this confirms the quality of the model and simulation implemented.

### 3.3.5. Simulations with different materials

The aim of this section is to find a piezoelectric material with the best electric response for the cantilever analysed. The validated model was exploited to realize new simulations where the harvester device used was the same shape and dimensions as that used in section 3.3.3 but it was made of one of three different piezoelectric materials: Quartz, PZT-5H and CdS. All the results obtained with new simulations are compared with those obtained with the initial cantilever beam made of PVDF. Other simulation parameters (metallic material used to support the piezoelectric layer, pressure applied and boundary conditions) were not changed. Table VII shows electric values of the results obtained.

TABLE VII - COMPARISON OF ELECTRIC POTENTIAL GENERATED BY DIFFERENT PIEZOELECTRIC MATERIALS.

	Calculated RMS value of electric potential (mV)	Calculated MAX of electric potential (mV)	Calculated MIN of electric potential (mV)	MAX absolute value of electric potential (mV)
<b>Quartz</b>	3.82	26.78	-164.95	164.95
<b>PZT-5H</b>	3.77	0.98	-181.35	181.35
<b>CdS</b>	26.25	47.06	-755.61	755.61
<b>PVDF</b>	38.08	72.50	-2.54	72.50

Figure 3.27 shows a plot of comparison of the four absolute RMS values of the electric potential generated by the different piezoelectric materials.

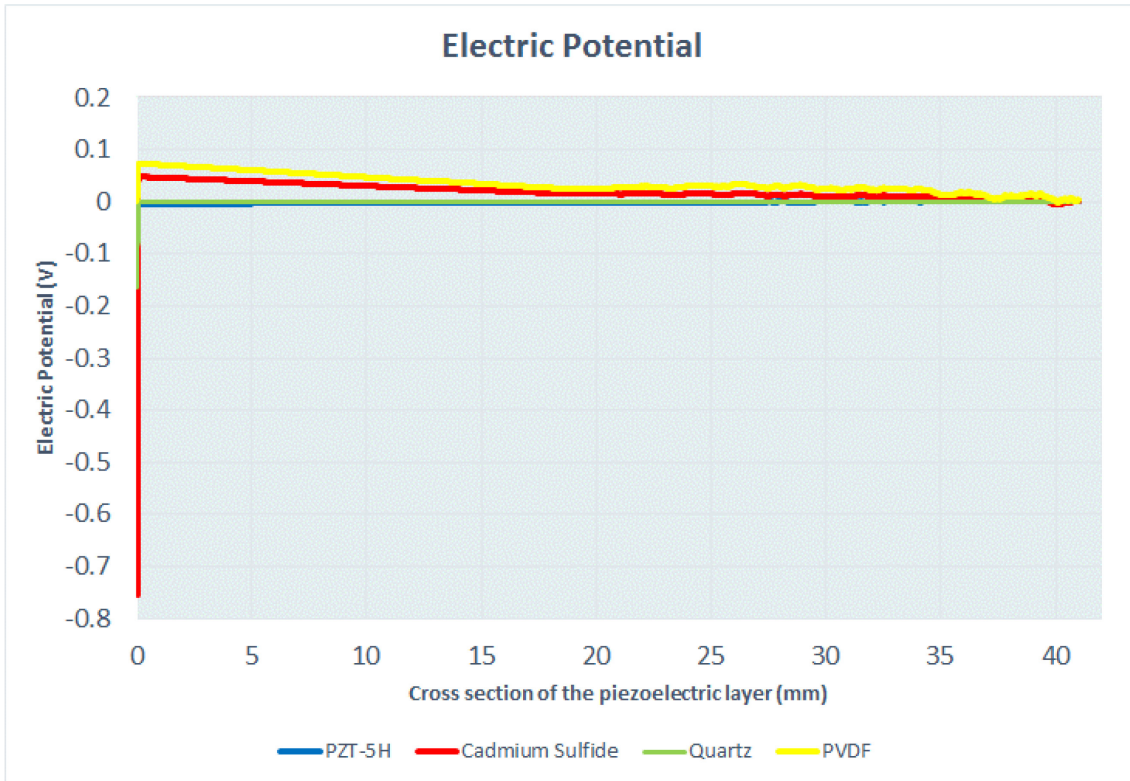


Figure 3.27 - Comparison of RMS values of electric potential generated using 4 different piezoelectric materials.

The histograms in Figure 3.28 show the minimum and the maximum absolute values of the electric potential generated.

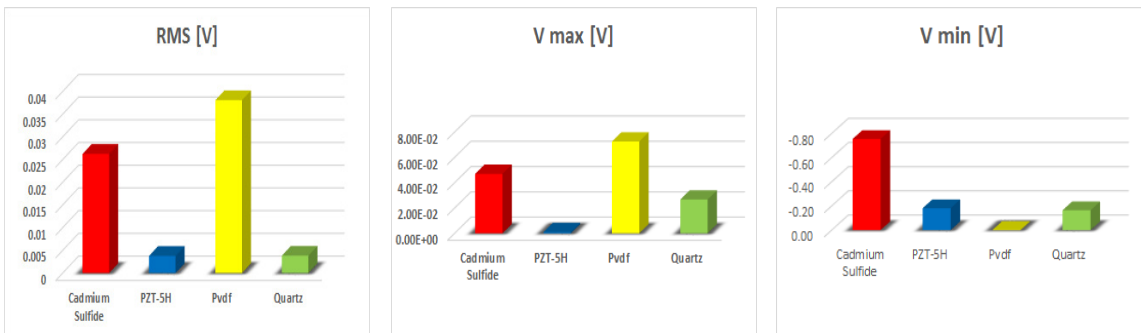


Figure 3.28 - Comparison of electric potential generated using different piezoelectric materials.

Even though the minimum and maximum values were obtained using CdS and PVDF, respectively, the comparison of RMS values shows the polymeric material PVDF as the best compromise for the proposed situation. This is due to the flexibility of this material that allows the cantilever beam to undergo greater deformation than with the other materials. Consequently it generates a higher voltage.

### 3.3.6. Simulation with different shapes

All the results described in the previous section refer to a cantilever beam with a parallelepiped shape and fixed dimensions. The geometric optimization of harvester devices is a well-known and still open problem in the literature. It has previously been discussed by Noh and Yoon in [14], by Goldschmidtboeing and Woias in [15] and by Roundy et al. in [16] who compare three different bimorph cantilever beams. They had the same volume of piezoelectric material (PZT) but different shapes (rectangular, trapezoidal and triangular). It is shown that a trapezoidal geometry can supply more than twice the energy (per unit volume PZT) than the rectangular geometry.

Due to the relationship between deformation and output power produced by the cantilever, geometric dimensions and shape factors have been investigated in order to find the most suitable combination of factors to optimize the output electric potential. KIMEME [17], a novel optimization platform, was used to conduct such an optimization investigation. KIMEME was used to integrate Matlab and Comsol Multiphysics in an optimization project. These tools are coordinated in order to redefine the geometry and to run numerical simulations at every step of the optimization procedure. This integration of processes is graphically described using a data flow graph, as depicted in Figure 3.29.

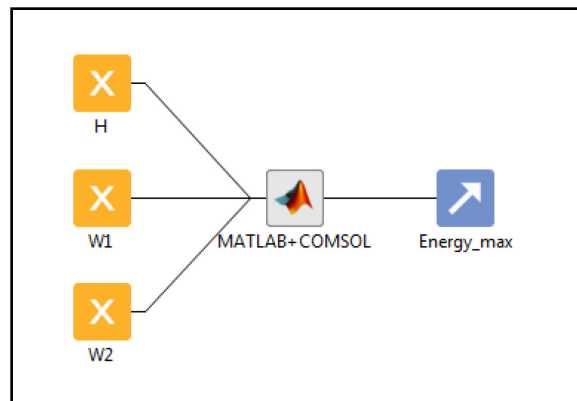


*Figure 3.29 - Optimization project schematics*

The main geometrical parameters of the moving element in the device (e.g. length, width on the bottom and top sides) were included in the optimization project as variables for each design.

The electrical energy produced by the device, when stimulated by a constant pressure equal to 10 (Pa), was used as the objective function to be maximized. Bound Optimization BY Quadratic Approximation (BOBYQA), developed by Powell [18], was used as the main optimization algorithm, as it has proved efficient in terms of convergence speed when computationally expensive simulations are involved.

Using the KIMEME platform, it is possible to optimize these shapes and dimensions in order to achieve a better production of electric potential and energy to harvest.

The geometric parameters used to define the form factor of the cantilever and its dimensions are shown in Figure 3.30.

Three geometric parameters have been considered to describe a variable form factor and sizing of the beam, width at the clamped and free side ( $W1$  and  $W2$ ) and the length of the beam ( $H$ ).

The geometric structure of the cantilever is obtained using three layers. The two external layers are silver foil, thickness 0.06mm each. A PVDF element of 0.28mm is positioned between the two silver layers.

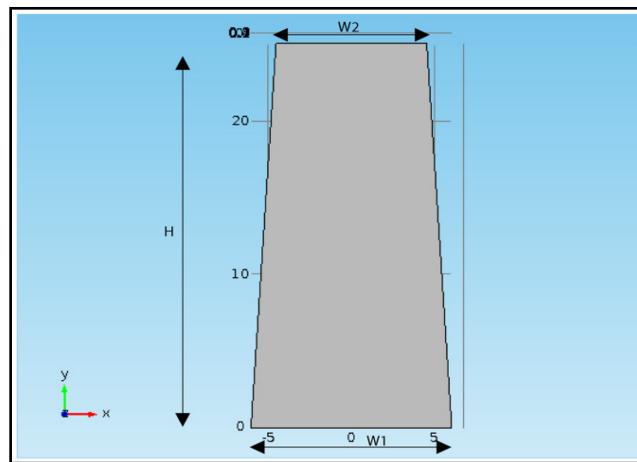


**Figure 3.30 - Geometric parameterization of the cantilever (all dimensions are expressed in millimetres)**

A local search optimization run, using the BOBYQA algorithm implemented in KIMEME, was launched to identify the most efficient design in terms of peak voltage produced. The bounds for parameters  $W1$ ,  $W2$  and  $H$  are listed in Table VIII.

TABLE VIII - DESIGN SPACE BOUNDS

Parameter Name	Min Value	Max Value
W1	5	30
W2	5	30
H	30	50

The optimization was carried on for 33 iterations and the objective function values for each iteration of the procedure are shown in Figure 3.31.

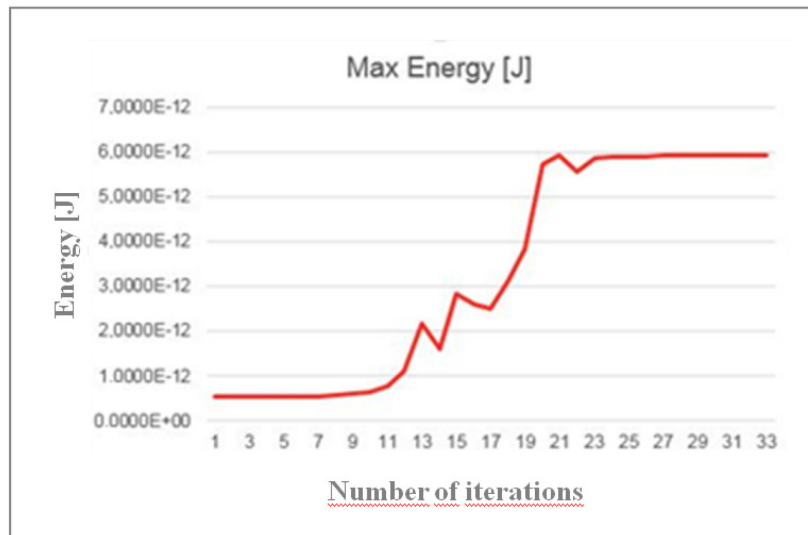


Figure 3.31 -Objective function trend during the optimization as a function of the number of iterations.

Figure 3.32 shows the final design at the end of the optimization procedure, while Figure 3.33 shows the original one.

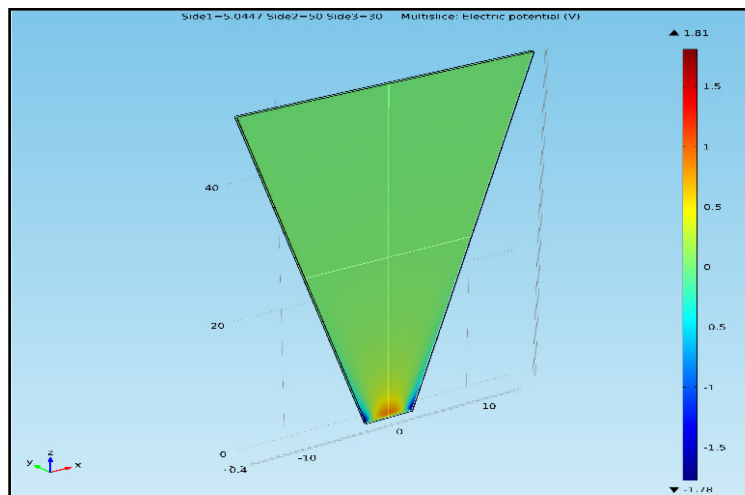
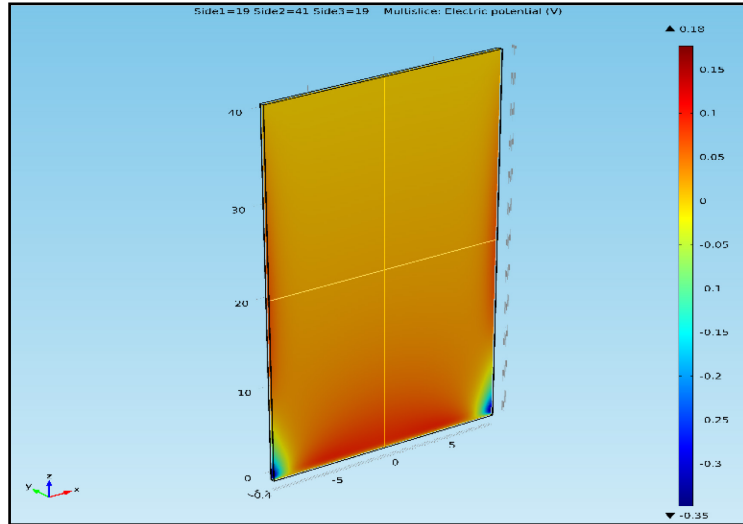


Figure 3.32 - Optimized cantilever design (all dimensions are expressed in millimetres).



**Figure 3.33 - Original cantilever design (all dimensions are expressed in millimetres).**

The result depicted is intuitive since it shows a direct correlation of the efficiency of the system with respect to the clamped side size and the length of the cantilever beam. However, a minor effect of the free side length is shown.

The results obtained are in perfect agreement with those reported in the literature [15], [16]. Moreover, they allow the identification of geometric parameters of the optimal shape predicted for the simulated object, which is an improvement in the design process of harvester devices.

Table IX shows a comparison between the results obtained with the original shape and the optimized one.

TABLE IX - COMPARISON OF ELECTRIC PERFORMANCE

	<b>MIN Electric Potential [V]</b>	<b>MAX Electric Potential [V]</b>	<b>RMS Electric Potential [V]</b>	<b>Energy [J]</b>
<b>Original shape</b>	-0.35	0.18	0.044	5.40E-13
<b>Optimized shape</b>	-1.78	1.81	0.066	5.92E-12

### 3.4. In-depth analysis of FEM mesh

The building of a good mesh is a crucial point in FEM simulations in order to have a convergent solution. Several studies have been carried out with this purpose. Some of them were looking for an automatic algorithm to build a good mesh [19-21], others were looking for the best configuration for objects with particular shapes [22-23].

Thin layers are extremely difficult to simulate with FEM, for the reasons explained in section 3.1. Rodriguez-Zermeno et al. [23] proposed an interesting solution to build an appropriate mesh for this kind of objects. The study described in this section moves on from these results and proposes a comparison between FEM simulations of a piezoelectric cantilever beam, with the dimensions of a thin layer, stressed by a given pressure [9]. The analysis was carried on in a two-dimensional environment and with two different kinds of mesh: free triangular and mapped. The simulated object was the same as that analysed in section 3.3.

#### 3.4.1. *A multiplier factor.*

The first strategy proposed to simulate a real thin layer was to consider layers with greater thicknesses and therefore simpler to simulate. The output variables of the layer with the real thickness were extrapolated from the results of simulated greater thicknesses.

The thickness of the layer was multiplied by a factor ranging from 10 to 1, in the case analysed. For each thickness, the layer was stressed with a pressure of 1 Pa and the reaction of the cantilever beam was observed for a time of 3s. The values of the average and the maximum electric potential generated on the left line of PVDF layer (Figure 3.26) were simulated, as well as the total displacement of the layer. Table X summarizes all these values for each different thickness. The free triangular mesh automatically generated by Comsol Multiphysics was used. Table X also shows the number of Degrees of Freedom (DoF) and the computational time for each thickness.

TABLE X - OUTPUT VALUES OF SIMULATIONS

<b>Thickness Multiplier Factor</b>	<b>Max Voltage [V]</b>	<b>Average Voltage [V]</b>	<b>Total Displ. [mm]</b>	<b>DoF</b>	<b>Comput. time [s]</b>
10	0.010269	0.0052439	0.0010714	34329	15
9	0.010296	0.0052488	0.0014688	38109	18
8	0.010324	0.0052537	0.0020905	42877	24
7	0.01035	0.005258	0.003119	48959	25
6	0.010378	0.0052627	0.0049506	57079	31
5	0.01041	0.0055689	0.0085522	68497	37
4	0.01044	0.0052741	0.0167	85805	56
3	0.010475	0.0052809	0.039592	114135	2130
2	0.0114887	0.00529385	0.13363	171205	12219
1	0.020132	0.00530505	1.0718	342017	19714

Figure 3.34 shows the plot of the maximum voltage generated by the transducer for each thickness.

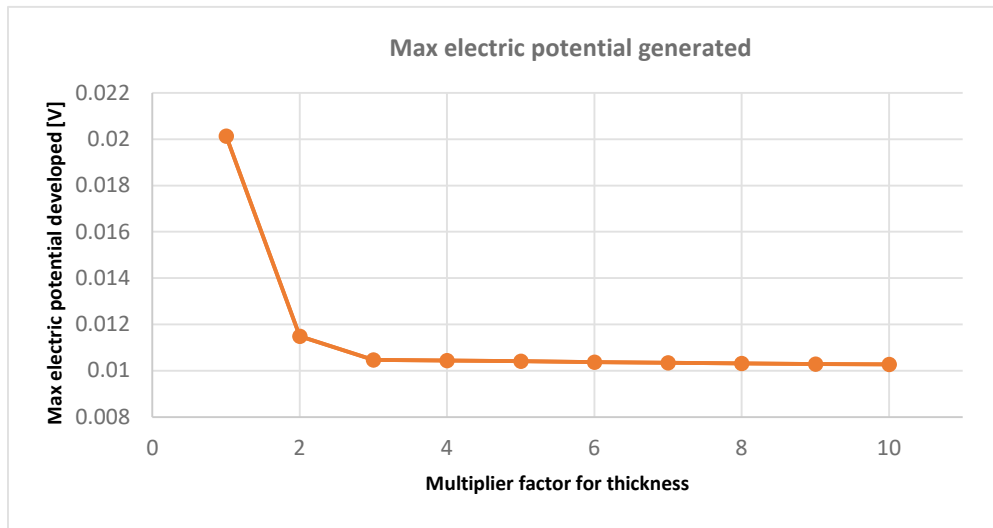


Figure 3.34 - Maximum electric potential generated for different thicknesses

Observing Table X and Figure 3.34, it is easy to note that the output values for the lowest thicknesses (the real thickness and double the real thickness) do not follow the linear trend, as is well shown in Figure 3.35, from which the voltages obtained with the first two thicknesses have been omitted.

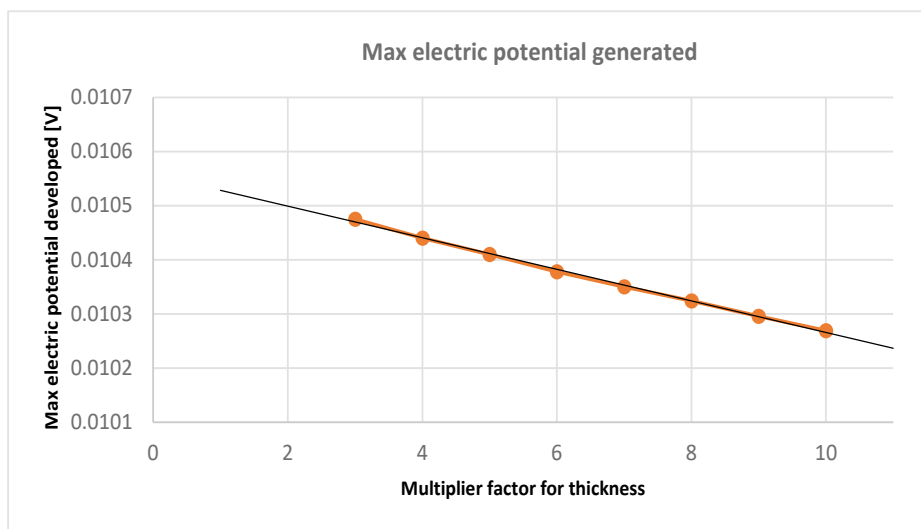
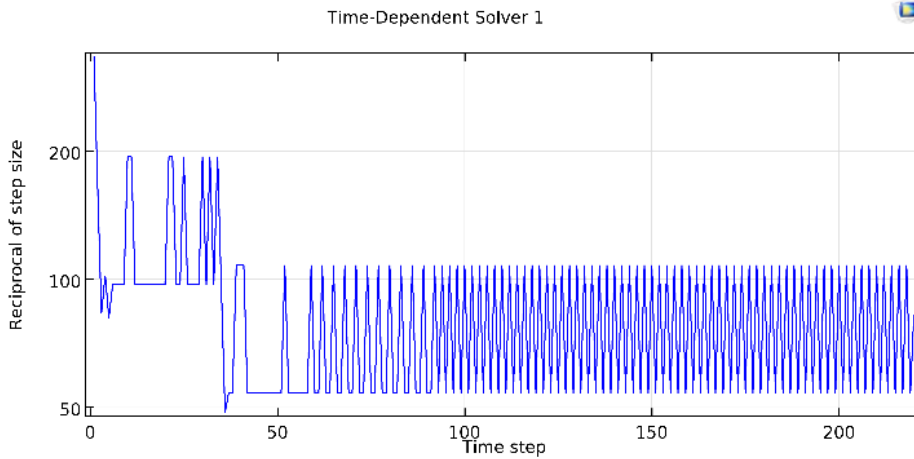


Figure 3.35 - Max electric potential generated for different thicknesses with multiplier factor from 10 to 3.

This anomalous behaviour was due to convergence problems of the simulating software for very low thicknesses, as shown from the convergence plots in Figure 3.36 and Figure 3.37, obtained by simulating the lowest and the highest thicknesses, respectively.

Figure 3.37 shows the expected behaviour, with the reciprocal of the step size steadily reducing as a function of the time step and eventually settling at a minimum. Very different behaviour is shown in Figure 3.36 where, after an initial reduction in the reciprocal of the step size, a swinging between two high values sets in and no minimum is reached.



**Figure 3.36 - Convergence plot for the real thickness.**

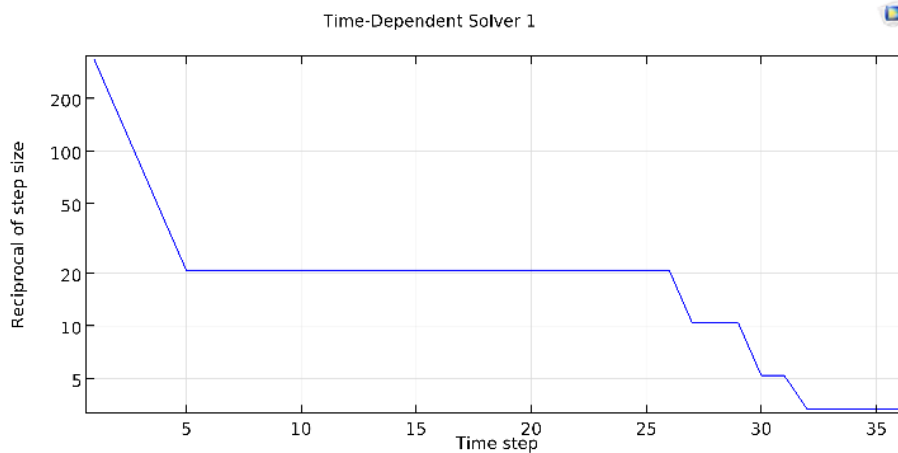


**Figure 3.37 - Convergence plot for the greatest thickness.**

Similar considerations could be extended to all the data in the last two rows of Table X. The two lowest thicknesses therefore have to be dropped and will not be considered in further analysis. However, the linear trend of the first 8 thicknesses can be used to extrapolate these values. The analysis of the trend line in Figure 3.35 allows to calculate 0.010597V as value for the maximum electric potential. Similarly, the extrapolated value for the average generated voltage can be 0.0053V.

### 3.4.2. A different mesh.

A free triangular mesh was created for all simulations described up to now. In order to solve some of the simulating problems described above, the same simulations were repeated using a mapped mesh, with the same number of nodes as the free triangular one on the longest side of the transducer. Table XI shows the same output variables as Table X, calculated with the mapped mesh. The simulations with the multiplier factors 2 and 1 had the same problems as those described in section 3.4.1 with the convergence plots and so they were also discarded in this study.

TABLE XI - OUTPUT VALUES OF SIMULATION WITH MAPPED MESH

<b>Thick. Multiplier Factor</b>	<b>Max Voltage (V)</b>	<b>Average Voltage (V)</b>	<b>Total Displ. (mm)</b>	<b>Comput. time (s)</b>
10	0.010205	0.0052141	0.0010652	36
9	0.010231	0.0052189	0.0014608	53
8	0.01026	0.0052245	0.0020789	56
7	0.010289	0.0052299	0.0031017	41
6	0.010318	0.005235	0.0049231	47
5	0.010348	0.0052402	0.0085039	50
4	0.010379	0.0052451	0.016603	58
3	0.01041	0.0052492	0.039335	85

Table XI does not show the number of DoF because in simulations with the mapped mesh it stays constant at 97394 for any thickness. This number is higher than those in the first 7 rows of Table X but becomes interesting for thickness with multiplier 3. Moreover, this does not have a heavy impact on computational time.

The good quality of the simulation with the mapped mesh in terms of output results is shown in Table XII which contains the absolute values of percentage relative deviation obtained by calculating outputs with the mapped mesh instead of the triangular one. The maximum deviation estimated is 0.65 %.

TABLE XII - PERCENTAGE DEVIATION VALUES OF SIMULATION WITH MAPPED MESH

<b>Thick. Multiplier Factor</b>	<b>Max Voltage (%)</b>	<b>Average Voltage (%)</b>	<b>Total Displ. (%)</b>
10	0.62	0.57	0.58
9	0.63	0.57	0.54
8	0.62	0.56	0.55
7	0.59	0.53	0.55
6	0.58	0.53	0.56
5	0.60	0.54	0.56
4	0.58	0.55	0.58
3	0.62	0.60	0.65

### 3.4.3. Mesh Streamlining.

Another strategy that can be adopted to reduce computational time is a reduction in the number of elements of mapped mesh. Table XIII shows the computational time and the maximum percentage relative deviation obtained from the simulations with a greater reduction in nodes on the longest side of the layer. The error was calculated both referring to the triangular mesh and to the mapped one without node reduction. Table XIII shows that the maximum error detected with these simulations is 1.33% and the analysis was stopped with a reduction of 70% of the nodes on the longest side of the layer because an error higher than 1% was reached. Future research could investigate the best percentage reduction of nodes for a given maximum error, with an automatic procedure.

TABLE XIII - ANALYSIS OF SIMULATION WITH REDUCTION OF NODES

<b>Reduction of nodes (%)</b>	<b>DoF</b>	<b>Elements on longest side</b>	<b>Max error compared to triangular mesh (%)</b>	<b>Max error compared to mapped mesh (%)</b>	<b>Max comput. Time (s)</b>
0	97394	5125	0.65	0	85
10	87666	4613	0.66	0.03	78
30	68210	3589	0.71	0.07	61
50	48697	2562	0.85	0.2	47
70	29222	1537	1.33	0.69	29

The computational time of the last column in Table XIII refers to triple the real thickness, that is the longest thicknesses analysed. These values are very competitive compared with those referring to the triple thickness in Table X (2130).

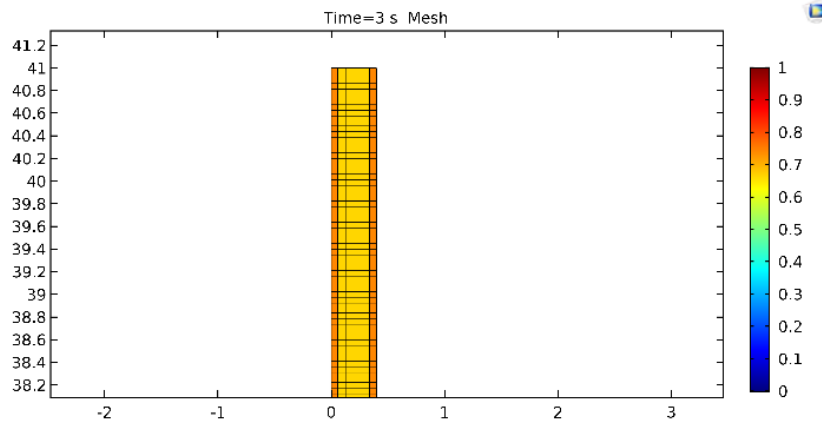


**Figure 3.38 - Mesh quality for triple thickness with mapped mesh reduced by 70% nodes.**

The minimum mesh quality is an important parameter to evaluate in order to build a good mesh, this is a number between 0 and 1 and an acceptable mesh quality is larger than 0.1. Moreover, Figure 3.38 shows a detail for the quality of the mapped mesh with a reduction of 70% of nodes on the longest side of the layer. In the case studied, the minimum element quality was 0.6655 while the average element quality for the whole system was 0.6911. Figure 3.38 confirms the good quality of mesh obtained with the strategies applied to reduce computational time.

### **3.5. Case study 3: interaction of a cantilever beam with a fluid.**

In recent years, a wide range of devices, based on piezoelectric materials, has been developed both on large and small-scales for various applications. A lot of interest has been directed to piezoelectric transducers stressed by natural vibrations, such as those induced by rain or wind [24-27]. The studies of piezoelectric devices are often based on extensive simulations to accurately reproduce the transducers and their behaviour under induced-vibrations. The earliest simulations were based on the isolated observation of a single physical phenomenon. The growing development of more sophisticated and better performing software packages, based on FEM, is opening new frontiers to simulation environments, nowadays. They are able to reproduce multiphysics phenomena as they really happen in nature [28]. Piezoelectric device models can also profit from the improvement given by such multiphysics simulation environments [29-31]. The interaction between the turbulent flow of a fluid and the piezoelectric effect, which is an electrostatic phenomenon, is reproduced in this section.

As in case study 2, this case study proposed the modelling and simulation of a piezoelectric transducer, validated by experimental results, with the difference that the wind was simulated as a flowing fluid, as in the model proposed by [29]. The experimental apparatus was the same as that described in case study 2.

### *3.5.1. Mathematical Modelling and Simulation Environment*

In order to simulate the air-cantilever interaction and the consequent piezoelectric effect, three different physics environments of Comsol Multiphysics were coupled: the Fluid-Structure Interaction (FSI), the Solid Mechanics (SM) and the Electrostatics. The FSI models phenomena where a fluid and a deformable solid affect each other, using the Arbitrary Lagrangian-Eulerian (ALE) technique. The ALE method is used to incorporate the geometrical changes of the fluid domain; a moving grid is used to deal with the dynamic of the deforming geometry and moving boundaries [28]. In the case analysed, the air flow caused a deformation of the piezoelectric object and so the generation of electric potential, due to the piezoelectric effect. This latter phenomenon was simulated using the Piezoelectric Effect (PE) environment of Comsol Multiphysics, which couples the SM module with the Electrostatic one automatically, unlike the coupling between FSI and PE.

In the simulation environment, the cantilever was built with the same shape, dimensions and material as that used in the experimental setup. A rectangular wind channel was set and the wind was studied as air that flows in the channel with an initial velocity, entering through the inlet, moving with a turbulent flow, and leaving the channel through the outlet, having fluid-structure interaction with the cantilever beam. The piezoelectric device reacted to fluid-wind pressure with a deformation, which in turn generated electric potential. A section of the system is shown in Figure 3.39 while Figure 3.40 shows a zoom of the region containing the cantilever beam, where the PVDF layer is shown in colour.

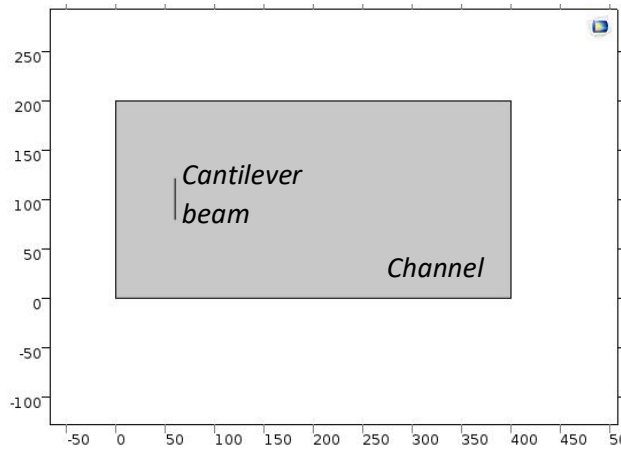


**Figure 3.39** – A section of the system showing the wind channel and cantilever beam

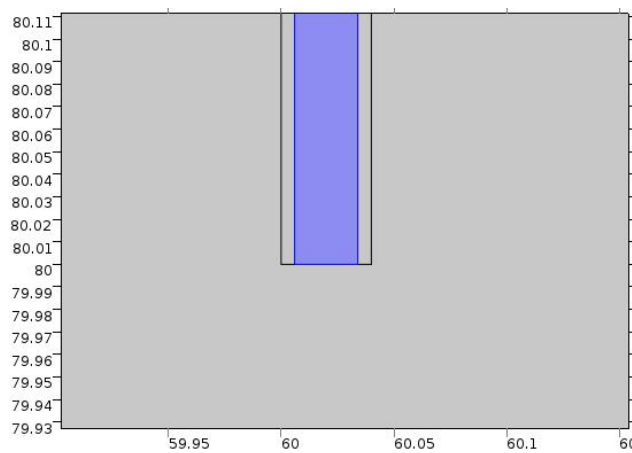


**Figure 3.40** - Zoom in the region containing the cantilever beam

The dimensions of each component are reported in Table XIV.

**TABLE XIV - CHANNEL AND CANTILEVER BEAM DIMENSIONS**

	<b>Parameter</b>	<b>Value</b>	<b>Unit</b>
<b>Silver Layer</b>	Length	41	mm
	Width	12	mm
	Thickness	6+6	$\mu\text{m}$
<b>PVDF</b>	Length	41	mm
	Width	12	mm
	Thickness	28	$\mu\text{m}$
<b>Channel</b>	Length	400	mm
	Height	200	mm

The process was analysed with a time dependent study. The behaviour of each part of the system was described using appropriate equations, described in the following subsections.

### 3.5.2. Fluid Model

Even though the fluid considered in this analysis is a gas and not a liquid, it could be assumed to act as an incompressible fluid because air behaves as an incompressible fluid until its velocity reaches 0.3 as Mach number (ratio of the fluid velocity to the speed of sound in the same fluid). Another important value useful to understand fluid turbulence is the Reynolds number  $Re$ , defined by (3.18):

$$Re = \frac{\rho u L}{\mu} \quad (3.18)$$

where  $\rho$  is the fluid density,  $\mu$  is the fluid dynamic viscosity,  $u$  is the fluid velocity and  $L$  is the length of the obstacle that the fluid encounters. A value of  $Re < 2300$  means that the flow is laminar. In Table XV there are some Reynolds numbers calculated for the analysed system for different fluid velocities.

TABLE XV - REYNOLDS NUMBERS AT DIFFERENT INPUT VELOCITY

Fluid Velocity [m/s]	$Re$
1.3	3529.5
1.4	3801
1.5	4072.5
1.6	4344

Table XV shows that the Reynolds number was much higher than 2300 for each input velocity, making it necessary to study a turbulent flow in order to simulate the fluid behaviour properly. The Reynolds Averaged Navier-Stokes (RANS) formulation with the k- $\varepsilon$  model was used. It is described using the *Navier-Stokes equations*, the *continuity equation for incompressible flow* and the *transport equation for k and  $\varepsilon$*  respectively (3.19-3.23):

$$\rho \frac{\partial u}{\partial t} + \rho(u \cdot \nabla)u = -\nabla p + \nabla \cdot ((\mu + \mu_T)(\nabla u + (\nabla u)^t)) + F \quad (3.19)$$

$$\rho \nabla \cdot u = 0 \quad (3.20)$$

$$\rho \frac{\partial k}{\partial t} + \rho(u \cdot \nabla)k = \nabla \cdot ((\mu + \frac{\mu_T}{\sigma_k})\nabla k) + P_k - \rho \varepsilon \quad (3.21)$$

$$\rho \frac{\partial \varepsilon}{\partial t} + \rho(u \cdot \nabla)\varepsilon = \nabla \cdot ((\mu + \frac{\mu_T}{\sigma_\varepsilon})\nabla \varepsilon) + c_{\varepsilon 1} \frac{\varepsilon}{k} P_k - c_{\varepsilon 2} \rho \frac{\varepsilon^2}{k} \quad (3.22)$$

$$P_k = \mu_T (\nabla u : (\nabla u + (\nabla u)^t)) \quad (3.23)$$

where  $t$  is the time,  $\mu$  is the fluid dynamic viscosity,  $\rho$  is the fluid density,  $u$  is the fluid velocity,  $p$  is the fluid pressure,  $k$  is the turbulent kinetic energy,  $I$  is the unit diagonal matrix, the superscript  $t$  denotes the transpose vector,  $F$  are the external forces applied to the fluid,  $\varepsilon$  is the turbulent dissipation rate,  $P_k$  is an intermediate variable, and  $\mu_T$  is the turbulent viscosity expressed by (3.24):

$$\mu_T = \rho c_\mu \frac{k^2}{\varepsilon}. \quad (3.24)$$

The model constants  $\sigma_k$ ,  $\sigma_\varepsilon$ ,  $c_{\varepsilon 1}$ ,  $c_{\varepsilon 2}$  and  $c_\mu$  in equations (3.21), (3.22) and (3.24) were determined from experimental data [32] and are listed in Table XVI.

TABLE XVI - MODEL CONSTANTS

Constant	Value
$c_\mu$	0.09
$c_{\varepsilon 1}$	1.44
$c_{\varepsilon 2}$	1.92
$\sigma_k$	1.0
$\sigma_\varepsilon$	1.3

The model ignores gravity and other volume forces affecting the fluid, so  $F=0$  in (3.19).

### 3.5.3. Fluid-structure interaction Model

The interaction between fluid and the cantilever beam is governed by the following equation (3.25):

$$\rho \frac{\partial^2 u_{solid}}{\partial t^2} - \nabla \cdot T = F_V, \quad (3.25)$$

where  $\rho$  is the solid density,  $u_{solid}$  is the structural displacement vector,  $t$  is the time,  $T$  is the stress tensor and  $F_V$  are the volume forces. While equation (3.26) defines the fluid load on the structure and how structural displacements affect the velocity of the fluid [28]:

$$T \cdot n = [-pI + \mu(\nabla u + (\nabla u)^t)] \cdot n \quad (3.26)$$

where  $T$  is the stress tensor,  $u$  is the fluid velocity,  $p$  is the fluid pressure,  $I$  is the unit diagonal matrix,  $\mu$  is the fluid dynamic viscosity,  $n$  is the unit vector normal to the boundary and the superscript  $t$  denotes the transpose vector.

### 3.5.4. Electromechanical coupling Model

The energy generated by the PVDF layer, due to the deformation caused by the wind, is

calculated using the constitutive equations of piezoelectric materials in the stress-charge form (1.3).

### 3.5.5. Simulations

Comsol Multiphysics, using equations (3.19-3.26) and (1.3), was used to simulate the behaviour of the cantilever in the channel, under wind effect. Figure 3.39 and 3.40 show the two sub-domains considered for the numerical simulations, i.e. the channel where the air flowed and the cantilever beam made of two silver layers and one PVDF layer. PVDF matrices used were (3.10-3.12).

### 3.5.6. Boundary Conditions

As for boundary conditions it was necessary to consider the cantilever ‘free’ to move under loads caused by wind flow, except for its lowest surface that was clamped, while the channel was completely fixed.

The input for the model was the inlet fluid velocity with a direction normal to the inlet surface. The fluid velocity and solid displacement fields were both set to zero for initial conditions. To avoid inconsistencies in initial conditions, the inlet fluid velocity was modelled as a ramp function, which reaches the cut-off value with a slope of 5. All the input values of wind velocity were the same detected by the anemometer in the experimental setup. A zero pressure boundary condition is applied at the outlet section. The interface boundary between the lower silver layer of the cantilever and the PVDF layer was electrically grounded.

### 3.5.7. Material properties

Table XVII provides some useful parameters peculiar of the materials used to build up the system.

TABLE XVII - MATERIAL PROPERTIES

	<b>Property</b>	<b>Value</b>	<b>Unit</b>
<b>Air</b>	Density	1.2032	Kg/m <sup>3</sup>
	Dynamic viscosity	1.8169*10 <sup>-5</sup>	Pa*s
<b>PVDF</b>	Density	1780	Kg/m <sup>3</sup>
	Young's Modulus	3*10 <sup>9</sup>	Pa
	Poisson's ratio	0.09	1
<b>Silver</b>	Density	1.05*10 <sup>4</sup>	Kg/m <sup>3</sup>
	Young's Modulus	8.1137*10 <sup>10</sup>	Pa
	Poisson's ratio	0.3677	1

### 3.5.8. Mesh

Based on the analysis carried out in section 3.4, the optimal aspect ratio for the mesh elements was chosen to be close to 15, in this section. Finally, the cantilever beam was simulated with a mapped structured mesh of 450 elements on the longest dimension and not with a free triangular one. Figure 3.41 shows the good quality of the deformed mesh.

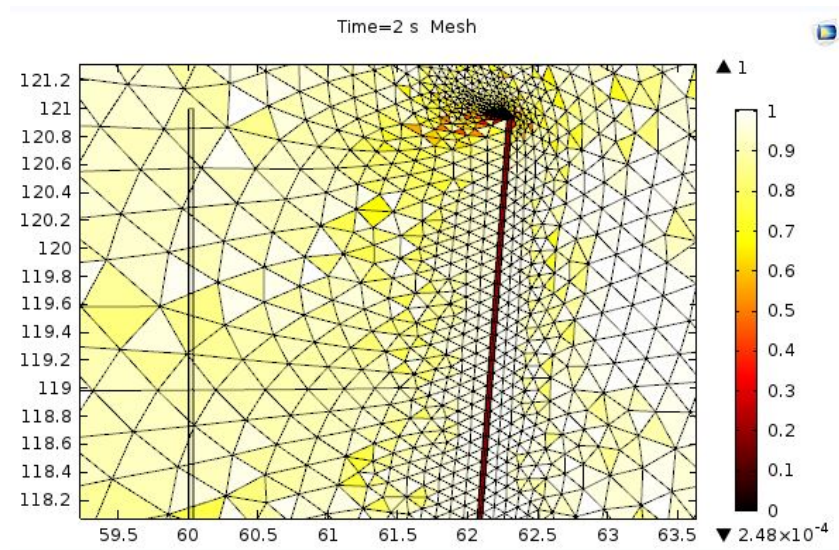
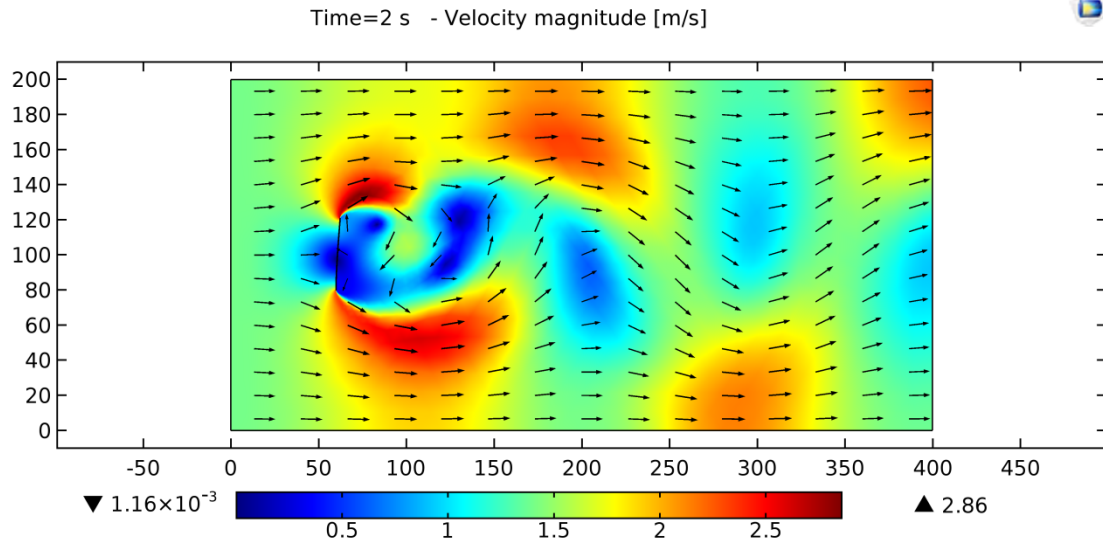


Figure 3.41 - Mesh quality (a value higher than 0.1 indicates an acceptable mesh quality).

The minimum value of the mesh quality was 0.1311, in this case. It was found in elements belonging to the thin layer. The minimum mesh quality in the fluid was 0.3944 and the average mesh quality for the whole system was 0.9003. With this mesh the system had 99907 degrees of freedom.

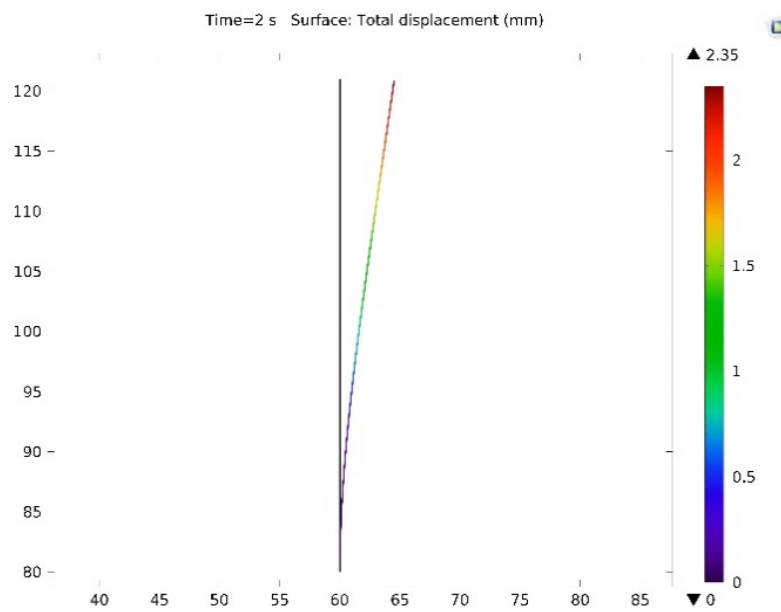
### 3.5.9. Results

The following Figures 3.42-3.44 show the results of a simulation of 2s with an initial wind speed of 1.4m/s. Figure 3.42 shows the wind flow near the cantilever after 2s; the velocity magnitude is highlighted by colours and arrows.



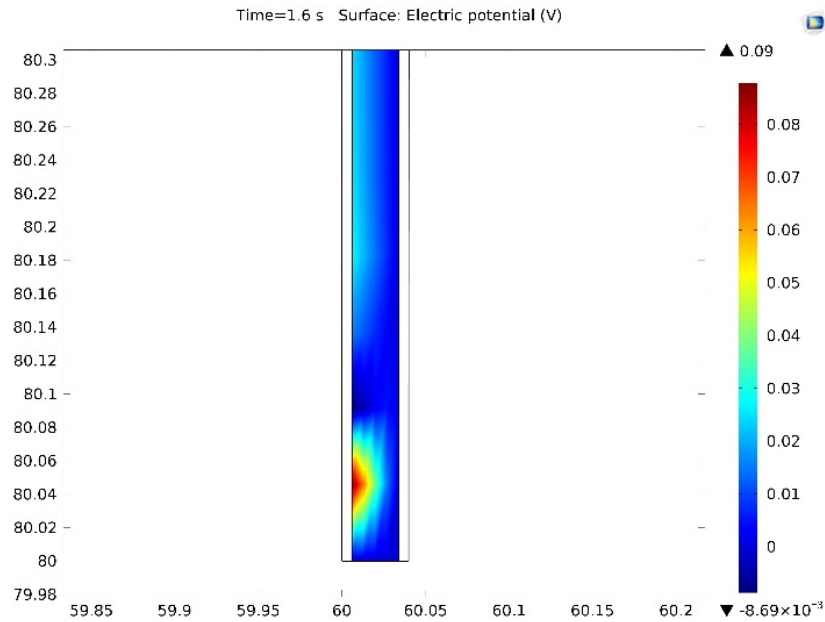
*Figure 3.42 - Wind flowing near cantilever – initial velocity 1.4 [m/s]*

Figure 3.43 shows the cantilever beam deformation under wind effect. The maximum deformation was reached after 2.0s of simulation and was equal to 2.35mm.



*Figure 3.43 - Cantilever deformation under wind effect*

Figure 3.44 shows the electric potential generated by the deformation of the harvester device at the time 2.0s. Its maximum absolute value was 8.69mV and was detected in the lowest part of the beam, near the locked region.



**Figure 3.44 –Electric potential generated by the cantilever under wind effect**

Table XVIII shows the simulated average values of electric potential, measured on the left interface of silver and PVDF, at different simulation times. The first two points were omitted from the table because they refer to an initial speed which had not yet reached the steady state.

TABLE XVIII - SIMULATED AVERAGE ELECTRIC POTENTIAL VALUES (WIND VELOCITY = 1.4 [M/S])

<b>Time (s)</b>	<b>Electric potential (V)</b>
0.4	0.00996
0.6	0.01102
0.8	0.01107
1	0.01109
1.2	0.01118
1.4	0.01136
1.6	0.01212
1.8	0.01207
2	0.01275

Using the setup described in case study 2, the output electric potential was measured on the test line over a range of possible wind velocity values between 1.3m/s and 1.63m/s, interval where the experimental and simulated setups have more stability. The same velocity values were used in the simulation environment. Both the results of the experimental acquisitions and simulation are depicted in Figure 3.45.

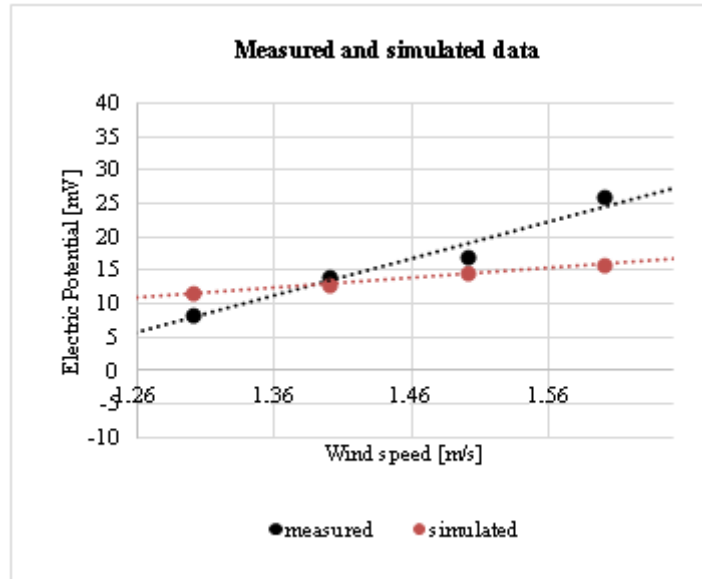


Figure 3.45 - Comparison between measured and simulated data

Figure 3.45 shows that the implemented FEM model was able to reproduce the trend of the electric potential as a function of the wind velocity, obtaining results that can be considered encouraging for complex multiphysics FEM simulations. In fact, this study did not consider the mechanical effect of the plastic film that covers the cantilever beam. Moreover, higher order dynamic effects, such as resonance and damping, were ignored. The simulation setup also needed additional improvements to reproduce the experimental system better. Studies in this respect are already ongoing to increase the matching between simulated and experimental data.

The results presented in this section show a multiphysics numerical simulation approach, in which a turbulent fluid, an energy harvester and their interactions were simulated concurrently and where the proposed model was eventually validated on an experimental test bench.

### 3.6. Case study 4: interaction of a fluid with a cantilever beam locked to a bluff body.

Several configurations include a bluff element capable of generating vortices that cause vibration on a piezoelectric element, thus generating electric power from flow-kinetic energy. This architecture is attractive since it does not contain rotating elements and induction phenomena, and therefore systems based on this idea are simpler to design and assemble.

Moreover, many preliminary studies about the optimal shape and configuration of the bluff body have been conducted [29], [31], showing that a D-shape bluff body is a better holder for a harvester cantilever beam, in terms of efficiency. In fact, there is a correlation between the shape of the bluff body and the vortex-induced vibration (VIV) on the beam. The amount of energy produced by the cantilever is strictly related to the fluid dynamics of the flow around the bluff body. As discussed in [33], in a system similar to the one proposed in this study, a voltage of 0.83V was achieved at an airflow speed of 35m/s. This case study aims at improving the design proposed in [34] by optimizing the shape of the device (with particular reference to the bluff body profile) in order to increase the energy conversion rate at lower speed. As a preliminary step in an ongoing study about the dynamic behaviour and the design optimization possibilities for these devices, the results reported in this section refer to static operating conditions and the optimization process is aimed at maximizing the static open-circuit voltage produced by the micro-cantilever.

The software tool KIMEME was then used to implement an optimization project, in order to iteratively evaluate several different candidate bluff body shapes and to obtain an optimal design that maximizes the electrical output of the system.

### *3.6.1. Parametric Shape Optimization of the Bluff element*

A schematic representation of the micro-cantilever is shown in Figure 3.46. It consisted of a two layered micro-cantilever which was attached to a semicylindric bluff body made of silicon. The cantilever lower layer was made of a thin silicon film, which acted as a support to the upper PZT-5H layer. A parallelepiped channel for the fluid flow was considered in the proposed simulation. The fluid entered the channel with a known low speed, which was normal to the inlet section. The fluid flow deviation, generated by the bluff body, produced a non-zero static pressure difference between the upper and lower faces of the micro-cantilever, which was placed immediately above the bluff body plane of symmetry.

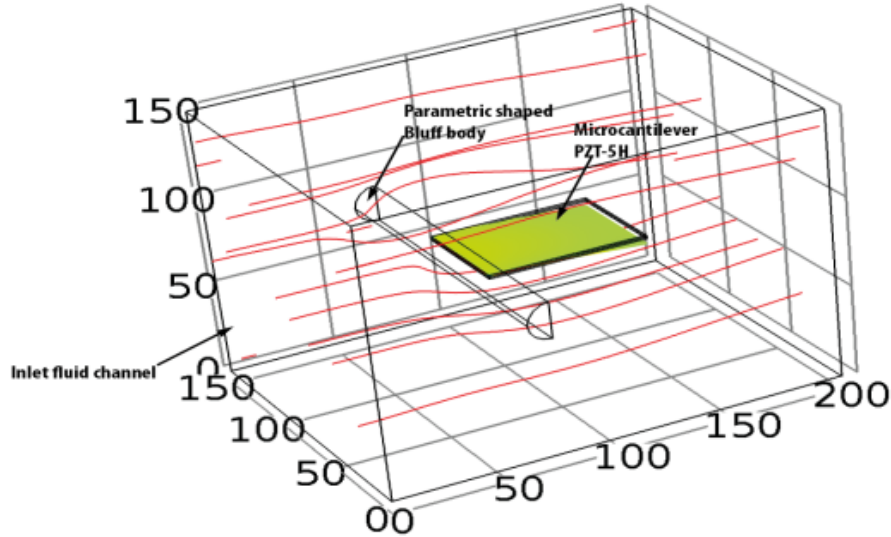


Figure 3.46 - Schematic representation of the micro-cantilever. All dimensions in  $\mu\text{m}$ .

Table XIX summarizes the geometrical parameters of the system in its original, non-optimized, configuration.

TABLE XIX - SYSTEM GEOMETRIC PARAMETERS.

Subdomain	Parameter	$\mu\text{m}$
Fluid Micro Channel	Length	200
	Width	150
	Thickness	150
Cantilever Silicon Layer	Length	70
	Width	50
	Thickness	1
Cantilever PZT-5H Layer	Length	70
	Width	50
	Thickness	1
Silicon D-shape Bluff Body	Length (d/2)	10
	Width	150
	Thickness (d)	20

### 3.6.2. Multiphysics Numerical Setup

The multiphysics simulation was realised by coupling the same three environments of Comsol Multiphysics as in the third case study. They are FSI, SM and Electrostatics. The ALE technique was also used. The fluid flow velocity field  $u$  and pressure  $p$  were evaluated by carrying out the numerical solution of the Navier-Stokes equations (3.19) and (3.20). The elastic formulation of the cantilever structural deformation was expressed by the equation (3.25). Equation (3.26) described the fluid-structure interaction and expressed the relationship between the fluid motion and the forces

perpendicular to the solid domain boundary. Finally, the linear electro-mechanical coupling model was expressed by the equation (1.3).

The elastic behaviour of the silicon subdomain (bluff body + cantilever lower layer) was modelled using the elasticity matrix provided by [35]. Other properties of materials that constituted the system under exam are provided in Table XX.

TABLE XX - PROPERTIES OF THE MATERIALS USED FOR THE FEM ANALYSIS.

Subdomain	Property	Value
Water (Fluid)	Density	1000 kg m <sup>-3</sup>
	Dynamic Viscosity	10 <sup>-3</sup> Pa s
Silicon	Density	7850 kg m <sup>-3</sup>
PZT-5H	Density	7500 kg m <sup>-3</sup>

Simulations reported in this case study were carried out considering an inlet fluid velocity of 1m/s. The Reynolds number for the considered set up was evaluated with Equation (3.18) where  $L$  is the characteristic dimension of the bluff body (semicylinder diameter).

Since the steady state configuration of the system was static, all the simulations needed for the shape optimization process were carried out in static conditions (time derivatives in Equations (3.19) and (3.21) equal to zero). This allowed a significant reduction in both computational time and memory in order to obtain the solution.

As for the boundary conditions, a *no-slip* boundary condition was applied on the lateral walls of the fluid channel. This condition prescribed that the fluid velocity was null near the walls, that is, the fluid at the wall was not moving [28]. The D-shape bluff body was considered fixed in the channel. The interface boundary between the cantilever silicon layer and the PZT-5H film was electrically grounded.

### 3.6.3. Bluff body profile geometric parametrisation

The shape of the D-shaped bluff body was modelled with equation 3.27. Four parameters were identified in order to fully describe the geometrical configuration of the considered device. They are depicted in Figure 3.47 and constituted the main subject of investigation in this optimization study. Quantities  $a_1$ ,  $a_2$ , and  $a_3$  univocally defined the cross sectional profile of the bluff body, while parameter  $a_4$  defined the position of the cantilever referred to the symmetry axis (the y-axis in Figure 3.47) of the bluff body.

Parameter  $a_3$  was evaluated as the first derivative of the following polynomial function evaluated for  $x = a_1$ :

$$y(x) = ax^4 + bx^3 + cx^2 + dx + e \quad (3.27)$$

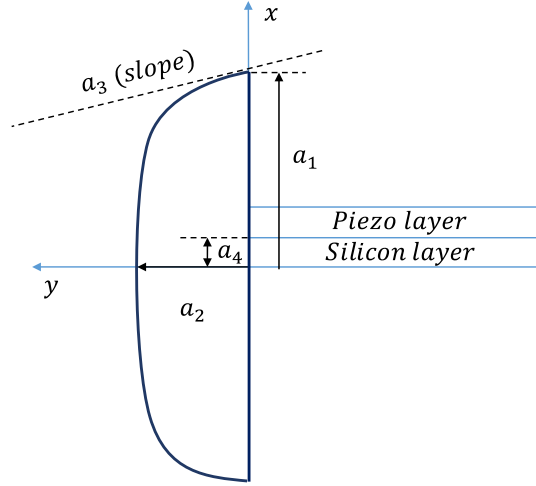


Figure 3.47 - Parametric shape 2D representation of the bluff body.

The solution of the linear system for the boundary conditions depicted in Figure 3.47  $y(0)=a_2$ ,  $y(-a_1) = 0$ ,  $y(a_1) = 0$ ,  $y'(-a_1) = a_3$ ,  $y'(a_1) = a_3$ , led, after a few mathematical manipulations, to the representation of the bluff profile used in this section. It is expressed, as a function of  $a_1$ ,  $a_2$  and  $a_3$ , by the following equation:

$$y(x) = \frac{(a_1^2 - x^2)(2a_1^2a_2 - 2a_2x^2 - a_1a_3x^2)}{2a_1^4} \quad (3.28)$$

#### 3.6.4. Numerical optimization of the parametric Bluff

The optimization procedure adopted for this case study is described in this section and simulation results for both the original and the optimized configurations are presented in section 3.6.5.

The electric potential produced by the cantilever during the simulation was proportional to its deformation. The deformation was produced by the fluid forces, as described in the previous section, therefore the cross profile of the bluff element was the subject of an optimization procedure to identify the most suitable configuration that maximized the surface voltage on the PZT-5H domain, keeping the inlet fluid velocity constant. KIMEME [17] was used to conduct this optimization investigation. Using this tool,

Comsol Multiphysics was integrated in an optimization project in which the four geometrical parameters ( $a_1, a_2, a_3, a_4$ ) were considered to define the design space. This set of optimization variables was input into the Comsol Multiphysics process, in order to regenerate the parametric geometry and execute the numerical simulation for the device. The maximum absolute value of the voltage on the upper PZT-5H surface was extracted from the Comsol Multiphysics simulation and used as a maximization objective for KIMEME. The voltage was evaluated compared to the boundary between the piezoelectric and the silicon layers of the cantilever, which was always grounded. The objective value maximized during this optimization procedure was directly calculated using a Comsol Multiphysics simulation. BOBYQA was used as the main optimization algorithm [18], as it has proven efficient in terms of convergence speed when computationally expensive simulations are involved.

Table XXI shows the design space bounds defined for the parametric bluff, in the second and third column. The fourth column reports the random values used as initial points for the optimization process.

TABLE XXI - OPTIMIZATION BOUNDS, INITIAL AND FINAL POINT.

Parameter	Lower bound	Upper bound	Initial point	Optimized value
$a_1$ [ $\mu\text{m}$ ]	0.1	20	10	11.2
$a_2$ [ $\mu\text{m}$ ]	0.1	10	3.5	2.02
$a_3$ [1]	0.001	5	1	0.52
$a_4$ [ $\mu\text{m}$ ]	0	5	1.85	4.69

The optimization procedure was iterated 34 times, each iteration lasting 35 minutes on a 16 core Intel i7 2.6 GHz server.

The value of the voltage obtained at the end of the optimization procedure was equal to 4.83mV, and it represented an increase of 150% with respect to the value obtained using the initial geometry. It can be observed that the optimization process stopped at a point where parameter  $a_4$  was close to the value chosen as its upper bound (Table XXI). A sensitivity analysis, conducted in the neighbourhood of the optimized parameter set that the produced electric potential was most affected by parameter  $a_4$ . Once parameter  $a_4$  had been decided, the corresponding optimal for  $a_1$  was identified (variations of  $\pm 30\%$  produce a decrease in the electric potential generated). Variations of parameters  $a_2$  and  $a_3$  in the neighbourhood of the optimized set did not produce significant changes in the electric potential.

Figure 3.48 shows the final geometry of the device at the end of the optimization. It corresponds to the parameter set reported in the last column of Table XXI.

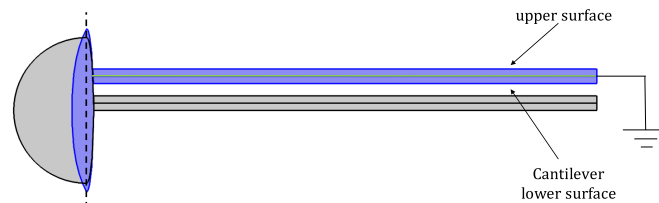


*Figure 3.48 - Comparison between the optimized and the original configuration of the device.*

### 3.6.5. Simulation results

A mapped mesh of 520 elements was adopted for the cantilever beam for all the configurations generated during the optimization process. The fluid domain was subdivided into two regions, depicted in Figure 3.49. The first one, which is closer to the solid domain, had a free quad mesh. The subdomain thickness and the distribution of the relative mesh elements along the bluff profile were made auto-adaptive in order to guarantee a constant number of elements along the normal direction, for each generated configuration. This was meant to adequately evaluate fluid pressure and fluid velocity in regions where the higher gradients are expected. The second fluid domain and the bluff body domain were modelled using a free triangular mesh.

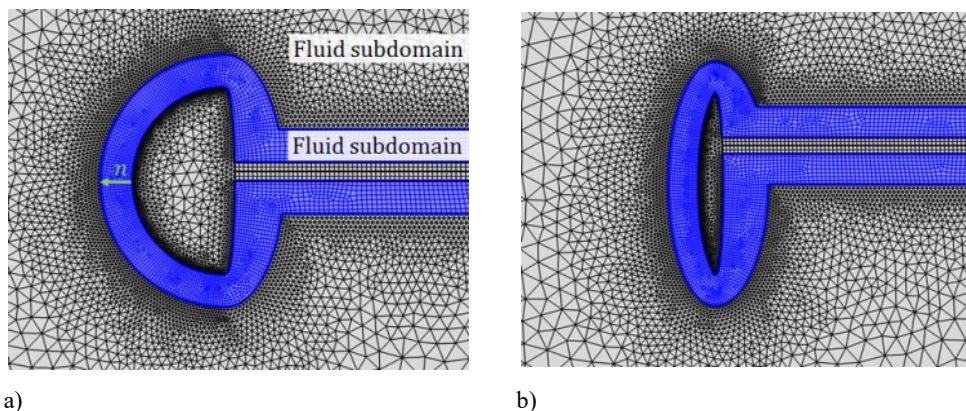


*Figure 3.49 - Details of the mesh created for the original (a) and the optimized (b) device configurations.*

Table XXII reports mesh statistics for the original and optimized configuration cases.

The relative number of DoF is reported in the third column. The average element quality (AEQ) and the minimum element quality (MEQ), in the fourth and the fifth columns, respectively, were evaluated using Comsol Multiphysics as representative indexes of the overall mesh quality. AEQ and MEQ were greater than 0.1 so Table XXII shows a good agreement with the quality requirements.

TABLE XXII - MESH STATISTICS

System configuration	Number of elements	DoF	AEQ	MEQ
Original	25473	85968	0.9601	0.2512
Optimized	23703	79558	0.9615	0.3265

Figure 3.50 shows plots of the fluid velocity components  $u_x^{Fluid}$  and  $u_y^{Fluid}$  evaluated along the  $y'$ -axis (Figure 3.48). The comparison between the curves relative to the optimized configuration (solid lines) and those relative to the original configuration (dashed lines) shows a significant increase in the  $u_y^{Fluid}$  absolute value in proximity of the separation points or points in which the  $y'$ -axis intersects the bluff body.

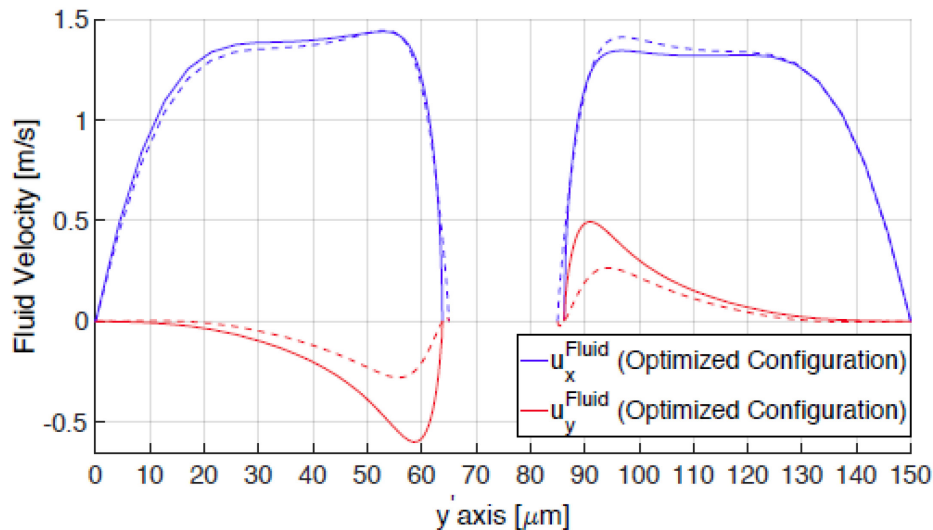


Figure 3.50 - Fluid velocity evaluated along the  $y'$ -axis (Fig. 3.48). Blue and red curves represent the velocity component along the  $x$ -axis and  $y$ -axis (Fig. 3.48), respectively. Dashed lines refer to the relative values in the original configuration.

In order to evaluate the effect of the mechanical stress applied to the cantilever beam, Figure 3.51 shows the pressure along the cantilever acting on both the tested configurations. The reported curves are evaluated as the difference between the pressure profiles on the upper and the lower surface of the cantilever (Figure 3.48). There is a

clear effect of the optimized geometry on the mechanical load transferred by the fluid motion to the cantilever itself.

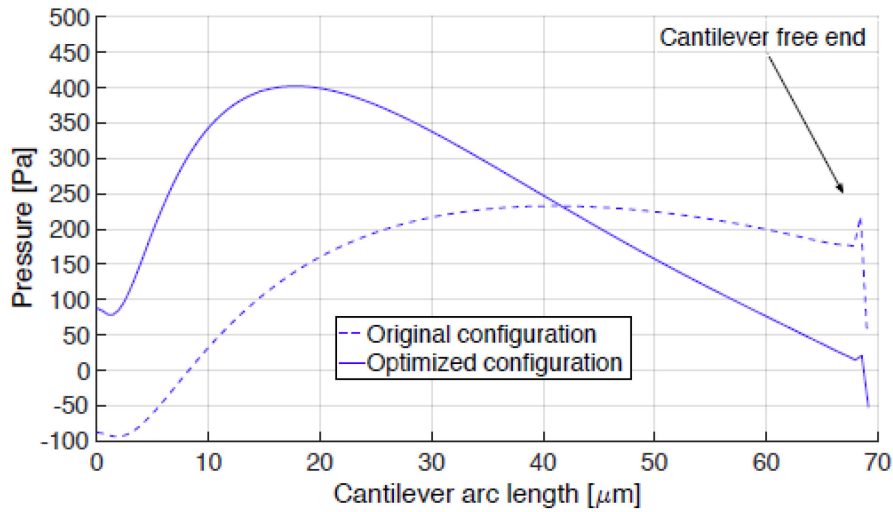


Figure 3.51 - Pressure on the cantilever. Comparison between values computed for the original configuration (dashed line) and the optimized configuration (solid line).

Figure 3.52 shows the effect of the optimized configuration in terms of total cantilever displacement.

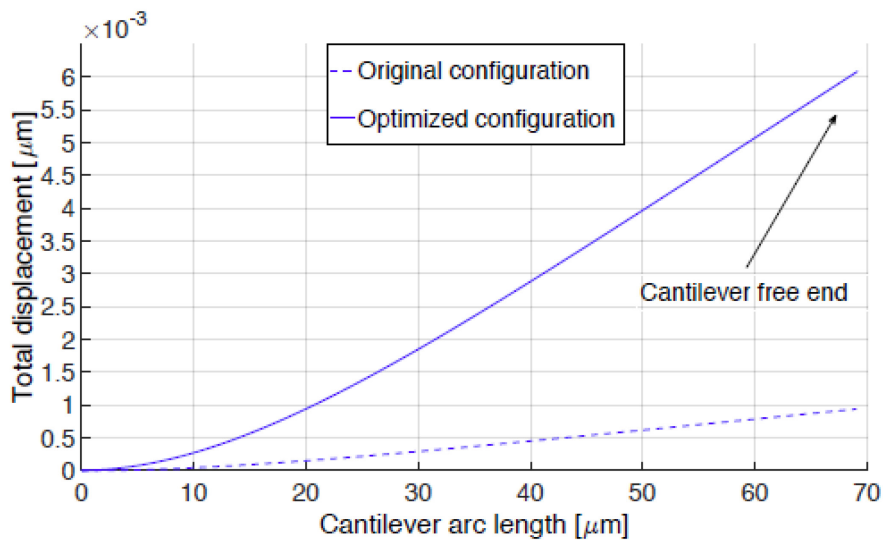


Figure 3.52 - Total cantilever displacement evaluated on the PZT-5H layer upper surface (Fig. 3.48). Comparison between values computed for the original configuration (dashed line) and the optimized configuration (solid line).

The relative increase in the electric potential profile detectable on the upper surface of the PZT-5H layer is shown in Figure 3.53.

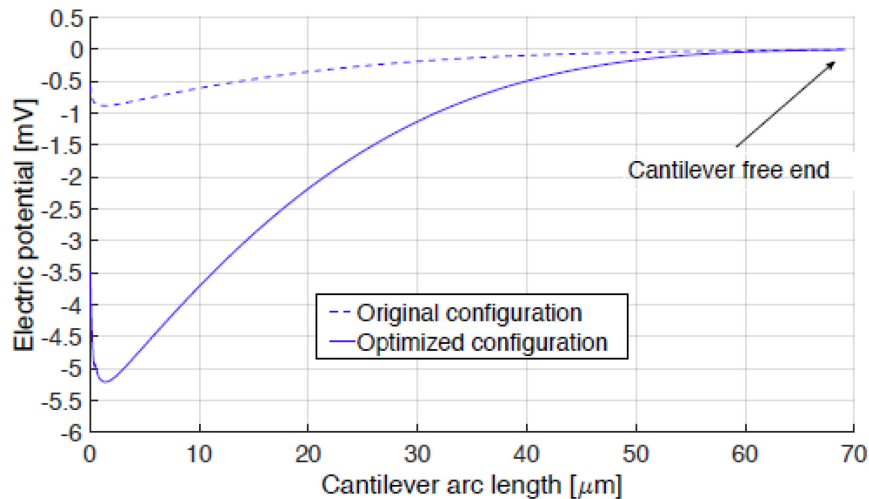


Figure 3.53 - Electric potential evaluated on the PZT-5H layer upper surface (Figure 3.48). Comparison between values computed for the original configuration (dashed line) and the optimized configuration (solid line).

### 3.7. Conclusions.

In this chapter the behaviour of a cantilever beam subjected to wind pressure has been observed and described using a mathematical model. The analysis was carried out through four different case studies.

In the first case study a unimorph cantilever beam made of structural steel and four different piezoelectric materials (PZT-5H, CdS, BGO and PVDF) was investigated. The analysis showed that the most suitable material to generate electric potential in the analysed situation was CdS, both for maximum absolute value and RMS value of voltage generated. On the other hand, CdS generated a lower surface charge density and a lower energy than PZT-5H. The case study ended with an in-depth study into the thickness of the device made of PZT-5H. Different thicknesses, greater or smaller than the initial one, were considered. The best electric potential generated was provided by the cantilever with the minimum thickness analysed, having a size comparable with those produced by manufacturers of piezoelectric devices nowadays.

A piezoelectric cantilever beam subjected to wind pressure was described in the second case study. The study compared the behaviour of a cantilever beam, made of silver and PVDF and subjected to wind force, observed with an experimental apparatus, with that of an FEM model of a device with the same features. The behaviour of the cantilever was modelled using constitutive equations of piezoelectric materials and

mechanical equilibrium equations. A comparison of values of electric potential generated was made. Other simulations were carried out with different piezoelectric materials and different shapes of piezoelectric layer. Comparisons led to choosing the polymeric material as the best compromise, because of the best RMS value of the electric potential generated and the least expensive cost. In addition, the trapezoidal shape was found to be the best one for the piezoelectric layer.

In case study 3, a novel study to analyse and simulate a piezoelectric cantilever beam subjected to wind force was described. The approach used for this case study represents an improvement on the existing literature because of the inclusion of an extended numerical model for the multiphysics interaction between a fluid and a piezoelectric device. The study considered a finite element model of a 2D cantilever beam. The behaviour of the cantilever beam was modelled using the Navier-Stokes equations and the constitutive equations of piezoelectric materials. The results observed in simulation were compared with the corresponding values detected by an experimental setup with a reasonable agreement for FEM simulations, thus validating the simulation approach.

In the last case study, an optimization procedure to design a more complex piezoelectric device has been proposed. The device designed is useful to analyse the interaction of the fluid with a deformable piezoelectric cantilever. A fixed D-shaped bluff body was used to generate flow deviation, resulting in a mechanical deformation on the micro-cantilever. A novel geometric parameterisation is proposed to find the maximum performance of the transducer for a fixed velocity of the flow. The optimized cross section shape was compared with the results of the standard D-shape used in the literature.

## References.

- [1] Yang Y., Shen Q.L., Jin J.M., Wang Y.P., Qian W.J., Yuan D.W. "Rotational piezoelectric wind energy harvesting using impact-induced resonance". *Applied Physics Letters*, 2014, Vol. 105, No. 5.
- [2] Cook-Chennault K.A., Thambi N., Sastry A.M. "Powering MEMS portable devices—a review of non-regenerative and regenerative power supply systems with special emphasis on piezoelectric energy harvesting systems". *Smart Materials and Structures*, 2008, Vol. 17, No. 4, pp. 1-33.
- [3] **Acciani G., Di Modugno F., Gelao G. "Comparative Studies of Piezoelectric Harvester Devices". *Energy Harvesting: Technology, Methods and Applications*. Nova Science Publishers, 2016, pp. 1-18.**

- [4] Acciani G., Adamo F., Di Modugno F., Gelao G. “Modelling and simulation of cantilever beam for wind energy harvesting”. *JVE Journal of Vibroengineering*, 2016, Vol. 18, No. 2, pp. 1167-1174.
- [5] Acciani G., Di Modugno F., Gelao G. “Modelling and simulation of a cantilever beam for wind energy harvesting”. *Proc. of 12th International Workshop on Piezoelectric Materials and Applications in Actuators - IWPMA 2015*.
- [6] Acciani G., Di Modugno F., Mininno E., Montegiglio P. “Multi-physics Simulation of a Wind Piezoelectric Energy Harvester Validated by Experimental Results”. *Proc. of 17th International conference on Thermal, Mechanical and Multiphysics Simulation and Experiments in Microelectronics and Microsystems - EUROSIM 2016*.
- [7] Acciani G., Mininno E., Montegiglio P., Di Modugno F. “Fluid Flow Based Micro Energy Harvester Optimization”. *Proc. of 16th IEEE International Conference on Environment and Electrical Engineering - EEEIC 2016*.
- [8] Acciani G., Di Modugno F., Gelao G., Mininno E. “Shape Optimization of Cantilever Beam for Wind Energy Harvesting”, *Proc. of International Conference on Renewable Energy Research and Applications - ICRERA 2015*, pp. 1207-1212.
- [9] Acciani G., Politi T., Di Modugno F. “Mesh Improvement Criteria in Dynamic Study of Thin Layers with Finite Element Method”. *Proc. of 9th Workshop on Structural Dynamical Systems: Computational Aspects - SDS 2016*.
- [10] "An American National Standard. IEEE standard on piezoelectricity". ANSI/IEEE Std 176, The institute of Electrical and Electronics Engineers Inc. New York, USA, 1988.
- [11] Roh Y., Varadan V.V., Varadan, V.K. "Characterization of all the elastic, dielectric and piezoelectric constants of uniaxially oriented poled PVDF films". *IEEE Transactions on ultrasonics, ferroelectrics, and frequency control*, 2002, Vol. 49, No. 6, pp. 836-847.
- [12] Clapp A.L. "National Electrical Safety Code". IEEE Standard Information Network, 1972.
- [13] <http://www.meas-spec.com/>
- [14] Noh J.Y., Yoon G.H. “Topology optimization of piezoelectric energy harvesting devices considering static and harmonic dynamic loads”. *Advances in Engineering Software* 53, Elsevier, 2012.
- [15] Goldschmidtboeing F., Woias P. “Characterization of different beam shapes for piezoelectric energy harvesting”. *Journal of Micromechanics and Microengineering*, 2008, Vol. 18, No. 10, pp. 1-7.
- [16] Roundy S., Baker J., Carleton E., Reilly E., Lai E., Otis B., Rabaey J.M., Wright P.K., Sundararajan V. “Improving power output for vibration-based energy scavengers”. *Pervasive Computing, IEEE*, 2005, Vol. 4, No. 1, pp. 28-36.
- [17] Iacca G., Mininno E. “Introducing Kimeme, a Novel Platform for Multi-Disciplinary Multi-Objective Optimization”. *Workshop on Artificial Life and Evolutionary Computation*, 2015.
- [18] Powell M.J.D. “The BOBYQA algorithm for bound constrained optimization without derivatives”. *Cambridge NA Report NA2009/06*, 2009.
- [19] Nagakura, S., Noguchi, S., Kaneda, K., Yamashita, H., Cingoski, V. "Automatic quadrilateral mesh generation for FEM using dynamic bubble system". *IEEE transactions on magnetics*, 2001, Vol. 37, No. 5, pp. 3522-3525.
- [20] Rzepka, S. "Automated FEM mesh optimization for nonlinear problems based on error estimation [IC packaging applications]". In *Proc. of IEEE Thermal and Mechanical Simulation and Experiments in Microelectronics and Microsystems*, 2004. EuroSimE 2004, pp. 201-209.
- [21] Xin, L., Zhaojie, Q., Xiaolong, C., Jiadong, X. "New Algorithm of Automatic FEM Mesh Generation for Electromagnetic Scattering Calculation". *Proc of IEEE 8th International Conference on Electronic Measurement and Instruments*, 2007. ICEMI'07. pp. 2-547.
- [22] Zhang, K., Jin, J.M., Geubelle, P.H. "A 3-D Interface-Enriched Generalized FEM for Electromagnetic Problems With Nonconformal Discretizations". *IEEE Transactions on Antennas and Propagation*, 2015, Vol. 63, No.12, pp. 5637-5649.

- [23] Rodriguez-Zermeno, V.M., Mijatovic, N., Traeholt, C., Zirngibl, T., Seiler, E., Abrahamsen, A.B., Pedersen, N.F., Sorensen, M.P. "Towards Faster FEM Simulation of Thin Film Superconductors: A Multiscale Approach". *IEEE Transactions on Applied Superconductivity*, 2011, Vol.21, No.3, pp. 3273-32.
- [24] Yang Y., Shen Q.L., Jin J.M., Wang Y.P., Qian W.J., Yuan D.W. "Rotational piezoelectric wind energy harvesting using impact-induced resonance". *Applied Physics Letters*, 2014, Vol. 105, No. 5.
- [25] Kluger J.M., Moon F.C., Rand, R.H. "Shape optimization of blunt body Vibro-wind galloping oscillator". *Journal of Fluids and Structures*, 2013, Vol. 40, p. 185-200.
- [26] Rezaei, N., Tabesh A., Dehghani R., Aghili A. "An Efficient Piezoelectric Windmill Topology for Energy Harvesting from Low Speed Air Flows", *IEEE Transactions on Industrial Electronics*, 2015, Vol. 62, No. 6, p. 3576-3583.
- [27] Viola F., Romano P., Miceli R., Acciari G. "On the harvesting of rainfall Energy by means of piezoelectric transducer". *Proc International Conference on Renewable Energy Research and Applications, ICRERA 2013*, pp. 1133-1138.
- [28] [www.Comsol.it/multiphysics](http://www.Comsol.it/multiphysics).
- [29] Bhuyan M.S., Othman M., Ali S.H.M., Majlis B.Y., Islam M.S. "Modeling and simulation of fluid interactions with bluff body for energy harvesting application". *Proc 10th IEEE International Conference on Semiconductor Electronics, ICSE 2012*, pp.123-127, 19-21.
- [30] Bhuyan M.S., Majlis B.Y.; Ali S.H.M.; Othman M.; Islam M.S. "Modelling and Finite Element Analysis of a micro energy harvester". *Proc. of International Conference on Multimedia, Signal Processing and Communication Technologies, IMPACT 2013*, pp.293-296.
- [31] Paxson, B., Wickenheiser, A.M. "Design considerations for small-scale wind energy harvesters driven by broadband vortex-induced vibrations". In *SPIE Smart Structures and Materials+ Nondestructive Evaluation and Health Monitoring International*. Society for Optics and Photonics, 2014.
- [32] Wilcox, D.C. "Turbulence Modeling for CFD", DCW Industries, 1998, Vol. 2, pp.103-217.
- [33] Pobering S., Schwesinger N. "Power Supply for Wireless Sensor Systems". *IEEE Sensors*, 2008, pp. 685-688.
- [34] Bhuyan M.S., Majlis B.Y., Othman M., Ali S.H.M., Islam S. "Finite element analysis of a fluid flow based micro energy harvester". *Research Journal of Applied Sciences*, 2013, Vol. 8, No. 10, pp. 507-515.
- [35] Hopcroft M.A., Nix W.D. Kenny T.W. "What is the Young's Modulus of Silicon?". *Journal of Microelectromechanical Systems*, 2010, Vol. 19, N. 2.

## ***4. Chapter 4***

### ***Applications of piezoelectric cantilever beams: Energy Harvesting and non-destructive diagnostics***

Chapter 4 illustrates the possible applications of piezoelectric harvester devices both in Energy Harvesting and Non-destructive testing fields.

An analysis of the possibility of exploiting the cantilever beams above described as energy harvester is described.

As for application in the Non-destructive testing field, a system useful for railway diagnostics is presented. The considered system consists of an axle box which undergoes the vibrations due to the irregularity of the railway track and transmits them to a piezoelectric cantilever beam. The transducer converts the input acceleration into electric potential useful to power a wireless sensor node. Therefore, the self-powered sensor node is able to ‘read’ information about the state of health of the axle box and to transmit it to an operational centre that provides an alert about defects or aberrations of the axle box in real time.

The chapter closes with an overview of the possible ongoing and future research of the case studies proposed.

#### 4.1. Introduction

A good definition of Energy Harvesting (EH) is provided by Heung Soo et al. They define it as the process interested in “capturing minute amounts of energy from one or more of the surrounding energy sources, accumulating them and storing them for later use” [1]. Erturk and Inman define the energy harvester as ‘the generator device undergoing vibrations due to a specific form of excitation’ [2]. Figure 4.1 shows a schematic representation of an EH process, implemented with piezoelectric energy harvesters.

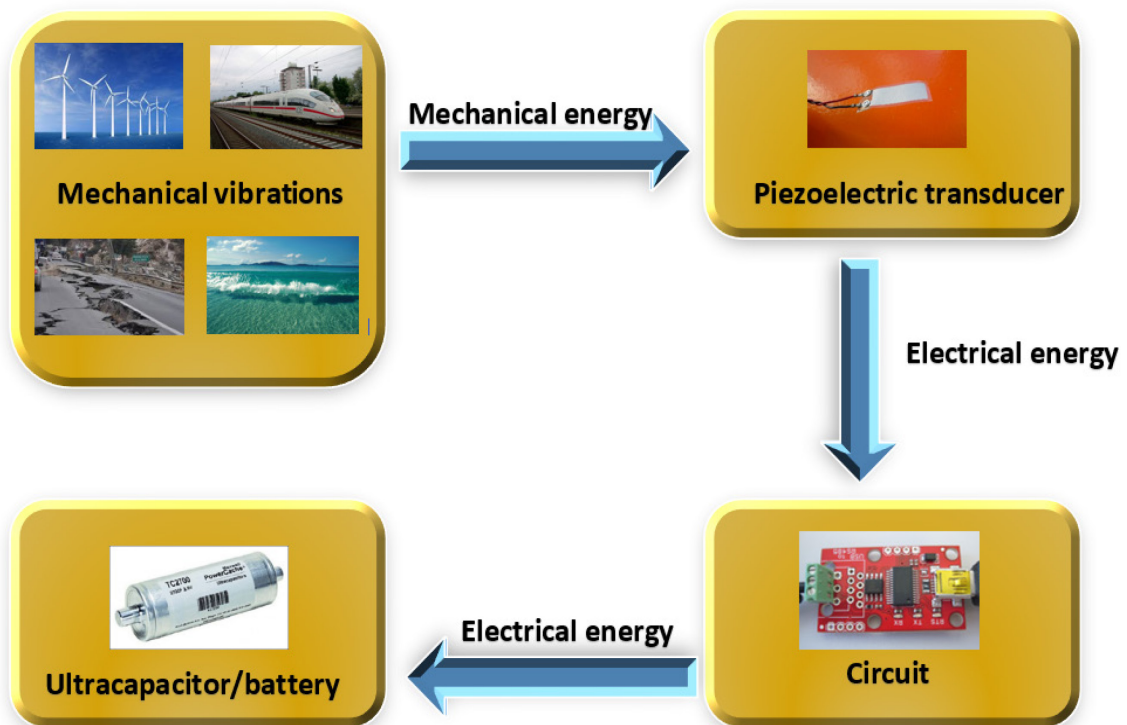


*Figure 4.1 – Schematic representation of the concept of a piezoelectric energy harvesting process.*

According to Mahadik and Sirohi, base-excited vibrations, flow induced vibrations and flutter due to wind flow are examples of the several possible ways to harvest piezoelectric energy [3]. The electromechanical response of a piezoelectric energy harvester to the energy it generates is dependent on the nature of the ambient energy [2] and the kind of stress applied.

In this dissertation, ‘minute amounts of energy’ have been captured from different ‘surrounding energy sources’ such as the flutter due to wind flow (sections 3.3 and 3.5) or water induced vibrations (section 3.6). Moreover, the following section 4.2 proposes an energy harvester useful to capture energy from the vibrations of a mechanical part of

a train. It is an example of a device which harvests energy produced by base-excited vibrations. In all the case studies considered there is a conversion of mechanical energy into electrical energy because of the use of piezoelectric transducers. These examples satisfy what the first two steps of an EH process require, represented by the first two yellow blocks of the diagram in Figure 4.1. But the energy generated has to be 'accumulated and stored for later use' to conclude the EH process. Electrical engineering provides appropriate solutions to close this process. A rectifier bridge and a smoothing capacitor can be used to convert the possible alternating output voltage into a stable rectified voltage. Then a DC–DC converter can be employed to regulate the output voltage of the rectifier, in order to maximize the power transfer to the storage device. In this way, if an existing structure can be modified using piezoelectric energy harvesters, the structure could be able to generate electrical energy from dynamic loads and to store it inside itself simultaneously. This concept provides a multifunctional structure that can find applications for remote wireless and low-powered systems, as long as the capacity of the modified structure is within an acceptable margin [2].

These kinds of devices can also find applications in the *Non-destructive techniques* (NDT) or *Non-destructive evaluation* (NDE) fields, as proposed in the following section 4.2. NDT and NDE refer to a wide range of techniques used by engineers to evaluate the properties of a material or the performance and the good state of health of objects or structures. These kinds of test must not damage or destroy the tested object. The detection of defects in solids is an essential part of quality control of engineering systems for their safe and successful use in practical situations [4-5]. The industrial inspection of engineering materials and products is aimed at the detection, localization and classification of defects in the most accurate and rapid way. In this field, NDE techniques are widely used and have an important role due to their non-invasive nature [6-11].

Several NDE test methods exist, such as radiography, ultrasonic inspection, magnetic particle inspection, liquid penetrating inspection, thermography, electrical and magnetic methods, and visual-optical inspection, but they often require expensive equipment and invasive installations or a long time to be implemented. Small inexpensive devices are presented in this chapter. These devices are able to conjugate an EH with NDE [12-13]. The piezoelectric cantilever beams analysed in the previous chapters can find several

appropriate applications, those related to the EH and NDE fields are analysed in this chapter.

## 4.2. Applications in NDE

Real time diagnostic and structural monitoring operations are not simple actions for freight trains, due to the absence of on board electrification. The sophisticated sensor systems, already installed on passenger trains, have never been applied to freight trains. They only have sensors available for a few controls along the rail. The opening of the borders between European nations and the free travelling of trains have unfortunately brought a reduction in the level of available information about vehicles, in particular about their maintenance and their safety. Thus, real-time monitoring for diagnostics and prevention is assuming a growing importance.

In the last decade, research efforts into low-power sensors and integrated wireless transmission modules have made more feasible the generation of the electric power required by simple diagnostic systems. They use devices set directly on board railways wagons [14-15]. From an operational point of view, it also appears possible to use these devices to monitor relevant diagnostic parameters. Piezoelectric harvester devices have found promising applications in this context [16-18]. The following sections describe a proposal for the design of a system consisting of an axle box, a sensor node and a piezoelectric cantilever beam.

### 4.2.1. *The axle box*

A good definition of the ‘axle box’ is provided by [19]: it is “the housing attaching the axle end to the bogie, which contains the bearing allowing the axle to rotate”. The axle box is the seat of the bearing of wheelset axles and is connected to the primary suspension: it sustains the weight of the carriage, downloading it through the bearings on the same axle pins. It is depicted in the red circle in Figure 4.2.



*Figure 4.2- Axle box on a rail vehicle*

The design of the system prescribes an axle box transferring its acceleration to a piezoelectric cantilever beam. Subsequently the transducer converts the acceleration into electric potential, useful to power a wireless sensor node.

Studies into the dynamics of trains have shown that the accelerations of the axle box are high because of the irregularities of the railway line, as explained in Table 2.D of the standard UNI EN 13749 [20]. So the axle box is one of the safety-critical subsystems in railway vehicles [21] and one of the most stressed components of the train wheelset. For this reason, the axle box has been chosen as the optimal place to install a piezoelectric harvester. Moreover, analysis of the system vibration frequencies enables the self-powered sensor node to provide information about the state of health of the axle box. When opportunely transmitted to an operational centre, this information can provide an alert in real time about defects or aberrations of the axle box. Thus, the described system achieves EH and diagnostic goals simultaneously.

With this aim, the axle box-cantilever system has been simulated. The studies were conducted in stationary and time-dependent conditions. The simulator provided a random input acceleration, which was modelled as a normal distribution having a prefixed mean value and standard deviation [22].

The axle box was simulated as a cylinder with a radius of 150mm and a height of 150mm. It is made of structural steel, the same material used for the lower surface of the

cantilever beams. Its properties are described in the following Table XXIV in section 4.2.3.

#### 4.2.2. The sensor node

The *sensor node* is an electronic device able to capture and store information with the purpose of processing and transmitting it via radio. It represents a promising technology in the structural monitoring field, because of the distribution of several single units able to make measurements and to communicate them to an external operative centre. Therefore, the self-powered sensor node can ‘read’ information about the state of health of the axle box, analysing the frequency of vibrations of the system. So, it is able to transmit this information to an operative centre, which opportunely provides an alert about defects or aberrations of the axle box in real time. The powering of a sensor node, with a piezoelectric energy harvester, creates an energetically autonomous system.

#### 4.2.3. The energy harvester

An energy harvester device, with a cantilever beam structure, was designed in order to generate electric power from the vibrations acting on the axles and on the axle boxes of the railway vehicle during its service. Figure 4.3 shows the structure, not to scale, of the considered device. It is composed of one layer of structural steel, which acts both as a support for the piezoelectric material and as ground terminal. The piezoelectric layer is made of Lead Zirconate Titanate PZT-8.

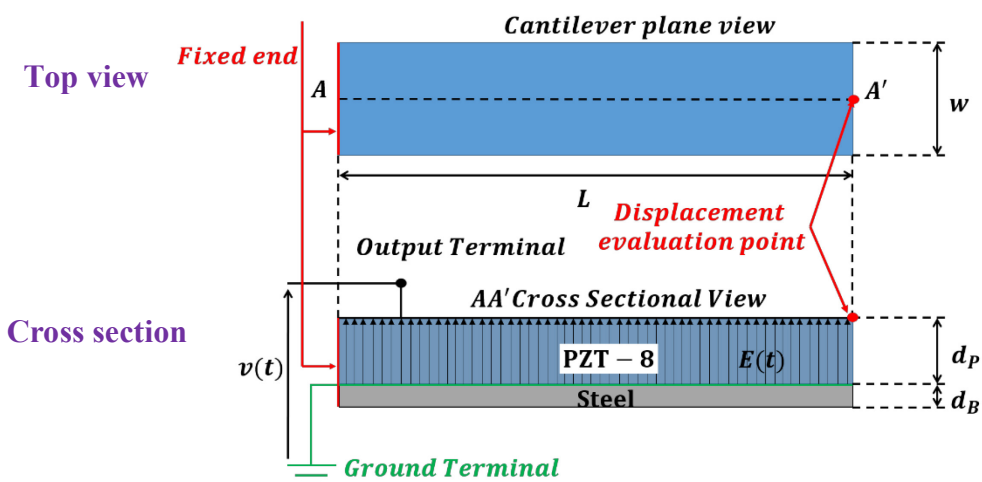


Figure 4.3 - Plane and cross sectional view of the device (not to scale).

The locked end of the cantilever beam is supposed to be connected to the axle box, as

schematically represented in Figure 4.4. The beam is embedded 5mm into the axle box .

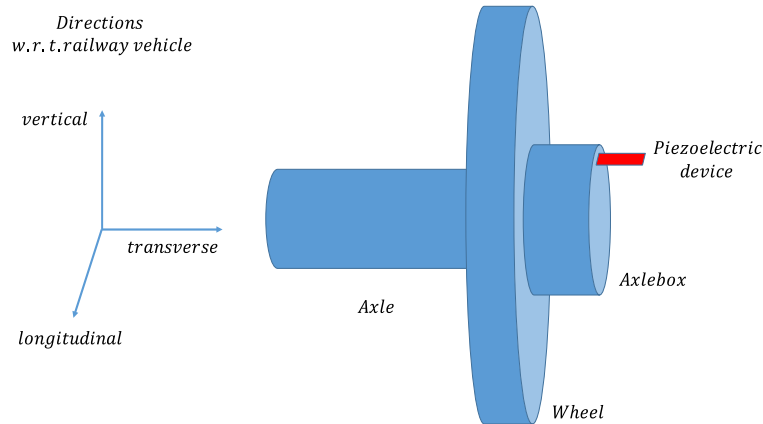


Figure 4.4 - Schematic representation of the system.

An in-service railway vehicle is subjected to vibrations and shocks, which are mostly due to the nature of railway tracks and the operational environment. The piezoelectric device is meant to harvest electrical power from these vibrations. The geometric and constitutive parameters of the device shown in Figure 4.3 are reported in Tables XXIII and XXIV where the matrix  $c^E$ ,  $e$  and  $\epsilon^S$  are the piezoelectric matrices of PZT-8, expressed in (4.1-4.3).

TABLE XXIII - GEOMETRIC PARAMETERS OF THE CANTILEVER BEAM.

L [mm]	w [mm]	$d_p$ [mm]	$d_B$ [mm]
50	10	0.15	0.125

In Table XXIII,  $L$  is the length of the beam,  $w$  is its width,  $d_p$  is the thickness of the piezoelectric layer and  $d_B$  the thickness of the structural steel layer.

TABLE XXIV - CONSTITUTIVE PARAMETERS OF THE CANTILEVER BEAM.

Material	Density $\rho$ [Kg/m <sup>3</sup> ]	Young's modulus [Pa]	Relative permittivity
Structural steel	7850	$200 \cdot 10^9$	1
PZT-8	7600	$c^E$	$\epsilon^S$

$$c^E = \begin{bmatrix} 1.4687e^{11} & 8.1087e^{10} & 8.10537e^{10} & 0 & 0 & 0 \\ 8.1087e^{10} & 1.4687e^{10} & 8.10537e^{10} & 0 & 0 & 0 \\ 8.10537e^{10} & 8.10537e^{10} & 1.31712e^{11} & 0 & 0 & 0 \\ 0 & 0 & 0 & 3.1348e^{10} & 0 & 0 \\ 0 & 0 & 0 & 0 & 3.1348e^{10} & 0 \\ 0 & 0 & 0 & 0 & 0 & 3.28947e^{10} \end{bmatrix} [\text{Pa}] \quad (4.1)$$

$$e = \begin{bmatrix} 0 & 0 & 0 & 0 & 10.3448 & 0 \\ 0 & 0 & 0 & 10.3448 & 0 & 0 \\ -3.87538 & -3.87538 & 13.9108 & 0 & 0 & 0 \end{bmatrix} \left[ \frac{\text{C}}{\text{m}^2} \right] \quad (4.2)$$

$$\varepsilon^S = \begin{bmatrix} 904.4 & 0 & 0 \\ 0 & 904.4 & 0 \\ 0 & 0 & 561.6 \end{bmatrix} \quad (4.3)$$

#### 4.2.4. Mathematical model

The mathematical model which describes the behaviour of the device is expressed by the following Equations (4.4-4.6):

$$\rho \ddot{u} = \nabla \cdot T + F_V \quad (4.4)$$

$$\nabla \cdot D = \rho_V \quad (4.5)$$

$$S = \frac{1}{2} (\nabla u + (\nabla u)^t) \quad (4.6)$$

where  $u$  is the displacement vector,  $D$  is the electric displacement vector,  $S$  is the strain tensor,  $T$  is the stress tensor,  $F_V$  represents the input mechanical action,  $\rho_V$  is the electric charge volumetric density and  $t$  denotes the transpose matrix. The last equation of the mathematical model is equation (1.3). The model proposed is only valid for small displacements and rotations.

#### 4.2.5. Stationary analysis

The first analysis was carried out on an axle box without defects in a steady-state situation. In order to simulate the irregularity of the railway line, it is necessary to apply a force to the axle box. Based on previous studies, a force directed and oriented on the z-axis and with an intensity of 2000 N was chosen (Figure 4.5). The simulation results show that the most stressed region in the axle box is the red line A shown in Figure 4.5. Based on these results, the configuration in Figure 4.4 was chosen.

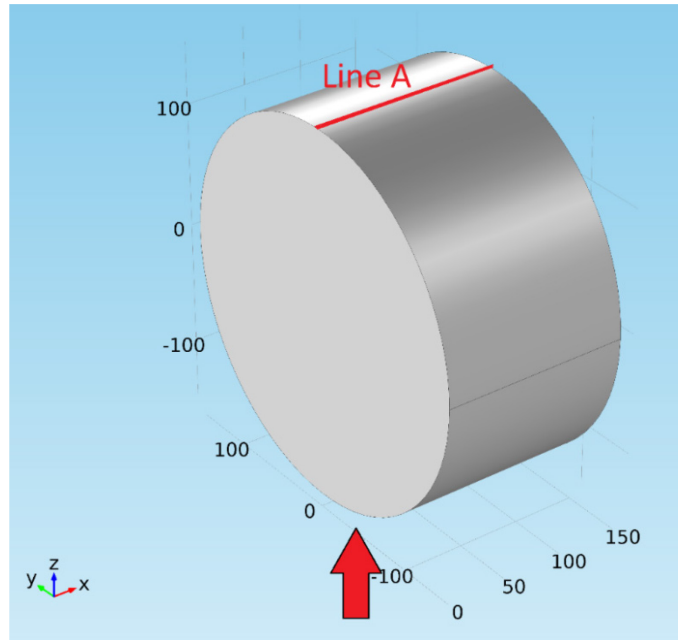


*Figure 4.5- Measuring line A and the z-axis force (all dimensions are expressed in millimetres).*

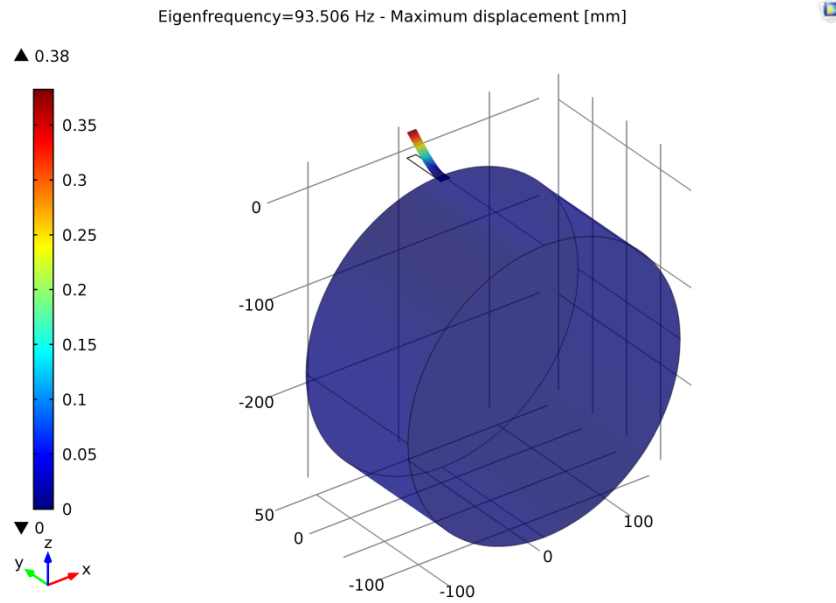
#### 4.2.6. Eigenfrequency analysis

*Modal analysis* is the study of the dynamic behaviour of structures, locked or free to move, under vibrational excitation. This analysis was used to evaluate the natural frequencies and normal modes of the considered system, in this section. Comsol Multiphysics allows this kind of study for a number of eigenfrequencies decided by the user. Therefore, it is possible to observe the new configuration that the system reaches while vibrating, at each different frequency.

To apply modal analysis to the axle-box-cantilever system some boundary conditions are needed. Mechanical boundary conditions require a fixed boundary constraint at the end of the cantilever where it is connected to the axle box (Figure 4.4). All the remaining portions of the cantilever are free to move. The back surface of the axle box is considered locked while all the other surfaces are free to move if they undergo an input acceleration.

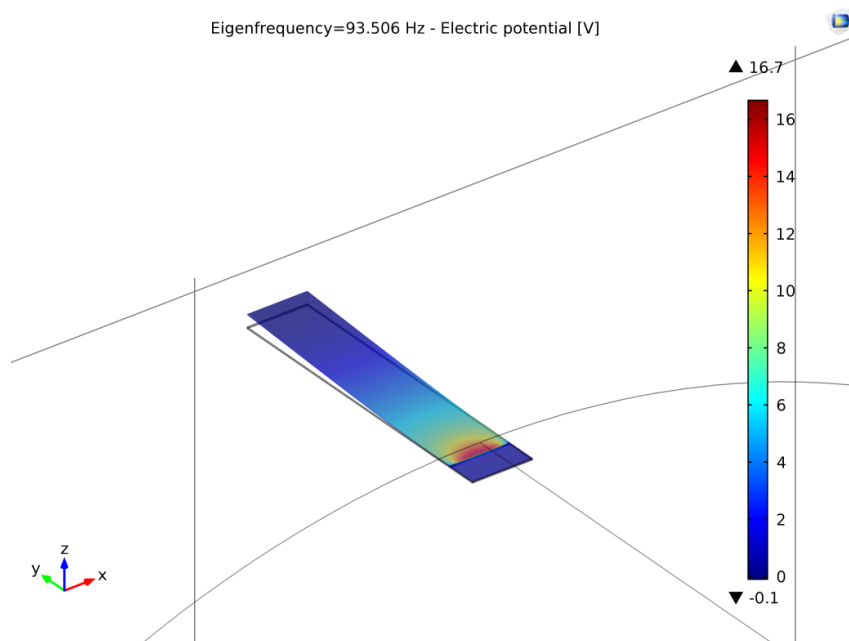
Electrical boundary conditions require all the surfaces of the cantilever to be at ground, except for the upper one, which initially has zero charge: this surface will show a charge density varying as a function of the beam deformation.

Figure 4.6 shows the deformed shapes of the cantilever beam vibrating at an eigenfrequency of 93.506Hz. This value belongs to the range of frequencies usually measured on the axle box [22].



*Figure 4.6 - Maximum displacement of the cantilever.*

Figure 4.7 shows the electric potential generated on the upper surface of the cantilever due to the endured deformation.



*Figure 4.7 - Electric potential generated on the upper surface of the cantilever beam.*

Figure 4.7 shows that the maximum value for the electric potential generated is 16.7V, while the minimum is -0.1V, with an RMS value of 4.04V, evaluated on the upper

piezoelectric surface.

As is well known, when the system vibrates at its resonance frequency the maximum displacement (Figure 4.8) and, consequently, the maximum electric potential (Figure 4.9) are generated.

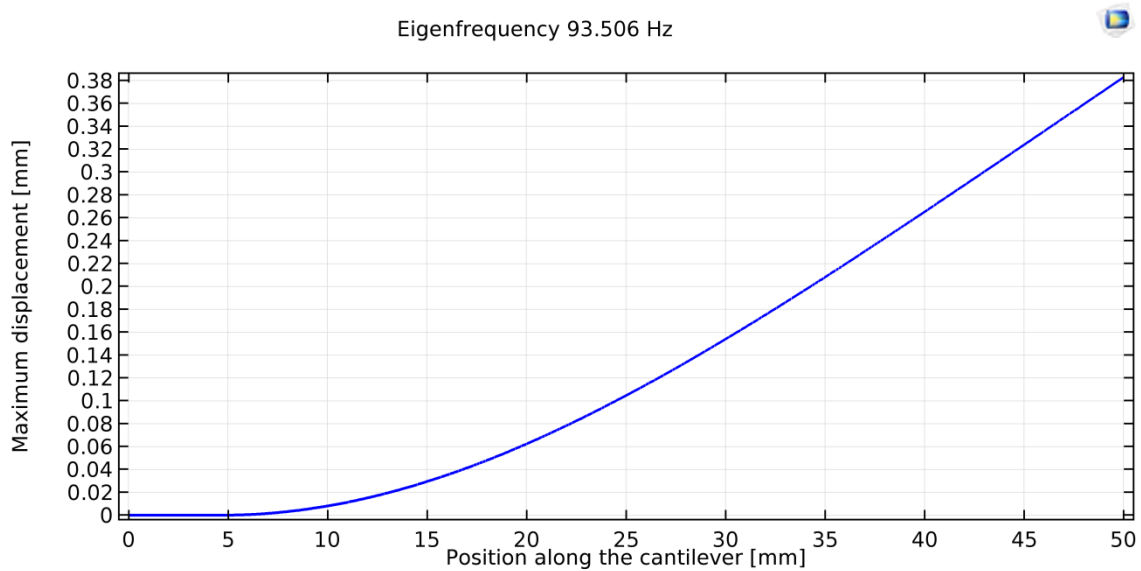


**Figure 4.8 – Displacement of cantilever beam.**

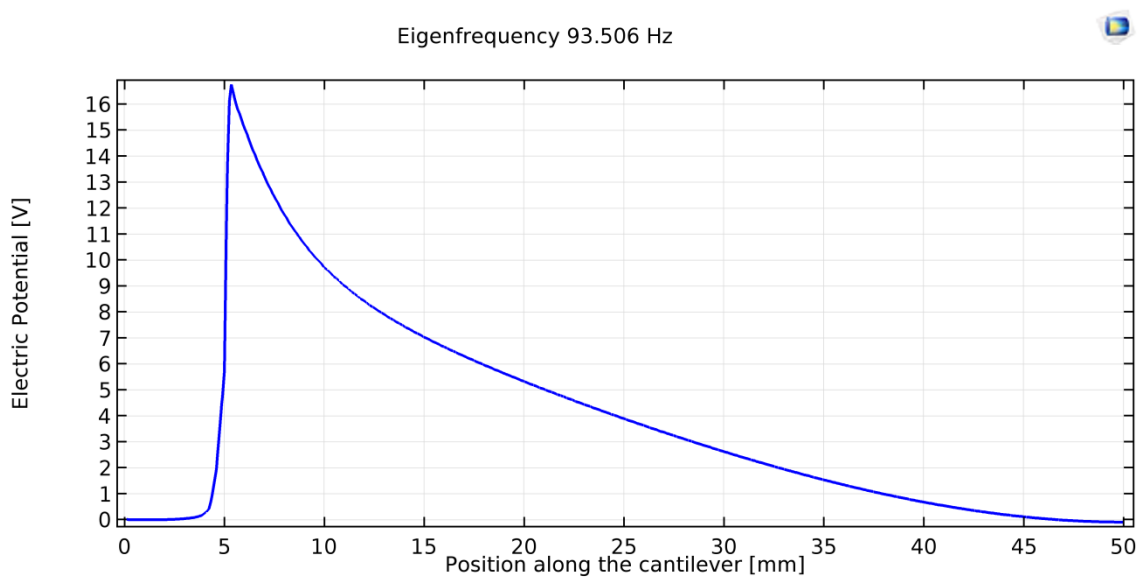


**Figure 4.9 - Electric Potential measured on the cantilever beam**

Figure 4.9 shows that the electric potential is null or very low for the portion of the cantilever embedded in the axle box (the first 5mm of its length) while it reaches the maximum value in the free portion very close to the axle box where it undergoes the

maximum stress.

#### 4.2.7. Time dependent analysis

In this kind of analysis, the electrical boundary conditions are different from those applied in the section 4.2.6. A terminal node was applied to the upper face of the PZT layer. It provides a boundary condition for connection to external circuits or with a specified voltage or charge. By specifying zero charge, a floating potential condition is obtained [23]. When the terminal node is present, the surface where electric potential is generated is equipotential. Moreover, a ground node was attached to the interface surface between the PZT and the steel domain, as shown in Figure 4.3. The terminal and ground nodes correspond to the output voltage electrodes, their thickness can be ignored. The zero charge condition was applied to all the remaining boundaries.

The mechanical boundary conditions were the same as those in section 4.2.6.

As previously mentioned, the role of the piezoelectric transducer is to harvest energy from the vibrations induced on the axle box during the normal service of the railway vehicle. The result of a study into the values of acceleration levels on a railway vehicle during its service is reported in [22]. In order to detect these accelerations, three different measuring points were selected: the axle, the frame (bogie), and the body. The results of the investigation showed that the highest accelerations were detected on the axle. Measured signals can be represented by normal distributions, characterized by the values reported in Table XXV, where the directions are those depicted in Figure 4.4.

TABLE XXV - AXLE ACCELERATIONS LEVELS.

Direction	Average level RMS [m/s <sup>2</sup> ]	Standard deviation
<b>Vertical</b>	24	14
<b>Transverse</b>	20	14
<b>Longitudinal</b>	11	6

The vertical acceleration reported in Table XXV can be reasonably assumed to be completely transferred to the axle box and, subsequently, to the boundary of the cantilever beam. In the time domain, its signal is represented in Figure 4.10.

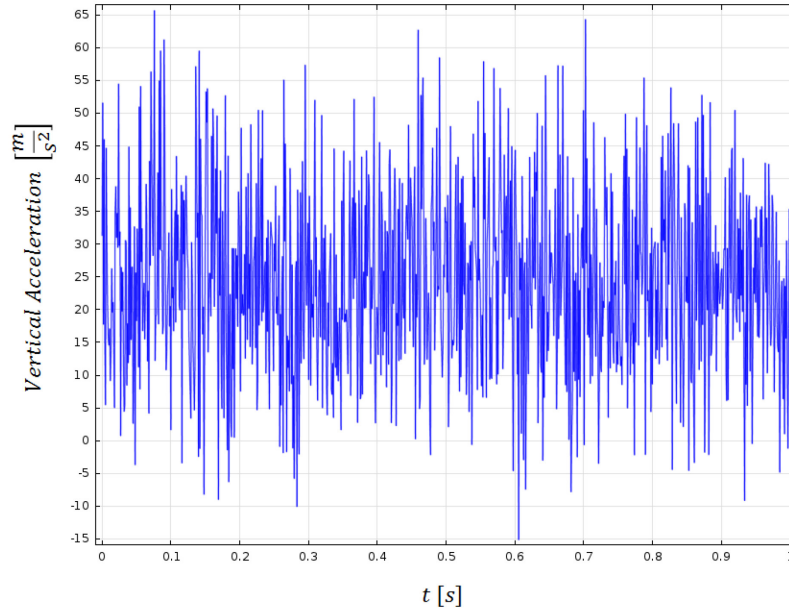


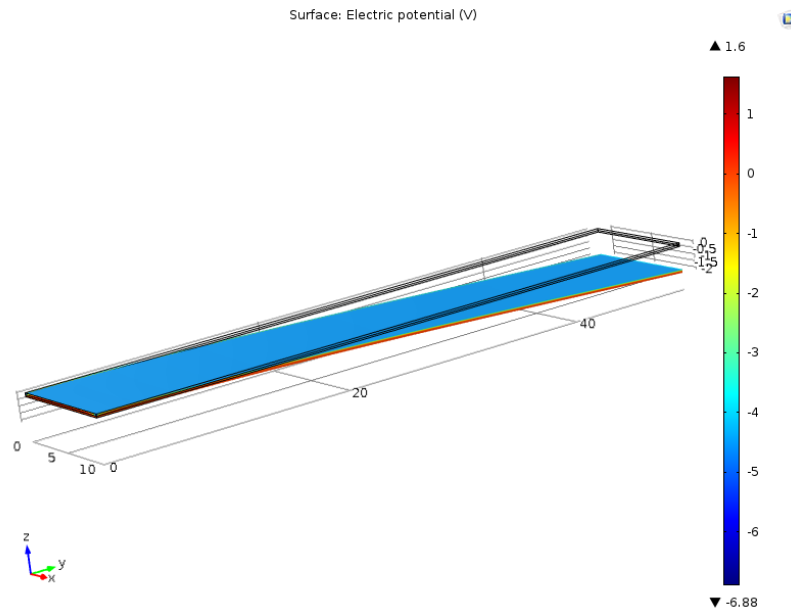
**Figure 4.10 - Axle box vertical acceleration in the time domain**

In order to simulate the response of the piezoelectric device to such an input, a boundary load was applied to the fixed surface of the cantilever. It was a force per unit area, directed along the vertical direction in Figure 4.4 and can be expressed as follows:

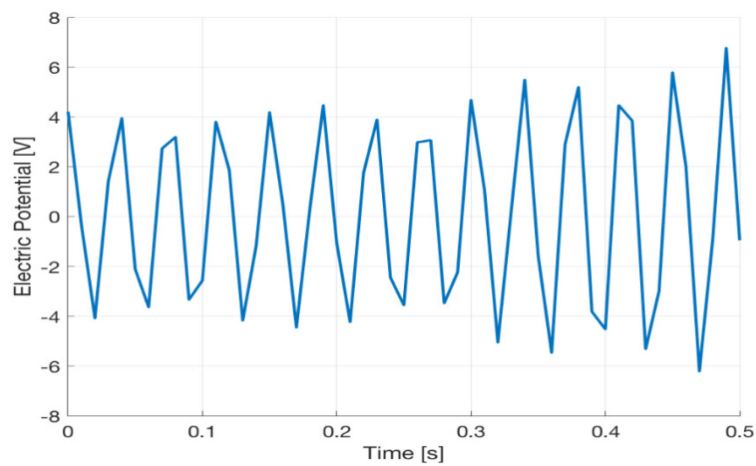
$$F = -\rho a(t) L 10^{-3} \left[ \frac{N}{m^2} \right] \quad (4.7)$$

where  $a(t)$  is the signal represented in Figure 4.10 and  $\rho$  is the material volumetric mass density, which Comsol Multiphysics automatically assigns to the appropriate domain. Parameter  $L$  is the length of the cantilever, which is reported in Table XXIII.

The choice to transfer the axle box acceleration to the fixed boundary of the cantilever was made in order to overcome difficulties related to multi-scale meshing. These problems are due to the need to represent the whole system which consists of two very different objects in terms of dimensions, namely the axle box and the cantilever beam. A time dependent study was carried out. The simulating time window was 0.5s long, with a step of 0.01s. Figure 4.11 shows an example of a three-dimensional plot of the electric potential distribution along the deformed cantilever, at time  $t=0.4$  s, while Figure 4.12 shows the open circuit output voltage, in time domain.

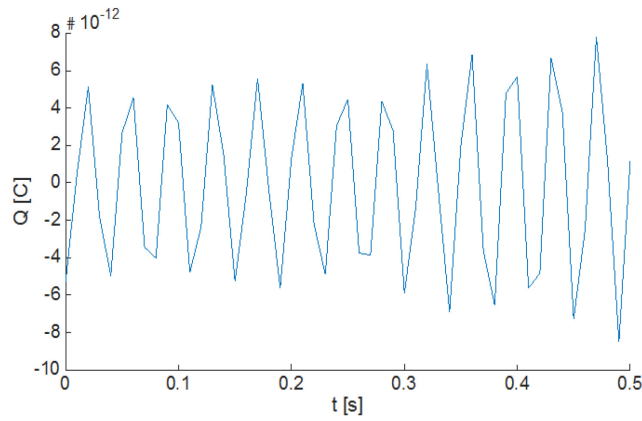


**Figure 4.11 - 3D plot of a cantilever and electric potential distribution at time 0.4 s. Dimensions are in millimetres.**



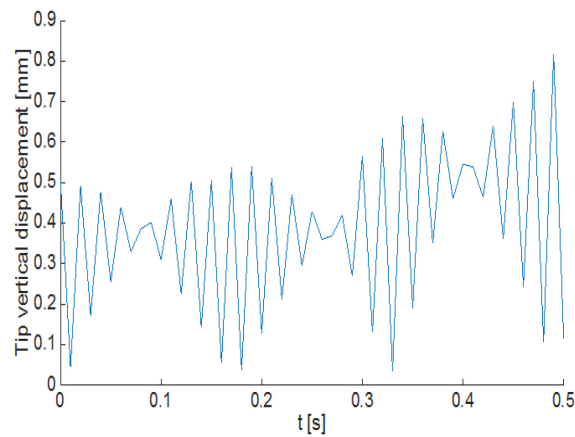
**Figure 4.12 - Open circuit voltage generated.**

Figure 4.13 shows the electric charge collected on the upper face of the piezoelectric layer, in the time domain.



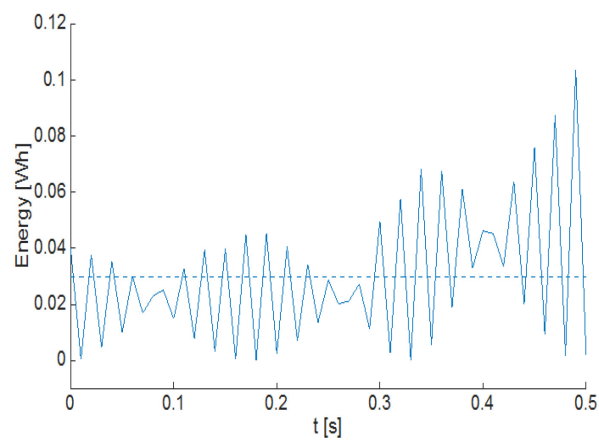
**Figure 4.13 - Electric charge on the upper surface of the piezoelectric material.**

Figure 4.14 shows a plot of the vertical displacement of an evaluation point (point A' shown in Figure 4.3) located at the free end of the cantilever.



**Figure 4.14 - Cantilever tip vertical displacement**

Figure 4.15 shows the absolute value of the electrical potential energy as a function of time. The dashed line represents the mean value.



**Figure 4.15 - Electrical potential energy and its mean value.**

These results are very promising because they clearly show that the energy generated by the piezoelectric cantilever beam in the configuration under study is enough to power a wireless sensor node for railway vehicles.

#### 4.2.8. Study in the presence of defects

In order to make a non-destructive test and diagnosis of the state of health of the axle box, an eigenfrequency study was carried out. The system considered was the same as that in section 4.2.6 with the same boundary conditions and kind of study. The results obtained with the damaged axle box were compared with those in section 4.2.6, obtained studying the intact axle box.

Macroscopic defects such as holes inside the axle box were simulated by removing material from the body of the device. These kinds of defect are not externally visible as shown in Figures 4.16 and 4.17 and non-destructive analysis can be useful to detect them and promptly replace the axle box before catastrophic failure occurs.

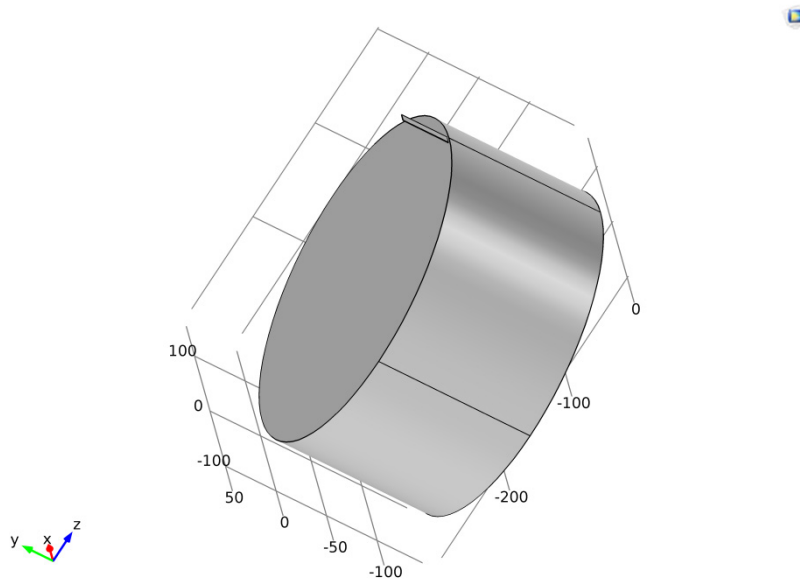


**Figure 4.16 - The outside of the damaged axle box (all dimensions are expressed in millimetres).**

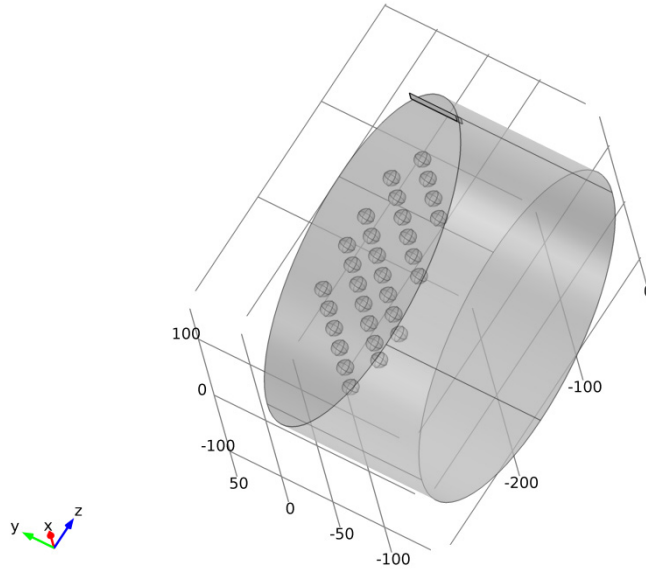


*Figure 4.17 - The inside of the damaged axle box shown using transparency (all dimensions are expressed in millimetres).*

30 spherical holes with the same radius were created inside the axle box. Simulations were then carried out increasing the holes radius from 0mm (undamaged axle box) to 15mm.. The first eight eigenfrequencies of the system were detected, for each radius considered. Moreover, the maximum electric potential values generated by the cantilever at the first eigenfrequency are reported in Table XXVI.

TABLE XXVI - COMPARISON OF NATURAL FREQUENCIES OF INTACT AND DAMAGED AXLE BOX (MULTIPLE HOLES).

<b>Holes' radius [mm]</b>	<b>First natural frequency [Hz]</b>	<b>Eighth natural frequency [Hz]</b>	<b>Max electric potential [V]</b>
0	93.506	4315.4	16.7
0.5	93.504	4316	19.6
1	93.504	4315.8	19.8
1.5	93.504	4316	19.6
3	93.506	4316.8	22
5	93.504	4320.5	23.2
7	93.505	4323.3	22.4
10	93.508	4323.3	21.2
15	93.508	4323.4	19.6

Analysis of the data in Table XXVI highlights that the first eigenfrequency can be

considered as a constant, as also shown in Figure 4.18. This is the first natural frequency of the cantilever as if it resonates without a connection to the axle box. It is constant because the cantilever is not influenced by the damage on the axle box.

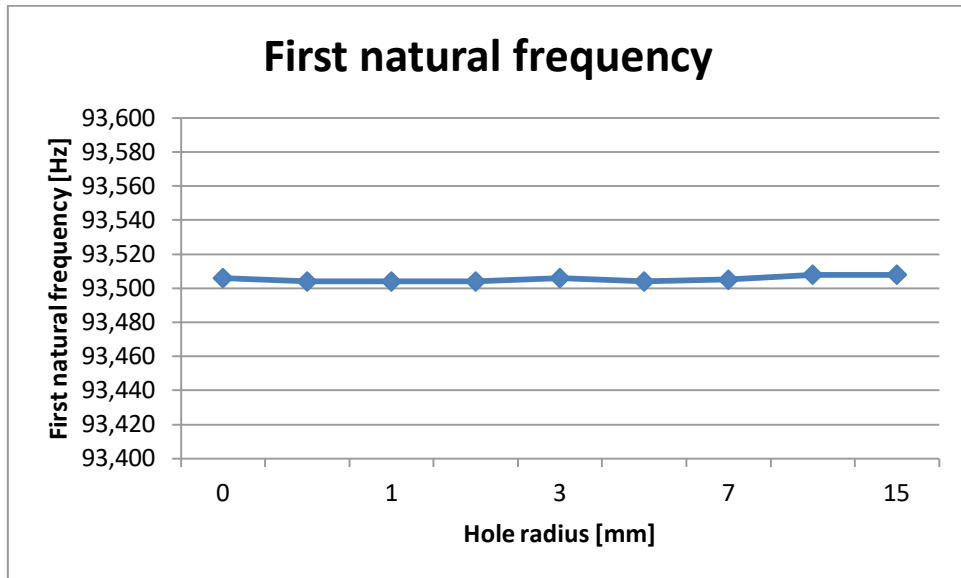


Figure 4.18 - First eigenfrequency of the system as a function of hole radius.

The eighth eigenfrequency increases with the increase in the hole radius and stabilises for the biggest radii, as shown in Figure 4.19. It corresponds to the natural frequency of the axle box as if it resonates without a connection to the cantilever beam. Thus, its value changes as a function of the damage.

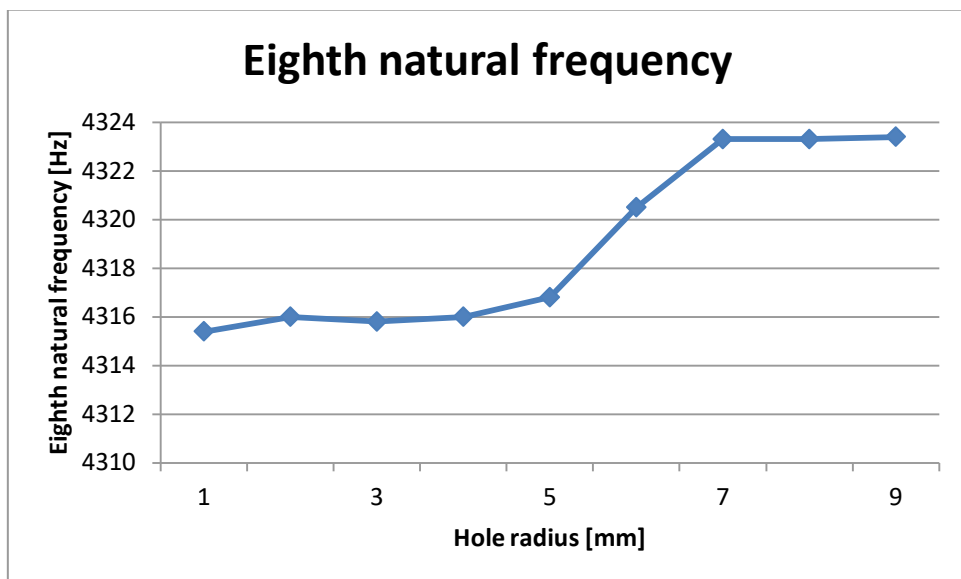
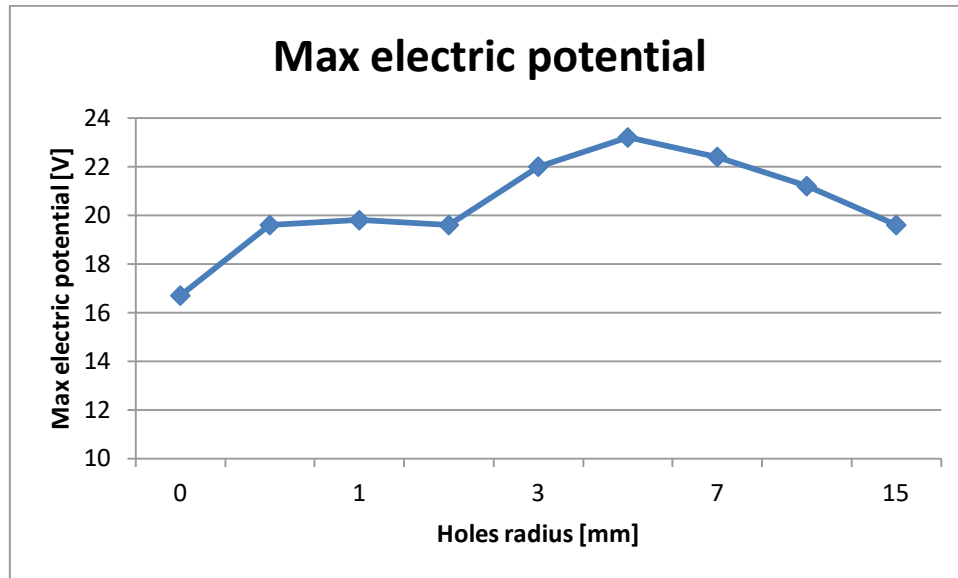


Figure 4.19 - Eighth eigenfrequency of the system as a function of hole radius.

The last column of Table XXVI shows the maximum values of the electric potential generated by the transducer. These values increase when the axle box is damaged, as shown in Figure 4.20.



*Figure 4.20 - Maximum electric potential generated by the cantilever beam.*

The electric potential generated is only influenced by the amplitude of the vibrations and not by their frequency, so it follows a different trend from that of the natural frequencies. A coupled analysis of the graphics in Figures 4.19 and 4.20 suggests that for smaller radii of the holes the natural frequency of the axle box stays fairly constant but the electric potential generated increases, while for bigger radii the natural frequency of the axle box increases.

Figures 4.21-4.24 depict the first eigenfrequency and the electric potential generated in two situations with different holes radii, 1mm and 7mm, respectively. Figures 4.21 and 4.23 show the whole system while Figures 4.22 and 4.24 each show a detailed image of the transducer.

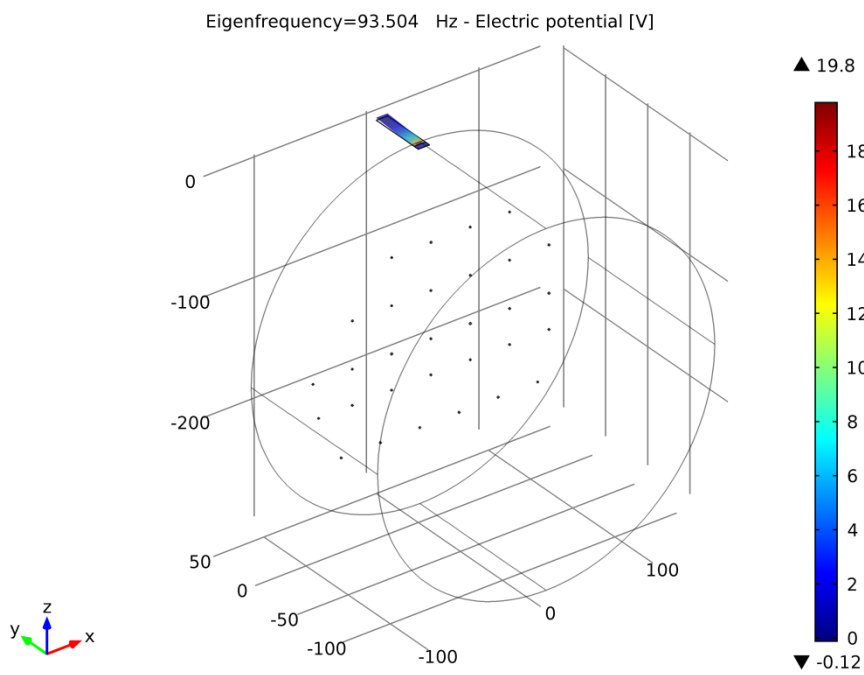


**Figure 4.21 - First eigenfrequency of the axle box with 1mm hole radius (all dimensions are expressed in millimetres).**

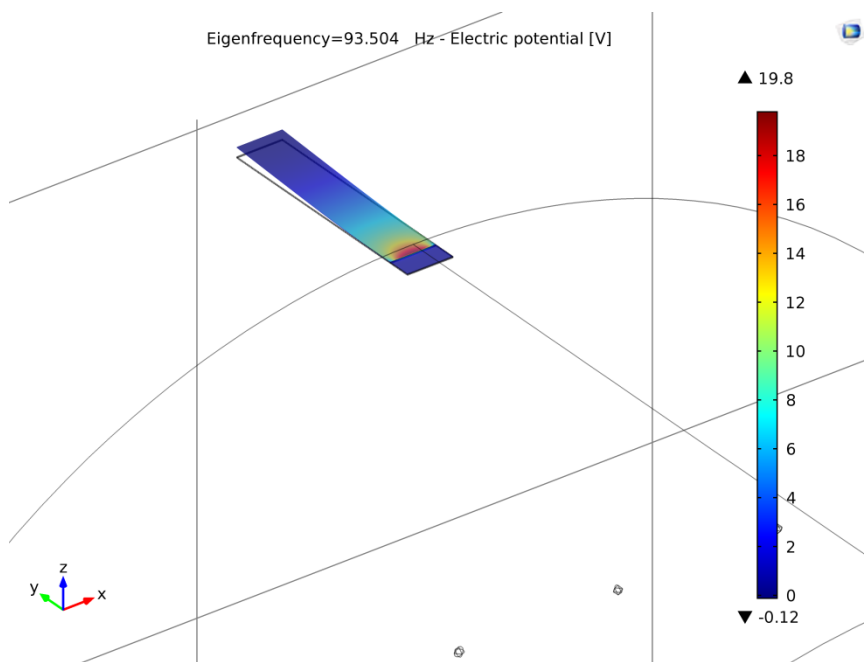


**Figure 4.22 - First eigenfrequency of the axle box with 1mm hole radius -A detail of the cantilever beam.**

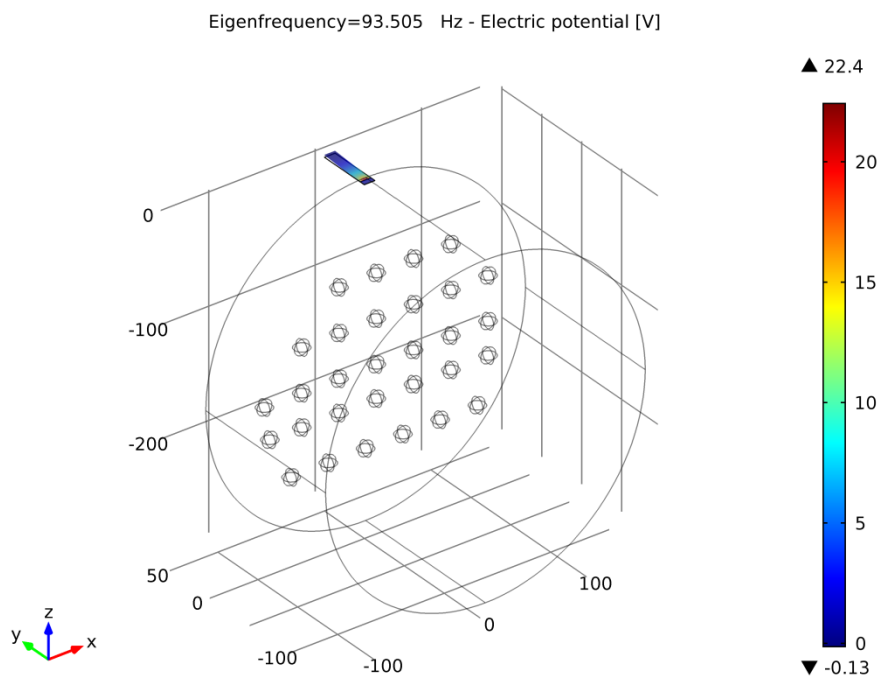


**Figure 4.23 - First eigenfrequency of the axle box with 7mm hole radius (all dimensions are expressed in millimetres).**

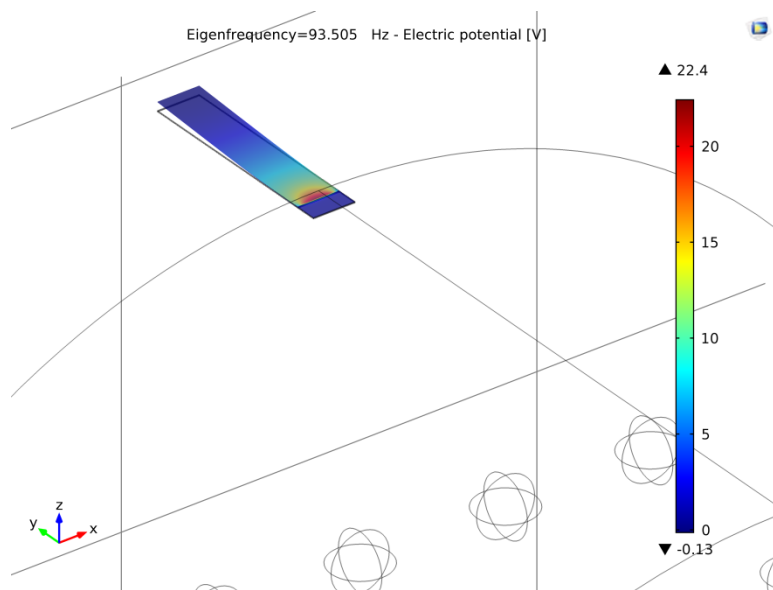
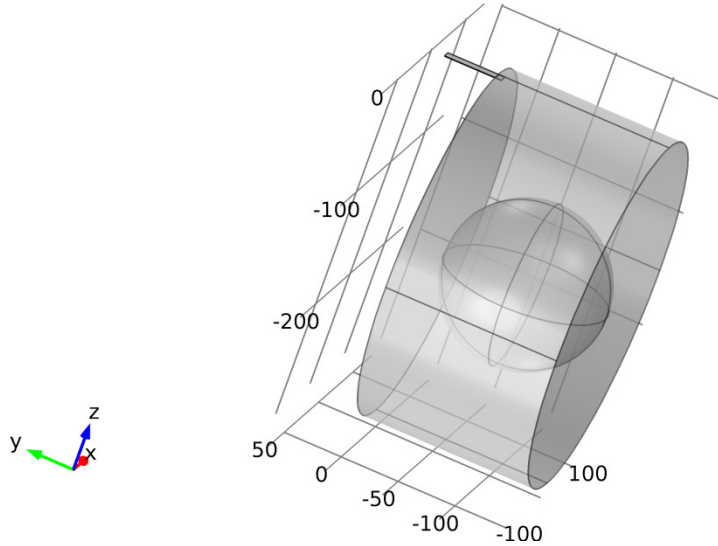


**Figure 4.24 - First eigenfrequency of the axle box with 7mm hole radius -A detail of the cantilever beam.**

#### 4.2.9. Study in the presence of a different defect

This section deals with a simulation of the same system as that in section 4.2.6 and

4.2.8, but introducing a different defect. The axle box only had a single hole in its centre and simulations were carried out increasing the hole radius from 0mm (undamaged axle box) to 70mm.



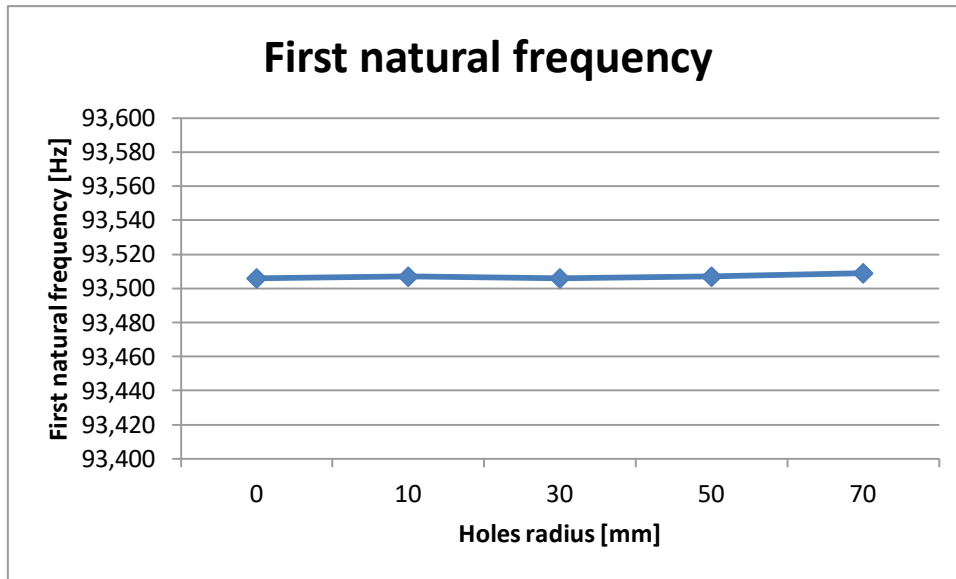
*Figure 4.25 - The inside of the damaged axle box shown using transparency (all dimensions are expressed in millimetres).*

Table XXVII shows the same variables as Table XXVI but specific for this new defect.

TABLE XXVII - COMPARISON OF NATURAL FREQUENCIES OF INTACT AND DAMAGED AXLE BOX (SINGLE HOLE).

Hole radius [mm]	First natural frequency [Hz]	Eighth natural frequency [Hz]	Max electric potential [V]
0	93.506	4315.4	16.7
10	93.507	4313.5	16.8
30	93.506	4271.8	16.5
50	93.507	4138.6	16.6
70	93.509	3925.5	16.9

The first eigenfrequency can be considered as a constant, as in the case studied in section 4.2.8. It is shown in Figure 4.26.



*Figure 4.26- First eigenfrequency of the system as a function of hole radius.*

The eighth eigenfrequency decreases in this case, as shown in Figure 4.27.

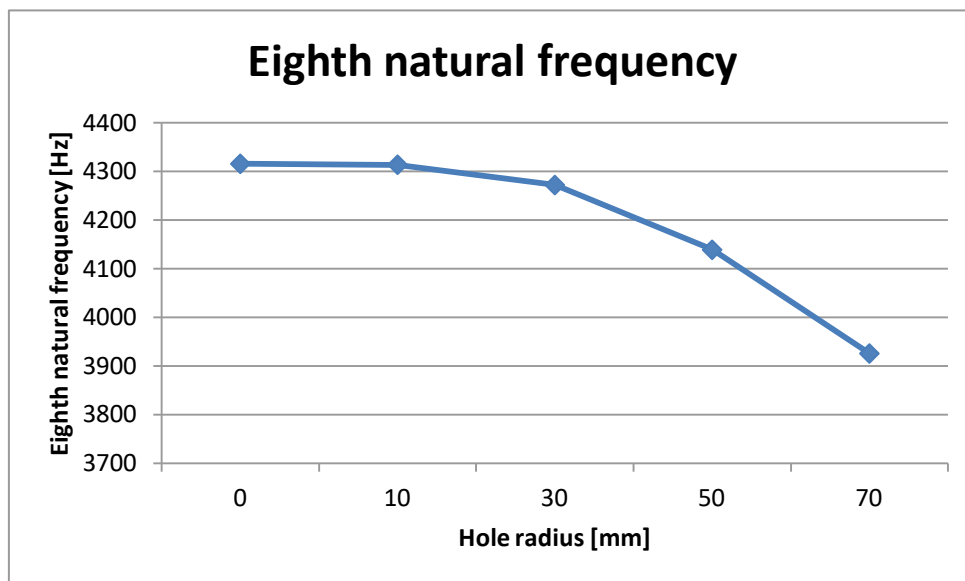


*Figure 4.27 - Eighth eigenfrequency of the system as a function of hole radius.*

The variations of electric potential generated are not significant in this case.

Figures 4.28 and 4.29 show the electric potential generated at the first eigenfrequency for a hole with a maximum radius of 70mm.

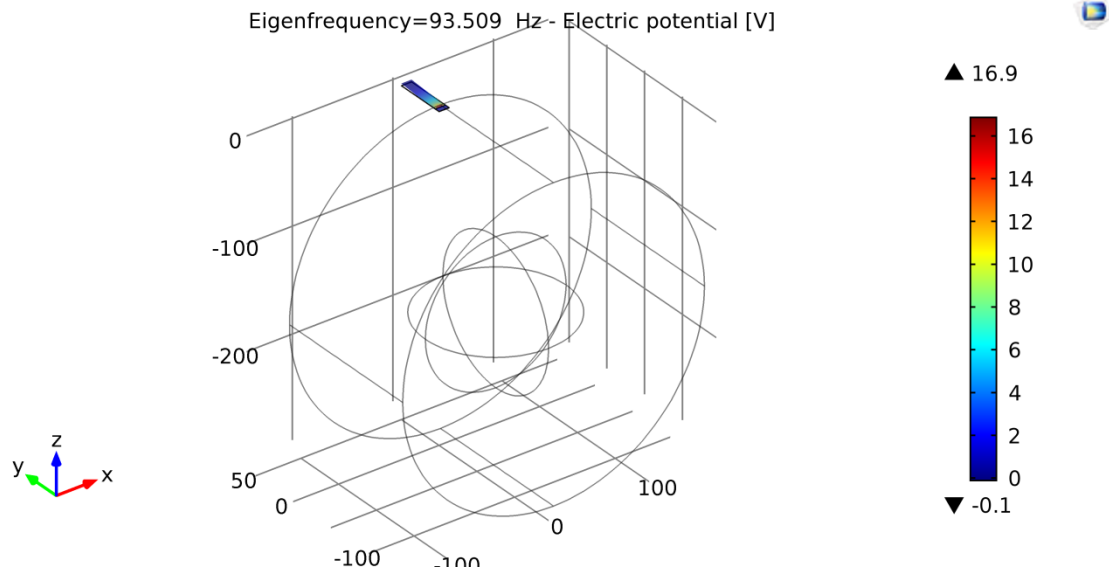


**Figure 4.28 - First eigenfrequency of the axle box with 70mm hole radius. All dimensions are in millimetres.**

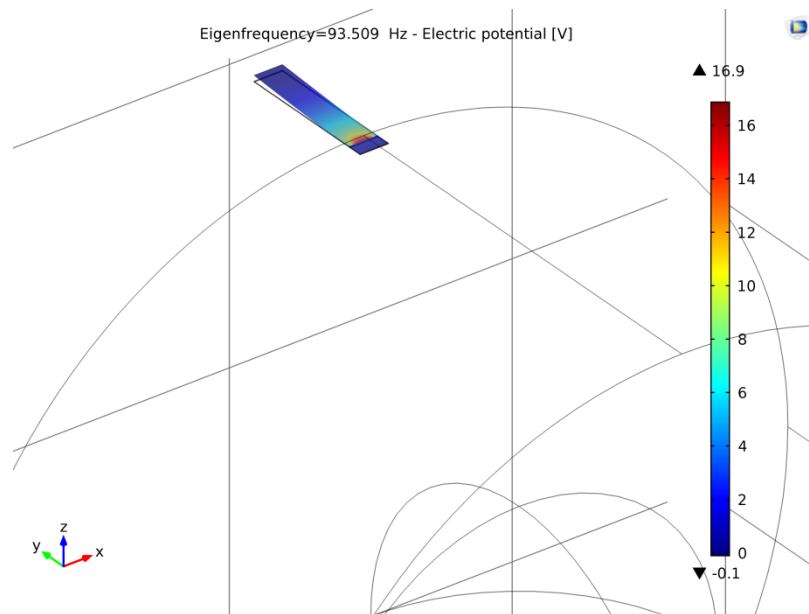


**Figure 4.29 - First eigenfrequency of the axle box with a 70mm hole radius -A detail of the cantilever beam.**

The results in sections 4.2.8 and 4.2.9 show how a different kind of defect changes the values of the basic variables of the system, such as the natural frequency of the axle box or the electric potential generated. Thus, an appropriate and coupled analysis of these variables and well-timed monitoring enables non-destructive diagnosis of the state of health of the axle box, in real time, while the train is in service.

#### 4.3. Ongoing and future research

The case studies analysed in chapter 3 and in section 4.2 offer several inspirations for future research.

The simulations proposed in sections 3.2.4, 3.2.5, 3.3.4 and 3.3.5 were carried out on limited parameters ranges. An in-depth study changing the piezoelectric cantilever beam parameters in a much wider range could be carried out, with the aim of finding simpler analytical expressions describing the behaviour of the transducers as a function of their parameters and of the inputs. This could foster the development of theoretical hypothesis which could in turn be used to refine the model. Additionally, comparison studies with isotropic materials could be carried out.

An automatic procedure could be realised or an optimization process could be applied to the mesh streamlining proposed in section 3.4.3. As already explained in that section, the reduction in the number of the mesh nodes was carried out manually and it was stopped when the deviation from the results obtained with the traditional mesh became higher than 1%. Once a maximum possible deviation has been decided, a suitable algorithm could be developed to investigate the best percentage of node reduction to find the best compromise between the DoF of the system and the computational time useful to find a numerical solution for the problem considered.

Further improvements on the study proposed in section 3.6 could be represented by the application of the proposed procedure to a wider range of parameters. This could enable the analysis of more complex geometries for the shape of the bluff body. Moreover, the analysis proposed in section 3.6 was carried out with the equations of a laminar flow for the fluid. The turbulent flow in the presence of the optimized bluff body could be compared to the standard shape. Finally, the analysis proposed refers to static operating conditions. An ongoing research is aimed at studying the response of the system both in eigenfrequency and in time dependent conditions. The goal is to extend the optimization procedure to the most interesting operative condition for the device under study: a vibration state produced by the Von Karman street. The characteristic frequency of the swirling vortices phenomenon, which determines the frequency of the mechanical solicitation transferred to the cantilever by the fluid, is influenced by the velocity of the fluid itself and by the geometrical parameters of the device. The synchronization of the frequency of the von Karman vortex with the natural frequency

of the system could enable the system to generate higher electric potential.

In Section 3.5, the output electric potential generated by the cantilever beam was measured over a range of possible wind velocity values between 1.3m/s and 1.63m/s, the interval in which the experimental and simulated setups had more stability. Ongoing research is investigating an improvement to the test-bench setup and a further refinement of the FEM model in order to reduce the discrepancy measured between the numerical results and the experimental measurements. At the time of writing, a cantilever beam is being observed over a range of possible input wind velocity values between 1.56m/s and 9.85m/s. The cantilever beam is being tested inside the subsonic, open loop wind tunnel in the GaVe Lab at the Department of Mechanics, Mathematics and Management (DMMM) of the Politecnico di Bari, shown in Figure 4.30. The wind velocity is no longer detected with the ultrasound anemometer, described in sections 3.3 and 3.5, but is recorded using a non-intrusive Laser Doppler Anemometry (LDA) system.

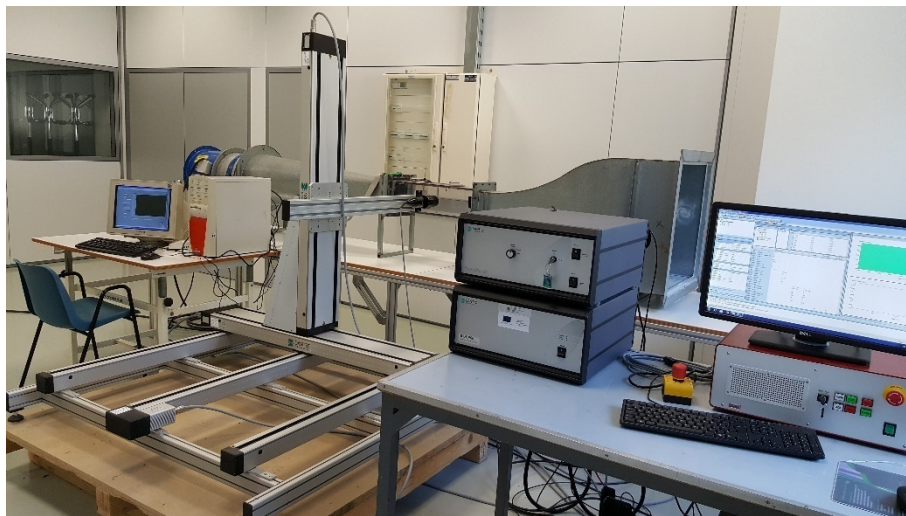


*Figure 4.30 - The subsonic, open loop wind tunnel in the GaVe Lab in the DMMM of the Politecnico di Bari.*

Moreover, an in-depth analysis of the experimental transducer is going to be carried out. Figure 4.31 shows a longitudinal section of the real device, observed under a microscope.



*Figure 4.31 - Longitudinal section of cantilever beam, observed under a microscope.*

In Figure 4.31 it is undeniable that the layers of the plastic cover, made of Mylar, have a considerable thickness compared with that of the PVDF layer. Moreover, the thickness of the upper layer is different from that of the lower layer, but this is not clearly stated in the datasheet of the Meas LDT1-028k transducer [24]. A study is being conducted in order to evaluate the correct proportions of the different layers of the transducer. The results of this study will provide the correct dimensions for the FEM geometry of the transducer.

#### 4.4. Conclusions.

The possible applications of the piezoelectric cantilever beams have been described, in this chapter. EH has been considered as first application field. All the previously described objects have been shown as possible energy harvesters. Moreover an application in NDE has been proposed.

A system made of a piezoelectric cantilever energy harvester and an axle box has been presented. The considered system consists of an axle box that undergoes the vibrations due to the irregularity of the railway track and transmits them to the piezoelectric cantilever beam.

The piezoelectric transducer converts acceleration into electric potential, because of the direct piezoelectric effect, useful to power a wireless sensor node. Therefore, the self-powered sensor node is able to ‘read’ information about the state of health of the axle box and to transmit it to an operational centre that provides an alert about defects or aberrations of the axle box in real time. The harvester device gives a good response as a transducer and the simulated data confirm that the device can effectively be used as a diagnostic tool, because of its different reaction in terms of eigenfrequency and electric

potential generated with or without defects.

The chapter closes with an overview of the possible ongoing and future research of the case studies proposed.

## References.

- [1] Heung Soo K., Joo-Hyon, Jaehwan K. "A Review of Piezoelectric Energy Harvesting Based on Vibration". International Journal of Precision Engineering and Manufacturing 2011, Vol, 12, No. 6, pp. 1129-1141.
- [2] Erturk A., Inman D.J. "Piezoelectric Energy Harvesting". John Wiley and Sons, Ltd., Publication, United Kingdom, 2011.
- [3] Sirohi J., Mahadik R.R. "Harvesting wind energy using a galloping piezoelectric beam". Journal of Vibration and Acoustics, 2011, Vol.134, No. 1.
- [4] Garcia C. "Artificial intelligence applied to automatic supervision, diagnosis and control in sheet metal stamping processes". Journal of Material Processing Technology, 2005, pp.164–165, p.1351–1357.
- [5] Cartz L. "Nondestructive Testing". A S M International. 1995.
- [6] Duran O., Althoefer K., Seneviratne L.D. "Automated pipe defect detection and categorization using camera/laser-based profiler and artificial neural network". IEEE Transactions on Automation Science and Engineering, 2007, Vol.4, No.1, pp. 118 – 126.
- [7] Duran O., Althoefer K., Seneviratne L.D. "Pipe inspection using a laser-based transducer and automated analysis techniques". Transactions on Mechatronics, 2003, Vol.8, No.3, pp. 401–409.
- [8] Cawley P., Alleyne D. "The use of lamb waves for the long range inspection of large structures". Ultrasonics 34, 1996, Vol.2, pp. 287–290.
- [9] Mori K., Spagnoli A., Murakami Y., Kondo G., Torigoe I. "A new non-contacting non-destructive testing method for defect detection in concrete". NDT & E International, 2002, Vol. 35, No. 6, pp. 399-406.
- [10] Xiang, S.K. Tso, "Detection and classification of flaws in concrete structure using bispectra and neural networks". NDT & E International, 2002, Vol. 35, No. 1, pp. 19-27.
- [11] Berriman J.R., Hutchins D.A., Neild A., Gan T.H., Purnell P. "The application of time-frequency analysis to the air-coupled ultrasonic testing of concrete". IEEE Transactions on Ultrasonics, Ferroelectrics and Frequency Control, 2006, Vol. 53, No. 4, pp. 768 – 776.
- [12] **Acciani G., Di Modugno F., Gelao G., Marziani V. "Simulation and Modeling of Self-powered Wireless Sensor Node for Railway Vehicles". Proc. of 14th IMEKO TC10 Workshop on Technical Diagnostics 2016: New Perspectives in Measurements, Tools and Techniques for Systems Reliability, Maintainability and Safety 2016, pp. 84-89.**
- [13] **Acciani G., Di Modugno F., Marziani V., "Nodo sensoriale autoalimentato per diagnostica su trasporto ferroviario", Proc. of 16° Congresso AIPnD, Conferenza Nazionale sulle Prove non Distruttive Monitoraggio Diagnostica Milan, 2015.**
- [14] Roundy S., Wright P.K., Rabaey J. "A study of low level vibrations as a power source for wireless sensor nodes". Journal of Computer Communications, 2002, Vol. 26, No. 11, pp. 1131-1144.
- [15] Knight C., Davidson J., Behrens S. "Energy options for wireless sensor nodes". Sensors, 2008, Vol. 8, pp. 8037–8066.
- [16] Sodano H.A., Inman D.J., Park G. "Comparison of piezoelectric energy harvesting devices for recharging batteries". Journal of Intelligent Material Systems, 2005, Vol. 16, No. 10, pp. 799-807.
- [17] Shu Y.C, Lien I.C. "Analysis of power output for piezoelectric energy harvesting systems". Smart Materials and Structures, 2006, Vol. 15, No. 6, pp. 1499–1512.
- [18] Panthongsy P., Isarakorn D., Sudhawiyangkul T., Nundrakwang S. "Piezoelectric energy harvesting from machine vibrations for wireless sensor system". Electrical Engineering/Electronics, Computer, Telecommunications and Information Technology -ECTI-CON 2015, 12th International Conference on, Hua Hin, 2015, pp. 1-6.
- [19] <http://www.railwaytechnical.com/newglos.shtml#A>, "A Glossary". Railway-Technical.com. Railway Technical Web Pages. 2014.
- [20] UNI EN 13749: "Railway Applications - Wheelsets And Bogies - Method Of Specifying The Structural Requirements Of Bogie Frames", 2011.

- [21] <http://evolution.skf.com/the-evolution-of-ilwayaxlebox-technology/>.
- [22] CEI EN 61373, "Railway applications: Rolling stock equipment-Shock and vibration tests", (CEI 9-61) I, 10, 5834, 2000.
- [23] [www.Comsol.it/multiphysics](http://www.Comsol.it/multiphysics).
- [24] <http://www.meas-spec.com/>.

## 5. Conclusions

Environmental pollution is one of the biggest world problems nowadays. Even though the damaging effects of fossil fuels on the environment are well known, coal, oil and natural gas are still exploited on a large scale to satisfy world energy demand.

Another important contribution to environmental degradation is also provided by the chemical batteries used in low-power electronic devices, such as wearable devices and wireless autonomous elements for sensor networks.

In recent years, several studies into alternative energies have been developed, also encouraged by authorities such as the European Parliament or the Council of the European Union. A lot of them are in the field of the Energy Harvesting, a science which studies the conversion of energy wasted in the environment into different and more useful forms. Energy is everywhere and it is possible to harvest energy, capturing it from environmental sources such as solar, thermal, wind-kinetic energy and natural vibrations. These alternative sources of energy, free and inexhaustible in the environment, are converted into electrical energy through non-polluting processes. Some of them, such as wind and vibrational energy, are used directly by devices that work as generators under the effect of vibrations, due to a specific form of excitation.

This conversion process often involves smart materials such as piezoelectric materials, which develop electrical charge when subjected to mechanical stress. These materials can be well exploited if subjected to the wind force. Wind energy is currently an important renewable source of electrical energy available everywhere in the world. Wind harvester devices can be used and applied universally.

Starting from the above recalled context, this dissertation is aimed at contributing to the production of clean and inexpensive energy, using small piezoelectric devices stressed by natural vibrations and useful to provide energy to low-power devices.

The dissertation analyses the reaction of a piezoelectric cantilever beam under the effect of vibrations. They could be induced by a flowing fluid, such as air or water, or by mechanical movement, such as that of a train on the rails. The vibrational analysis has been carried out both using experimental apparatus and the Comsol Multiphysics simulation environment. The simulations have been validated with experimental data. In this way, the simulation process can be extended to analyse situations not easily testable in the laboratory. Furthermore, the simulation environment offers the opportunity to look at the optimization of several constitutive elements of cantilever beams, such as their shapes, thicknesses and materials they are made of, so allowing the design of an ‘optimal’ cantilever beam, specific for the situation considered. The electrical potential developed by such devices can be stored and reused following the principles of energy harvesting. Moreover, these so designed devices can be used as sensors in the field of non-destructive testing.

With a more detailed description, piezoelectric materials are the main topic of chapter 1. All their properties have been described and they have been classified into the main piezoelectric groups. The crystal classes concerning these materials have been considered and the mathematical model of constitutive equations, useful to describe the behaviour of piezoelectric materials has been presented.

The chapter closes with a novel contribution to the field: an in-depth study of the electromechanical conversion of energy applied to a capacitive two-port device and its relation to the constitutive equations of piezoelectric devices.

A vibrational model has been described in chapter 2. A numerical approach to integrate non-stationary Lyapunov matrix equation has been presented to improve the stochastic linearization technique adopted for non-linear system representation.

The numerical integration algorithm has been used for an important case of vibrational non-linearity, the hysteretic Bouc-Wen model. A single degree of freedom system modelled and subjected to non-stationary filtered white noise has been evaluated under different mechanical conditions and time step sizes. The results show that the proposed algorithm is stable and accurate.

Finally, useful conditions to well define a vibrational problem are discussed at the end of the chapter.

The behaviour of a cantilever beam subjected to wind pressure has been observed and described using a mathematical model, in chapter 3. The analysis was carried out through four different case studies.

In the first case study a unimorph cantilever beam made of structural steel and four different piezoelectric materials (PZT-5H, CdS, BGO and PVDF) was investigated. The analysis showed that the most suitable material to generate electric potential in the analysed situation was CdS, both for maximum absolute value and RMS value of voltage generated. On the other hand, CdS generated a lower surface charge density and a lower energy than PZT-5H. The case study ended with an in-depth study into the thickness of the device made of PZT-5H. Different thicknesses, greater or smaller than the initial one, were considered. The best electric potential generated was provided by the cantilever with the minimum thickness analysed.

In the second case study, a piezoelectric cantilever beam subjected to wind pressure was described. The study compared the behaviour of a cantilever beam, made of silver and PVDF and subjected to wind force, observed with an experimental apparatus, with that of an FEM model of a device with the same features. The behaviour of the cantilever was modelled using constitutive equations of piezoelectric materials and mechanical equilibrium equations. A comparison of values of electric potential generated was made. Other simulations were carried out with different piezoelectric materials and different shapes of piezoelectric layer. Comparisons led to choosing the polymeric material as the best compromise, because of the best RMS value of the electric potential generated and the least expensive cost. In addition, the trapezoidal shape was found to be the best one for the piezoelectric layer.

In case study 3, a novel study to analyse and simulate a piezoelectric cantilever beam subjected to wind force was described. The approach used for this case study represents an improvement on the existing literature because of the inclusion of an extended numerical model for the multiphysics interaction between a fluid and a piezoelectric device. The study considered a finite element model of a 2D cantilever beam. The behaviour of the cantilever beam was modelled using the Navier-Stokes equations and the constitutive equations of piezoelectric materials. The results observed in simulation were compared with the corresponding values detected by an experimental

setup with a reasonable agreement for FEM simulations, thus validating our simulation approach.

In the last case study, an optimization procedure to design a more complex piezoelectric device has been proposed. The device designed is useful to analyse the interaction of the fluid with a deformable piezoelectric cantilever. A fixed D-shaped bluff body was used to generate flow deviation, resulting in a mechanical deformation on the micro-cantilever. A novel geometric parameterisation is proposed to find the maximum performance of the transducer for a fixed velocity of the flow. The optimized cross section shape was compared with the results of the standard D-shape used in the literature.

In chapter 4, some possible applications of the piezoelectric cantilever beams have been described. Energy harvesting and non-destructive evaluation have been considered as application fields. All the objects described in the first three chapters have been shown as possible energy harvester.

A system consisting of a piezoelectric cantilever energy harvester and the axle box of a railway wagon has been presented. The considered system consists of an axle box that undergoes the vibrations due to the irregularity of the railway track and transmits them to the piezoelectric cantilever beam. The piezoelectric transducer converts acceleration into electric potential useful to power a wireless sensor node thanks to the direct piezoelectric effect. Therefore, the self-powered sensor node is able to ‘read’ information about the state of health of the axle box and to transmit it to an operational centre that provides an alert about defects or aberrations of the axle box in real time. The harvester device gives a good response as a transducer, showing that the energy generated by the piezoelectric cantilever beam in the configuration under study is enough to power a wireless sensor node for railway vehicles. Moreover, the sensor reacted differently in terms of eigenfrequency and electric potential generated with or without axle box defects. This shows that the system enables non-destructive diagnosis of the state of health of the axle box, in real time, while the train is in service.

The chapter closes with an overview of the possible ongoing and future research of the case studies proposed.

In summary, piezoelectric devices are a fast growing field due to their possible

use in many different applications, from clean energy production to environmental parameter logging in remote areas. For this reason, research is needed in many branches of this fast developing field and this thesis provides substantial contributions in many of them. Precise mathematical modelling of piezoelectric devices is of paramount importance and a novel electromechanical model is proposed here. Modelling of the phenomena exciting the devices is also critical for the correct forecasting of their behaviour under load. A new such model has been developed, useful to describe mechanically induced vibrations, such as those produced by earthquakes. It is also shown how very advanced multiphysics simulation environments can be exploited to simulate and optimize the development of piezoelectric transducers, comparing the results with real measurements to further refine models and simulations. Finally, this work presents a feasibility study for a real application, in which a self-powered system based on a piezoelectric device can constantly monitor the state of health of the axle-box of a railway carriage and hence contribute to the safety of rail passengers.

## 6. List of publications co-authored by the PhD candidate

### (a) *Contributions in International Journals and Books*

- [a1] Acciani G., Abrescia A., Di Modugno F., Marano G.C. “Numerical algorithm for non-stationary covariance analysis of non linear mechanical system using equivalent stochastic linearization”. *Advances in Computer Science and Engineering*. Pushpa Publishing House, 2014, Vol. 13, No. 1, pp. 27 - 49.
- [a2] Acciani G., Di Modugno F., Giaquinto A., Maiullari D., Dimucci A., Fornarelli G. “Models of Piezoelectric Materials for Transduction and Energy Harvesting”. *Advances in Materials Science Research*. Nova Science Publishers, 2015, Vol. 19, pp. 1-42.
- [a3] Acciani G., Di Modugno F., Gelao G. “Comparative Studies of Piezoelectric Harvester Devices”. *Energy Harvesting: Technology, Methods and Applications*, Nova Science Publishers, 2016, pp. 1-18.
- [a4] Acciani G., Adamo F., Di Modugno F., Gelao G. “Modelling and simulation of cantilever beam for wind energy harvesting”. *JVE Journal of Vibroengineering*, 2016, Vol. 18, No. 2, pp. 1167-1174.
- [a5] G. Acciani, F. Di Modugno, A. Abrescia, G.C. Marano, “Integration algorithm for covariance nonstationary dynamic analysis using equivalent stochastic linearization”, *Mathematics and Computers in Simulation*, 2016, Vol. 125, pp. 70-82.

### (b) *Contributions in International Conferences*

- [b1] Marano G.C., Acciani G., Abrescia A., Di Modugno F., “Equivalent Stochastic Linearization Algorithm for Non-Stationary Covariance Analysis of Mechanical Systems”, SDS 2014 – 8th Workshop on Structural Dynamical Systems, Monopoli (BA), Italy 10-13 June 2014.
- [b2] Acciani G., Di Modugno F., Gelao G. “Modelling and simulation of a cantilever beam for wind energy harvesting”. 12th International Workshop on Piezoelectric Materials and Applications in Actuators - IWPMA 2015, Vilnius, Lithuania, 29 June - 1 July 2015.
- [b3] Acciani G., Di Modugno F., Gelao G., Mininno E. “Shape Optimization of Cantilever Beam for Wind Energy Harvesting”. *Proc. of International Conference on Renewable Energy Research and Applications - ICRERA 2015*, pp. 1207-1212.
- [b4] Acciani G., Di Modugno F., Mininno E., Montegiglio P. “Multi-physics Simulation of a Wind Piezoelectric Energy Harvester Validated by Experimental Results”. *Proc. of 17th International conference on Thermal, Mechanical and Multiphysics Simulation and Experiments in Microelectronics and Microsystems - EUROSIME 2016*.
- [b5] Acciani G., Di Modugno F., Gelao G., Marziani V. “Simulation and Modeling of Self-powered Wireless Sensor Node for Railway Vehicles”. *Proc. of 14th IMEKO TC10 Workshop on Technical Diagnostics 2016: New Perspectives in Measurements, Tools and Techniques for Systems*

Reliability, Maintainability and Safety 2016, pp. 84-89.

- [b6] Acciani G., Mininno E., Montegiglio P., Di Modugno F. "Fluid Flow Based Micro Energy Harvester Optimization". Proc. of 16th IEEE International Conference on Environment and Electrical Engineering - IEEEIC 2016.
- [b7] Acciani G., Politi T., Di Modugno F. "Mesh Improvement Criteria in Dynamic Study of Thin Layers with Finite Element Method". 9th Workshop on Structural Dynamical Systems: Computational Aspects - SDS 2016, Monopoli (BA), Italy, June 2016.

(c) Contributions in National Conferences

- [c1] Acciani G., Di Modugno F., Amoroso V. "An electromechanical model for harvesting simulation", Proc. of 1st Workshop on the State of the Art and Challenges of Research Efforts at POLIBA, 2014.
- [c2] Acciani G., Di Modugno F., Marziani V., "Nodo sensoriale autoalimentato per diagnostica su trasporto ferroviario", Proc. of 16° Congresso AIPnD, Conferenza Nazionale sulle Prove non Distruttive Monitoraggio Diagnostica, 2015.